Abstract The main aim of this thesis has been to find a cosmologically motivated infall law to understand if the ΛCDM cosmology can reproduce the main chemical characteristics of a Milky Way-like spiral galaxy.

We have tested several gas infall laws, starting from that suggested in the two-infall model of Chiappini et al. (1997) for the chemical evolution of the Milky Way, but focusing on laws derived from cosmological simulations which follow a concordance ΛCDM cosmology. By means of a detailed chemical evolution model for the solar vicinity, we have studied the effects of the different gas infall laws on the abundance patterns and the G-dwarf metallicity distribution.

Our best cosmological infall law, derived from dark matter halos having properties compatible with the formation of a disk galaxy like the Milky Way, and assuming that the baryons assemble like dark matter, resembles the infall law suggested by the two-infall model. It predicts two main gas accretion episodes. Minor infall episodes are predicted to have followed the second main one but they are of little significance compared to the previous two. By means of this cosmologically motivated infall law, we have studied the star formation rate, the SNIa and SNII rate, the total amount of gas and stars in the solar neighbourhood and the behaviour of several chemical abundances (O, Mg, Si, C, N, Fe). We have found that the results of the two-infall model are fully compatible with the evolution of the Milky Way with cosmological accretion laws. We have derived that the timescale for the formation of the stellar halo and the thick disk must have not been longer than 2 Gyr, whereas the disk in the solar vicinity assembled on a much longer timescale ($\sim$ 6 Gyr).

Then we have studied the abundance gradients along the Galactic disk produced by our best cosmological model and their dependence upon several parameters: a threshold in the surface gas density regulating star formation, the star formation efficiency, the timescale for the formation of the thin disk and the total surface mass density of the stellar halo.

We have found that to reproduce at the same time the abundance, star formation rate and surface gas density gradients along the Galactic disk it is necessary to assume an inside-out formation for the disk. The threshold in the gas density is not necessary and the same effect could be reached

by assuming a variable star formation efficiency. However the derived new cosmological infall law contains a mild inside-out formation and is still not enough to reproduce the disk properties at best.

We have also studied the effect of a cosmologically motivated infall law for the formation of a massive elliptical galaxy in order to understand the impact on the formation of the spheroids.

We have found that such a model predicts a too low mean stellar value for the [Mg/Fe] ratio. This is, according to us, the most important result of our cosmological model applied to an early-type galaxy indicating that perhaps the hierarchical paradigm of galaxy formation should be revised for ellipticals. Moreover we have found that models for ellipticals without a galactic wind predict a too large current SNIa rate. In particular, the cosmological model produces a current SNIa which is about ten times higher than the observed values and predicts a large current SNII rate which is not observed. The predicted SNII rate for models with galactic wind is also in contrast with the actual star formation mesured by GALEX.

The conclusions of our work are that a gas assembly history derived from a DM halo, compatible with the formation of a late-type galaxy from the morphological point of view, can produce chemical properties in agreement with the available observations. Moreover, a cosmologically derived infall law with an inside-out process for the disk formation and a variable star formation efficiency can indeed well reproduce all the properties of the disk. Higher resolution cosmological simulations, however, are necessary to better trace the radial properties of disk galaxies. Finally, a cosmologically derived infall law for an elliptical galaxy cannot well reproduce all the chemical constraints given by observations and this is an important result.

Aknowledgements I want to thank my parents, Rino and Paola, my brother Alberto and his wife, Lucia, to have walked by my side during these three years.

I also want to thank my supervisor, Prof. Francesca Matteucci, since she helped me to give my best and for all the things she tought to me.

I have a debt with Giuseppe Murante for all the useful suggestions. Without him my thesis would not exist.

I thank Cristina Chiappini since she has been a really precious referee.

Thank you very much to all my collegues for the pleasant chats and to Gabriele Cescutti and Francesco Calura for all the help they gave me.

Finally, I want to thank Guido Cupani e Monica Midori Marcon Uchida Anunciato for some irreplaceable moments.

Contents

1 Overview **11**

2 Chemical evolution models **19**
2.1 Basic ingredients 19
2.1.1 The initial conditions 20
2.1.2 Birthrate function 20
2.1.3 Stellar yields 22
2.1.4 Gas flows 23
2.1.5 Type Ia SN progenitors 23
2.2 Detailed numerical models 25

3 The cosmological simulation **27**

4 The MW in the solar vicinity **33**
4.1 The two infall model 33
4.2 Nucleosynthesis prescriptions 35
4.3 The infall laws 36
4.4 Results for the solar neighborhood 40

5 Formation of the MW disk **61**
5.1 Models C08, C97, 1 and 2 67
5.2 The cosmological infall law with inside-out 74
5.3 Changing the parameters in the C97 models 75

6 Elliptical formation **89**
6.1 Introduction to elliptical galaxies 90

6.2 The cosmological infall law 92
6.3 The model by Pipino & Matteucci (2004) 93
6.4 Results for an elliptical galaxy 94
6.4.1 Comparison between the three models 95
6.4.2 Comparison with observables 100

7 Conclusions **107**

List of Figures

3.1 The best cosmological halo at four different redshift 32

4.1 $a(r)$ vs radius 38
4.2 Infall vs time for all the models 46
4.3 Σ_{tot} vs time for all the models 47
4.4 SFR vs time for all the models 48
4.5 SNIa rate vs time for all the models 49
4.6 Fe/H vs time for all the models 50
4.7 G-dwarf metallicity distribution for all the models 51
4.8 O/Fe vs Fe/H for all the models 52
4.9 O/Fe vs Fe/H for all the models 53
4.10 Mg/Fe vs Fe/H for all the models 54
4.11 Si/Fe vs Fe/H for all the models 55
4.12 C/Fe vs Fe/H for all the models 56
4.13 N/Fe vs Fe/H for all the models 57
4.14 Infall law, SFR, SNIa rate and the Fe/H for the halo 20912 . 58
4.15 O/Fe vs Fe/H for the halo 20912 59
4.16 G-dwarf metallicity distribution for the halo 20912 60

5.1 Infall law of the best cosmological halo at three different radii 62
5.2 Predicted and observed O abundance gradients in the galactocentric distance range 4 - 14 kpc 63
5.3 $SFR/SFR_{\odot}$ and surface gas density vs radius for Models C97 and C08 68
5.4 O/H, N/H and Fe/H vs radius for Models C97 and C08 . . . 69

5.5 $SFR/SFR_{\odot}$ and surface gas density vs radius for Models 1 and C08 70
5.6 O/H, N/H and Fe/H vs radius for Models 1 and C08 71
5.7 $SFR/SFR_{\odot}$ and surface gas density vs radius for Models 2 and C08 72
5.8 O/H, N/H and Fe/H vs radius for Models 2 and C08 73
5.9 $SFR/SFR_{\odot}$ and surface gas density vs radius for Models 3 and C08 76
5.10 O/H, N/H and Fe/H vs radius for Models 3 and C08 77
5.11 $SFR/SFR_{\odot}$ and surface gas density vs radius for Models 4 and C08 79
5.12 O/H, N/H and Fe/H vs radius for Models 4 and C08 80
5.13 $SFR/SFR_{\odot}$ and surface gas density vs radius for Models 5 and C08 81
5.14 O/H, N/H and Fe/H vs radius for Models 5 and C08 83
5.15 $SFR/SFR_{\odot}$ and surface gas density vs radius for Models 6 and C08 84
5.16 O/H, N/H and Fe/H vs radius for Models 6 and C08 85
5.17 $SFR/SFR_{\odot}$ and surface gas density vs radius for Models 7 and C08 86
5.18 O/H, N/H and Fe/H vs radius for Models 7 and C08 87

6.1 The gas infall rate vs time 96
6.2 Total mass vs time 97
6.3 The star formation rate vs time 98
6.4 The SNIa rate vs time 99
6.5 Fe/H vs time 101
6.6 Mg/Fe vs Fe/H 102

List of Tables

3.1 Characteristics of the chosen DM halos 30

4.1 Models parameters: adopted infall law, time scale for the halo and for the disk, type of infalling gas 39
4.2 Current values for all the models and observed values (SFR, infall, SNII rate and SNIa rate) 41
4.3 Current values for all the models and observed values (gas, stars, $\frac{\Sigma_{gas}}{\Sigma_{tot}}$ and Σ_{tot}) 42
4.4 Predicted and observed solar abundances by mass (after 8.64 Gyr from the Big Bang) 43

5.1 Model parameters: threshold, SF efficiency, inside-out formation, halo density, type of infall law and SFR 66
5.2 Models successes and failures 88

6.1 Luminous mass, star formation efficiency and time of formation 95
6.2 Mean values for Fe/H, Mg/H and Mg/Fe 103
6.3 Mass in stars formed in the last 1.0 and 6.2 Gyr 104
6.4 Current SNIa rate and SNII rate in SNum 105

Chapter 1

Overview

One of the major challenge in modern astrophysics is to understand the origin and evolution of galaxies. Two kinds of approaches have been explored up to now: a forward approach and a backward approach.

The forward approach is based on modelling galaxy formation and evolution in a cosmological context. In a Universe dominated by Cold Dark Matter (CDM) and, as recent observations seem to suggest, by some kind of Dark Energy in the form of a non-zero Cosmological Constant Λ, and containing a suitable mix of baryons and photons, cosmic structures are formed by the gravitational collapse of Dark Matter and are organized in a hierarchy of complexes (halos) inside which baryons dissipate their energy and collapse to form luminous systems.

The backward approach, instead, is based on reproducing the observed properties of stellar populations at present time and, from them, inferring the evolutionary history of a galaxy. In this context, our work mainly refers to the backward approach model of Chiappini et al. (1997), the so called two-infall model for the Milky Way. Prior to this model, different models assuming gas accretion onto the galactic disk had been constructed. For example, dynamical models, such as the one of Larson (1976), viscous models (Lacey & Fall 1985; Sommer-Larsen & Yoshii 1989, 1990; Tsujimoto et al. 1995), inhomogeneous models (Malinie et al. 1993), detailed chemical evolution models (Matteucci & Greggio 1986; Tosi 1988; Matteucci & François 1989; Pagel 1989; Matteucci & François 1992; Carigi 1994; Giovagnoli &

Tosi 1995; Ferrini et al. 1994; Pardi & Ferrini 1994; Pardi, Ferrini & Matteucci 1995; Prantzos & Aubert 1995; Timmes, Woosley & Weaver 1995) and chemodynamical models (Samland & Hensler 1996, Burkert, Truran & Hensler 1992).

The model of Chiappini et al. (1997) was the first in which two main infall episodes for the formation of the Galactic components were suggested. In particular, they assumed that the first infall episode was responsible for the formation of the halo and thick-disk that originated from a fast dissipative collapse. The second infall episode formed the thin-disk component, with a timescale much longer than that of the thick-disk formation. The authors also included in the model a threshold in the gas density below which the star formation process stops. The existence of such a threshold value was suggested by observations relative to the star formation in external disk galaxies (Kennicutt 1998b, but see Boissier et al. 2006). The physical reason for a threshold in the star formation is related to the gravitational stability, according to which, below a critical density, the gas is stable against density condensations and, consequently, the star formation is suppressed. In the two-infall model the halo-thick disk and the thin disk evolutions occur at different rates, mostly as a result of different accretion rates. With these prescriptions it has been possible to reproduce the majority of the observed properties of the Milky Way and this shows how important is the choice of the accretion law for the gas coupled with the star formation rate in the Galaxy evolution.

On the other hand, in the context of cosmological models, we recall the one of Naab & Ostriker (2006) who presented a simplified model (assuming I.R.A.) for the evolution of disk galaxies in a ΛCDM cosmological context, assuming that a generic disk forms through mergers of dark matter halos. Their model needs three input parameters: the present-day scalelenght of the total disk surface density distribution, the central surface density of the disk and the circular velocity. They used these three parameters to constrain the evolution of the infall rate. They assumed that in the absence of star formation the gas in a given halo would settle in a disk with an exponential surface density, starting the star formation after the disk is formed. Throughout the paper they used a formulation for the star formation based on the local

dynamical time (rotation period) of the system.

With this model they were able to reproduce a large number of observed global and local properties of the Milky Way. However, their model does not contain any detailed chemical evolution and no consideration is given to the formation of the stellar halo. Moreover their model is a simplified version of a hierarchical model. In fact, in the hierarchical framework disk galaxies do not only grow continuously by smooth accretion of gas but also in discrete steps by minor mergers and accretion of small satellites. In addition, a small amount of old stars that have formed within small satellites are continuously added to the disk by accretion.

Robertson et al. (2005) adopted the hierarchical scenario for galaxy formation to see if in this context they could reproduce the rich data set of stellar abundances in the galactic halo and Local Group dwarf galaxies. They used an analytical expression for the growth of DM halos in a ΛCDM cosmology. Their baryonic infall law was proportional to the DM one. The hierarchical formation scenario, when applied to the stellar halo of the Milky Way, suggests that it formed through accretion and disruption of dwarf galaxies. They concluded that the majority of stars in the stellar halo were formed within a relatively massive dwarf irregular sized dark matter halo, which was accreted ~ 10 Gyr ago. In their scenario, these systems had rapid star formation histories and were enriched primarily by supernovae (SNe) of type II. They also suggested that the still existing dwarf irregular galaxies formed stars more gradually and they underwent both SNIa and II enrichment. On the other hand, dwarf spheroidal galaxies should be systems where the abundances are determined by galactic winds. In summary, the paper dealt mostly with the comparison between the $[\alpha/\mathrm{Fe}]$ ratios in the galactic halo and dwarf galaxies.

Another paper dealing with chemical evolution in a cosmological context is that by Nagashima & Okamoto (2006). The authors investigated the chemical evolution in Milky Way-like galaxies based on the ΛCDM model in which cosmic structures form via hierarchical merging. They adopted a semi-analytical model for galaxy formation where the chemical enrichment due to both SNeIa and SNeII was considered. They suggested that the so-called G-dwarf metallicity problem can be fully resolved by the hierarchical formation of galaxies. In fact, the infall term introduced by the traditional

monolithic collapse models to solve the G-dwarf problem can be explained by some physical processes such as injection of gas and metals into hot gas due to SNe. The model, however, was not tested on a large number of chemical elements but was limited to the [O/Fe] vs. [Fe/H] plot.

When only cooling processes are included, smoothed-particle hydrodynamical simulatons of galaxy formation in a ΛCDM hierarchical clustering scenario produce collapsed objects that are deficient in angular momentum. Sommer-Larsen, Gelato & Vedel (1999) explored and compared the effects of including two different types of feedback event to solve the problem: an uniform reheating of the entire universe at redshift ~ 6 and a gas blowout from pregalactic clouds at a lower redshift. They found that blowout is more successful than early reheating and that it can be sufficient to solve the angular momentum problem. They showed that the remaining angular momentum deficit was due to limitations in the numerical method they used.

Another important paper about the the formation of a disk galaxy within a growing dark matter halo is that of Samland & Gerhard (2003). They used the cosmological N-body simulations of the VIRGO-GIF-project (Kauffmann et al. 1999) to study the galactic evolution of 96 halos. The three-dimensional chemo-dynamical code included dark matter, stars and a multi-phase ISM. In their model the star formation rate reaches a maximum at redshift $z \sim 1$. Moreover they showed that the galaxy forms radially from inside-out and vertically from halo-to-disk. The first galactic component that forms is the halo, followed by the bulge and the disk-halo transition region. The last component is the disk. They also found that at redshift ~ 1 a gaseous ring forms and then it collapses and forms a galactic bar. It alters the structure of the disk, induces spiral arms, enhances the mixing of ISM and flattens metallicity gradients in the disk.

An intermediate approach between chemical models and cosmological ones was followed by Prantzos (2003) who developed a detailed model of the Milky Way and extended it to other disks using some simple scaling relations obtained in the framework of CDM models. With his approach he could reproduce a large number of observables of galaxies in the local universe, including: disk sizes and central surface brightness, Tully-Fisher relations in various wavelenght bands, gas fractions vs magnitude and abundances as a

function of local and integrated properties. He found that the crucial ingredient of that success was the assumption that gas is infalling more slowly in galaxies with smaller masses and/or surface densities. He showed that, on average, massive disks are older than lower mass ones, being redder, poorer in gas and richer in metals than less massive ones. In spite of the cosmological context, this result is in contrast with the hierarchical galaxy formation scenario, where low mass dark matter halos form first, while more massive ones are formed later through accretion and merging.

Samland (2004) developed a model for the formation of the Milky Way where the galaxy forms inside a slowly growing dark matter halo in a ΛCDM cosmology. In this case the galactic mass grows continuosly, without any major merger, over a Hubble time. The whole formation scenario was simulated with a three-dimensional chemodynamical code. This model predicted that even galaxies like the Milky Way show phases with supernova-driven galactic winds. However, being the mass loss of the order of a few per cent of the total baryonic mass, these galaxies are in all probability not the main contributors to the enrichment of the intergalactic medium. As expected, the mass loss decreases with increasing mass of galaxy and it also increases with angular momentum. For dwarf galaxies the model by Samland (2004) predicts mass losses up to 80% of the baryonic matter.

Abadi et al. (2003a) presented a detailed analysis of the dynamical and photometric properties of a spiral galaxy simulated in the ΛCDM scenario. They used a three-dimensional simulation including gravitational and hydrodynamical effects of dark matter, gas and stars. Moreover they also included the energetic feedback from stellar evolution. They found that the galaxy assembled through a number of high-redshift mergers followed by a rather quiescent period after $z \sim 1$. They found that 75% of stars have already formed by $z \sim 1.3$ and that two distinct dynamical components formed: a spheroid of mostly old stars and a rotationally supported disk of younger stars. They showed that approximately half of the total light comes from each component. The luminous component had a specific angular momentum well below that of late-type spirals of similar rotation speed, in agreement with their previous simulation work. Finally they showed that the main limitation of their simulation was the simplified star formation/feedback recipe

adopted.

In a second paper, Abadi et al. (2003b) focused on the fine structure of simulated galactic disks in a ΛCDM universe. They used the same simulation of their first paper and they analyzed a galaxy formed in a dark matter halo chosen so that mergers and accretion events were dynamically unimportant after z $\sim$ 1. They found that at z = 0 two separate stellar components were easily distinguishable on the basis of the orbital parameters of stars in the galaxy: a slowly rotating, centrally concentrated spheroid and an extended disk-like component largely supported by rotation. The spheroid was old and had no stars younger than the last major accretion episode, i.e. $\sim$ 8 Gyr in the past for their galaxy. On the other hand, the majority of thin-disk stars formed after the merging activity was over and had a mean age of $\sim$ 5 Gyr. They could also decompose the disk in two well-defined subcomponents: a thin, dynamically cold disk of stars on nearly circular orbits and a thicker disk with orbital parameters transitional between the thin disk and the spheroid. The bulk ($\sim$ 60%) of the thick-disk consisted of the tidal debris of satellites whose orbital plane was roughly coincident with the disk. Moreover they found that a significant fraction ($\sim$ 15%) of thin-disk stars were old enough to predate the last major accretion event. These were the remains of the cores of disrupted satellites.

Also Governato et al. (2007) used cosmological simulations to follow the formation of disk galaxies in a ΛCDM universe. Their simulations included gas cooling, star formation, the effects of a uniform ultraviolet background and a physically motivated description of feedback from supernovae. They showed that an extended stellar disk formed inside the Milky Way-sized halo immediately after the last major merger. Moreover the combination of UV background and SN feedback drastically reduced the number of visible satellites orbiting inside the Milky Way-sized halo. Their simulations predicted that the average age of a primary galaxy's stellar population decreases with mass because feedback delays star formation in less massive galaxies. They showed that their simulated galaxies reproduced the observed 'antihierarchical' trend of stellar polulations: smaller galaxies have younger stellar populations. The authors underlined that their simulations and those published in the recent literature show that some significant progress has been done to-

ward understanding galaxy formation in the context of a ΛCDM concordance cosmology. However, areas remain were progress needs to be made. For example, a large range of initial conditions needs to be explored to understand the role played by halo spin and merging history on the morphology and colours of galaxies. Moreover satellites are still too bright compared to those orbiting our Milky Way. One obvious possibility to create fainter satellites would be to increase the efficiency of SN feedback.

In addition, most of these models in a cosmological context adopt a very simple scheme for computing chemical evolution. Most of these models, for example, assume the instantaneous recycling approximation (I.R.A.) which neglects stellar lifetimes and it does not allow a precise calculation of the evolution of the abundances of single elements in the gas, especially those produced on long timescales. In this thesis we attempt of constructing a very detailed chemical evolution model in a cosmological context.

Chapter 2

Chemical evolution models

Galactic chemical evolution describes how the gas as a whole and its chemical composition evolve with time in galaxies. In order to build models to compute galactic chemical evolution one needs to specify the basic ingredients and the equations. Details can be found in Matteucci (2008).

2.1 Basic ingredients

The basic ingredients to build a model of galactic chemical evolution can be summarized as:

- Initial conditions
- Stellar birthrate function (the rate at which stars are formed from the gas and their mass spectrum)
- Stellar yields (how elements are produced in stars and restored into the interstellar medium)
- Gas flows (infall, outflow, radial flow)

The chemical abundance of a generic chemical species i is defined as:

$$X_i = \frac{M_i}{M_{gas}}. \tag{2.1}$$

According to this definition it holds:

$$\sum_{i=1,n} X_i = 1, \tag{2.2}$$

where n represents the total number of chemical species.

2.1.1 The initial conditions

The initial conditions for a model of galactic chemical evolution consist in establishing whether: a) the chemical composition of the initial gas is primordial or pre-enriched by a pre-galactic stellar generation; b) the studied system is a closed box or an open system (infall and/or outflow).

2.1.2 Birthrate function

The birthrate function can be defined as:

$$B(M,t) = \psi(t)\varphi(m), \tag{2.3}$$

where the quantity:

$$\psi(t) = SFR, \tag{2.4}$$

is called the star formation rate, namely the rate at which the gas is turned into stars, and the quantity:

$$\varphi(t) = IMF, \tag{2.5}$$

is the initial mass function (IMF), namely the mass distribution of the stars at birth.

The most common parametrization of the SFR is the Schmidt (1959) law:

$$\psi(t) = \nu\sigma_{gas}^{k}, \tag{2.6}$$

where k = 1-2 with a preference for $k = 1.4 \pm 0.15$, as suggested by Kennicutt (1998a) for spiral disks and ν is a parameter describing the star

formation efficiency. Other physical quantities such as gas temperature, viscosity and magnetic field are usually ignored.

Other common parametrizations of the SFR include a dependence on the total surface mass density besides the surface gas density:

$$\psi(t) = \nu \sigma_{tot}^{k1} \sigma_{gas}^{k2}, \tag{2.7}$$

as suggested by observational results of Dopita & Ryder (1994) and taking into account the influence of the potential well in the star formation process. Other suggestions concern the star formation induced by spiral density waves (Wyse & Silk 1998) with expressions like:

$$\psi(t) = \nu V(R) R^{-1} \sigma_{gas}^{1.5}, \tag{2.8}$$

or

$$\psi(t) = 0.017 \Omega_{gas} \sigma_{gas} \propto R^{-1} \sigma_{gas}, \tag{2.9}$$

with Ω_{gas} being the angular rotation speed of gas (Kennicutt 1998a).

The most common parametrization of the IMF is a one-slope (Salpeter 1955) or multi-slope (Scalo 1986, 1998; Kroupa et al. 1993, Chabrier 2003) power law. The most simple example of a one-slope power law is:

$$\varphi(m) = a m^{-(1+x)}, \tag{2.10}$$

generally defined in a mass range of 0.1 - 100 $M_{\odot}$, where a is the normalization constant derived by imposing that $\int_{0.1}^{100} m\varphi(m)dm = 1$.

The Scalo and Kroupa IMFs were derived from stellar counts in the solar vicinity and suggest a three-slope function. Unfortunately, the same analysis cannot be done in other galaxies and we cannot test if the IMF is the same everywhere. Kroupa (2001) suggested that the IMF in stellar clusters is a universal one, i.e.:

$$x_1 = 0.3 \; for \; 0.08 \leq M/M_{\odot} \leq 0.50 \tag{2.11}$$

$$x_2 = 1.3 \; for \; M/M_{\odot} > 0.50. \tag{2.12}$$

Weidner & Kroupa (2005) suggested that the IMF integrated over galaxies is generally different from the IMF in stellar clusters. Therefore, we should expect that the chemical enrichment histories of different galaxies cannot be reproduced by an unique invariant Salpeter-like IMF.

2.1.3 Stellar yields

The stellar yields, namely the amount of newly material ejected with the respect to the material locked up in the star, represent a fundamental ingredient to compute galactic chemical evolution. All the elements with mass number A from 12 to 60 have been formed in stars during the quiescent burnings. Stars transform H into He and then He into heaviers until the Fe-peak elements, where the binding energy per nucleon reaches a maximum and the nuclear fusion reactions stop. H is transformed into He through the proton-proton chain or the CNO-cycle, then ^4He is transformed into ^{12}C through the triple-α reaction.

Elements heavier than ^{12}C are then produced by synthesis of α-particles: they are called α-elements (O, Ne, Mg, Si and others).

The last main burning phase in stars is the ^{28}Si-burning which produces ^{56}Ni, which then decays into ^{56}Co and ^{56}Fe. Si-burning can be quiescent or explosive (depending on the temperature).

Explosive nucleosynthesis occurring during SN explosions mainly produces Fe-peak elements. Elements originating from s- and r-processes (with A $>$ 60 up to Th and U) are formed by means of slow or rapid (relative to the β-decay) neutron capture on Fe seed nuclei; s-processing occurs during quiescent He-burning, whereas r-processing occurs during SN explosions (Sneden & Cowan 2003).

Some yields are obtained by assuming mass loss by stellar winds with a strong dependence on metallicity (e.g. Maeder 1992), whereas others (Woosley & Weaver 1995) are computed by means of conservative models without mass loss. One important difference arises for oxygen in massive stars for solar metallicity and mass loss: in this case the O yield is strongly depressed as a consequence of mass loss. In fact, the stars with masses $>$ 25 $M_\odot$ and solar metallicity lose a large amount of matter rich in He and

C, thus subtracting these elements to further processing which would lead to O and heavier elements. So the net effect of mass loss is to increase the production of He and C and to depress that of O. More recently, Meynet & Maeder (2002, 2003, 2005) have computed a grid of models for stars with M > 20 $M_\odot$ including rotation and metallicity dependent mass loss. The effect of metallicity dependent mass loss in decreasing the O production in massive stars was confirmed, although they employed significantly lower mass loss rates compared with Maeder (1992).

2.1.4 Gas flows

Various parametrizations have been suggested for gas flows and the most common is an exponential law for the gas infall rate:

$$IR \propto e^{-t/\tau}, \tag{2.13}$$

with the timescale τ being a free parameter, whereas for the galactic outflows the wind rate is generally assumed to be proportional to the SFR:

$$WR \propto -\lambda SFR, \tag{2.14}$$

where λ is againg a free parameter. Both τ and λ should be fixed by reproducing the majority of observational constraints.

2.1.5 Type Ia SN progenitors

Type Ia SNe originate from C-deflagration in C-O white dwarfs (WD) in binary systems. The C-deflagration produces ~ 0.6 - 0.7 $M_\odot$ of Fe plus traces of other elements from C to Si, as observed in the spectra of SNIa. Two main evolutionary scenarios for the progenitors of SNIa have been proposed:

- Single Degenerate (SD) scenario: the classical scenario of Whelan and Iben (1973), recently revised by Han & Podsiadlowsky (2004), namely C-deflagration in a C-O WD reaching the Chandrasekhar mass $M_{Ch} \sim 1.44$ $M_\odot$ after accreting material from a red giant companion. Kobayashi et al. (1998) had proposed a similar scanario, based on the model of

Hachisu et al. (1996), where the companion can be either a red giant or a main sequence star. The clock to the explosion in this scenario is given by the lifetime of the secondary star in the binary system, where the WD is the primary (the originally more massive one). Therefore, the largest mass for a secondary is 8 $M_{\odot}$, which is the maximum mass for the formation of a *C-O* WD. As a consequence, the minimum timescale for the occurance of SNIa is $\sim$ 30 Myr (i.e. the lifetime of a 8 $M_{\odot}$) after the beginning of star formation. The minimum mass for the secondary is 0.8 $M_{\odot}$, which is the star with lifetime equal to the age of the Universe.

- Double Degenerate (DD) scenario: the merging of two *C-O* WDs, due to the loss of angular momentum caused by gravitational wave radiation, which explode by *C*-deflagration when M_{Ch} is reached. In this scenario the two *C-O* WDs should be of $\sim$ 0.7 $M_{\odot}$ in order to give rise to a Chandrasekhar mass after they merge, therefore their progenitors should be in the range 5-8 $M_{\odot}$. The clock to the explosion here is given by the lifetime of the secondary star plus the gravitational time delay which depends on the original separation of the two WDs. The minimum timescale for the appearance of the first SNIa in this scenario is about one million year more than in the SD scenario (Greggio 2005).

Within any scenario the explosion can occur either when the *C-O* WD reaches the Chandrasekhar mass and carbon deflagrates at the center or when a massive enough helium layer is accumulated on top of the *C-O* WD.

A way of defining the typical SNIa timescale is to assume it as the time when the maximum in the SNIa rate is reached (Matteucci & Recchi 2001). This timescale varies according to the chosen progenitor model and to the assumed star formation history, which varies from galaxy to galaxy. For the solar vicinity, this timescale is at least 1 Gyr, if the SD scenario is assumed, whereas for elliptical galaxies, where the stars formed much more quickly, this timescale is only 0.5 Gyr (Matteucci & Greggio 1986; Matteucci & Recchi 2001).

2.2 Detailed numerical models

Detailed models of galactic chemical evolution require consideration of the stellar lifetimes, namely they should relax IRA. However, the majority of them still retain the instantaneous mixing approximation (IMA).

The basic equations of chemical evolution follow the evolution of the abundances of single chemical species and the gas as a whole. If σ_i is the surface mass density of an element i, with $\sigma_{gas} = \sum_{i=1,n} \sigma_i$ being the total surface gas density and n the total number of chemical elements, we can write:

$$\begin{aligned}
\dot{\sigma}_i(t) \;=\; & -\psi(t)X_i(t) \\
& + \int_{M_L}^{M_{Bm}} \psi(t-\tau_m))Q_{mi}(t-\tau_m)\varphi(m)dm \\
& + A\int_{M_{Bm}}^{M_{BM}} \varphi(m) \\
& \cdot [\int_{\gamma_{min}}^{0.5} f(\gamma)\psi(t-\tau_{m2})Q_{mi}(t-\tau_{m2})d\gamma]dm \\
& + B\int_{M_{Bm}}^{M_{BM}} \psi(t-\tau_m)Q_{mi}(t-\tau_m)\varphi(m)dm \\
& + \int_{M_{BM}}^{M_U} \psi(t-\tau_m)Q_{mi}(t-\tau_m)\varphi(m)dm \\
& + X_{A_i}A(t) - X_i(t)W(t), \qquad (2.15)
\end{aligned}$$

for any given chemical element. These equations can be solved only numerically. The quantities $X_i(t)$ are the abundances as defined in eq. (2.1). The quantity Q_{mi} contains all the information about stellar evolution and nucleosynthesis.

The various integrals represent the rates at which the mass of a given element is restored into the ISM by stars of different masses which can evolve into WDs or supernovae (II, Ia, Ib). The integral representing the rate of matter restoration by SNIa is the second one on the right hand side. The quantity A is a constant: it is the fraction, in the IMF, of binary systems with those specific features required to give rise to SNIa, whereas $B = 1 - A$ is the fraction of all the single stars and binary systems in the same mass

range of definition of the progenitors of SNIa (third integral).

The integral of the SNIa contribution is made over a range of mass going from $M_{Bm} = 3M_{\odot}$ to $M_{BM} = 16M_{\odot}$, which represents the total masses of binary systems able to produce SNIa in the framework of the single degenerate scenario. There is also an integration over the mass distribution of binary systems; in particular, one considers the function $f(\gamma)$ where $\gamma = \frac{M_2}{M_1+M_2}$, with M_1 and M_2 being the primary and secondary mass of the binary system, respectively (for more details see Matteucci & Greggio 1986 and Matteucci 2001). The third and fourth integrals represent the rates of Type II and Type Ib/c SNe, respectively. Finally, the functions $A(t)$ and $W(t)$ are the infall and wind rate, respectively.

For type Ia SNe, if a progenitor model made of a C-O white dwarf plus a red giant (Whelan & Iben 1973) is assumed, the resulting rate is:

$$R_{SNIa} = A \int_{M_{Bm}}^{M_{BM}} \psi(M_B) \int_{\mu_m}^{0.5} f(\mu)\psi(t - \tau_{M2})\, d\mu\, dM_B. \qquad (2.16)$$

(Greggio & Renzini 1983; Matteucci & Greggio 1986), where M_B is the total mass of the binary system, $M_{Bm} = 3M_{\odot}$ and $M_{BM} = 16M_{\odot}$ are the minimum and maximum masses allowed for the adopted progenitor systems, respectively. $\mu = M_2/M_B$ is the mass fraction of the secondary and μ_m is its minimum value. The constant A represents the fraction of binary systems in the IMF which are able to give rise to SNIa explosions.

In the following chapters we will present results obtained with a detailed numerical model such as that just described and we will follow the evolution of the abundances of H, He, C, N, O, Mg, Si and Fe.

Chapter 3

The cosmological simulation

A numerical simulation integrates the Vlasov-Poisson equations in order to follow the non-linear evolution of density fluctuations. The capacity of an N-body simulation to follow the gravitational clustering is limited by the dynamical resolution, i.e. by the minimum scale of lenght and mass which can be resolved. In a cosmological simulation, in which no attempt is made to better simulate a particular region, the resolution is defined by the particle number used in the simulation itself.

To avoid as much as possible the influence of collisionalities (Aarseth 1963) all N-body algorithm performing an evaluation of the force between couples of particles needs to introduce a softening lenght ϵ. For scales lower then ϵ the gravitational force becomes constant. The softening parameter, however, implies a dissipation for small scales and, therefore, the energy is not strictly conserved. It is very important to chose the better softening parameter to have a good conservation of the energy and a minimum collisionality.

Clasically there are four main types of N-body codes:

- Particle-Particle (PP). These codes calculate the gravitational force acting on a particle considering the effect of all the other particles. In this case the particle trajectories are calculated with high precision. The computation time is $t_{CPU} \propto N^2$.

- Tree-codes. In this case the data are organized following a tree struc-

ture. The gravitational force is directly calculated only for particles belonging to the same region, while every other particle interacts only with the centre of mass of regions farther and larger. In this case $t_{CPU} \propto N\ logN$.

- Particle-Mesh (PM). These codes uses Fourier transforms to calculate the gravitational potential. Every particle interacts only with the mean field calculated on the mesh. This technique is the one with less collisionality problems and it is particularly adapt for a high number of particles; no softening is needed since here we do not have 2-body interactions.

- Particle-Particle, Particle-Mesh (P^3M). This code combines the PP and the PM. In this case the gravitational force is the sum of a term which considers the mean field on the mesh plus a contribute due to direct interaction with closed particles. This code represents a compromise between the velocity of PM codes and the accuracy of PP codes.

In the last decade more algorithms have been introduced, which improve or mix the technical characteristics of those summarized above. Among them, the most important are the Tree + PM codes (making use of a PM algorithm at large scales and of a tree code at intermediate/low ones) and AMR (Adaptive Mesh Refinements) codes. The latter use a finer grid to improve resolution where needed, for example in high density regions.

The main aim of this thesis is to study the formation and chemical evolution of spiral galaxies in a cosmological context. Thus we run a dark matter-only cosmological simulation, using the public tree-code GADGET2 (Springel 2005), in order to produce and study dark matter halos in which spiral galaxies can form. Our simulated box has a side of 24 h^{-1} Mpc. We used 256^3 particles. We adopted the standard cosmological parameters from WMAP 3-years (Spergel et al. 2007), namely $\Omega_0 = 0.275$, $\Omega_\lambda = 0.725$ and $\Omega_b = 0.041$. Each DM particle has a mass equal to $6.289 \cdot 10^7 h^{-1} M_\odot$ and the Plummer-equivalent softening length is set to 3.75 h^{-1} comoving kpc to redshift $z = 2$ and to $1.25\, h^{-1}$ physical kpc since $z = 2$. We use the public package GRAFIC (Bertschinger 1995) to set up our initial conditions. The

simulation started at redshift $z = 20$ and 28 outputs were produced. We have chosen to use a quite large spread in the redshifts at the beginning, while in the last part of the simulation, where a small change in the redshift corresponds to a large change in time, the redshifts are closer. We checked that the final mass function of DM halos and the power spectrum were in agreement with theoretical expectations.

We identified DM halos at redshift $z = 0$ using a standard friend-of-friends algorithm, with a linking length $l = 0.17$ mean (comoving) interparticle distance. After that, we determined the virial mass and radius for each DM halo, using the center of mass of the F-o-F group as the halo center. Here we define the virial radius as the radius of the sphere within which the matter density contrast is $\delta \approx 100$ times the critical density, with δ given by the cosmological parameter as in Navarro & Steinmetz (2000).

We then built the mass accretion history of our halos. To achieve this goal, we analysed our 28 outputs from redshift $z = 9.0$ to $z = 0$. We identified all DM halos in each snapshot using the procedure described above, except for the fact that we used the redshift-dependent density contrast given by Bryan & Norman (1997) to define the virial radius as a function of z. At any output z_{i+1}, we found all the progenitors of our halos at redshift z_i. We defined a halo at redshift z_{i+1} to be a progenitor of one at z_i if at least 50% of its particles belong to the candidate offspring (see e.g. Kauffmann 2001, Springel et al. 2001 for a discussion on this threshold). The mass accretion history is defined as the mass of the main progenitor of the halo as a function of redshift. Having the mass accretion histories, we were able to identify the redshift of formation (defined as the epoch at which half of the mass of the forming halos were accreted) and the redshift at which each halo experienced its last major merger (defined as an increase of at least 25% of its mass with respect to the mass of its main progenitor at the previous redshift). To identify the DM halos that can host a spiral galaxy similar to the MW we used selection criteria based on four different characteristics of the halos:

- mass between $5 \cdot 10^{11} M_{\odot}$ and $5 \cdot 10^{12} M_{\odot}$;
- spin parameter $\lambda > 0.04$;

- redshift of last major merger larger than $z = 2.5$;
- redshift of formation larger than $z = 1.0$.

We found four DM halos compatible with our selection criteria. We label them with their F-o-F group number, i.e. group 48001, group 52888, group 56004 and group 6460.

In Table 3.1 we summarize the characteristics of the halos. Figure 3.1 represents our best cosmological halo (halo 48001) at four different redshifts (z = 0.0, z = 0.5, z = 1.0 and z = 2.0).

Table 3.1: Characteristics of the chosen DM halos

Group	Mass [$10^{10} M_{\odot}$]	Spin parameter	Redshift major merger	Redshift of formation
48001	90.26	0.045	5.00	1.75 - 1.50
52888	465.75	0.059	3.75	1.50 - 1.25
56009	90.73	0.049	3.25	2.00 - 1.75
6460	61.94	0.041	2.50	1.25 - 1.00

We note that, given our simulated volume, the expected number of halos in our mass range is higher: using a Press & Schechter mass function, approximately 70 halos are expected. However, the requirement of having a "quiescent" formation history and a high spin parameter greatly reduces their number (see e.g. D'Onghia & Burkert 2004 and references therein for a discussion on this point). In this thesis we want to focus on the chemical evolution of a MW-like galaxy in its cosmological context and, therefore, we will not discuss issues connected with the angular momentum problem which arises when performing a direct simulation of the formation of a disk-like galaxy in a cosmological dark matter halo. Also, we could have obtained a larger number of halos by relaxing the third of the above constraints, but for the purpose of the present work it is more important to focus on the most promising DM halos than on obtaining statistics. So, we simply used the (few) best candidates as example halos.

Assuming that the baryonic matter follows the same accretion pattern as the dark matter, and that it represents 19% (the cosmological baryon fraction) of all the infalling matter, we obtained a final baryonic mass for the Galaxy of $1.7 \cdot 10^{11} M_{\odot}$. This approach is similar to that followed by Robertson

et al. (2005). In this way, we obtained the baryon infall law from the mass accretion history of each halo. We also considered the arithmetic mean of the infall laws of all four halos, in order to have an "average" cosmological infall law to study.

As a first approach, we assumed that the derived infall law has the same functional form for the whole Milky Way, but that the normalization constant is different for different Galactic regions. In other words, the normalization constants were obtained by reproducing the current total surface mass density at any specific galactocentric distance (see next chapter). In chapter 5, however, we try to derive infall laws having different functional form along the disk in order to obtain an inside-out formation for the disk.

Here, we do not make any attempt to model the disk formation inside the hierarchically growing DM halo, even if a cosmological simulation can follow the inside-out formation of a galactic disk (producing however a too high bulge/disk ratio, Scannapieco et al. 2008) This is undoubtedly an oversimplification of the physics involved. On the other hand, the issue of disk galaxy formation in hierarchical cosmologies is far from being solved. Any attempt to model the formation of the disk should use a number of assumptions which are currently under debate. As an example, the structure of the disk is obviously driven by the gas cooling coupled with its angular momentum content. Semi-analytical galaxy formation models (SAMs) usually assume that DM and gas share the same specific angular momentum. But this point is very controversial (see e.g. D'Onghia & Burkert 2004, D'Onghia et al. 2006, and references therein). Even direct self consistent numerical simulations are not currently able to solve the problem, which may (Governato et al 2007) or may not (Abadi et al 2003) be simply due to insufficient numerical resolution and/or an insufficiently detailed treatment of supernova feedback. Lacking a widely accepted model for the formation of the disk, we prefer to keep our model as simple as possible and to verify whether the cosmological growth of the halo is compatible with the observational constraints obtained using available data on the chemical composition of stars and gas in the Milky Way.

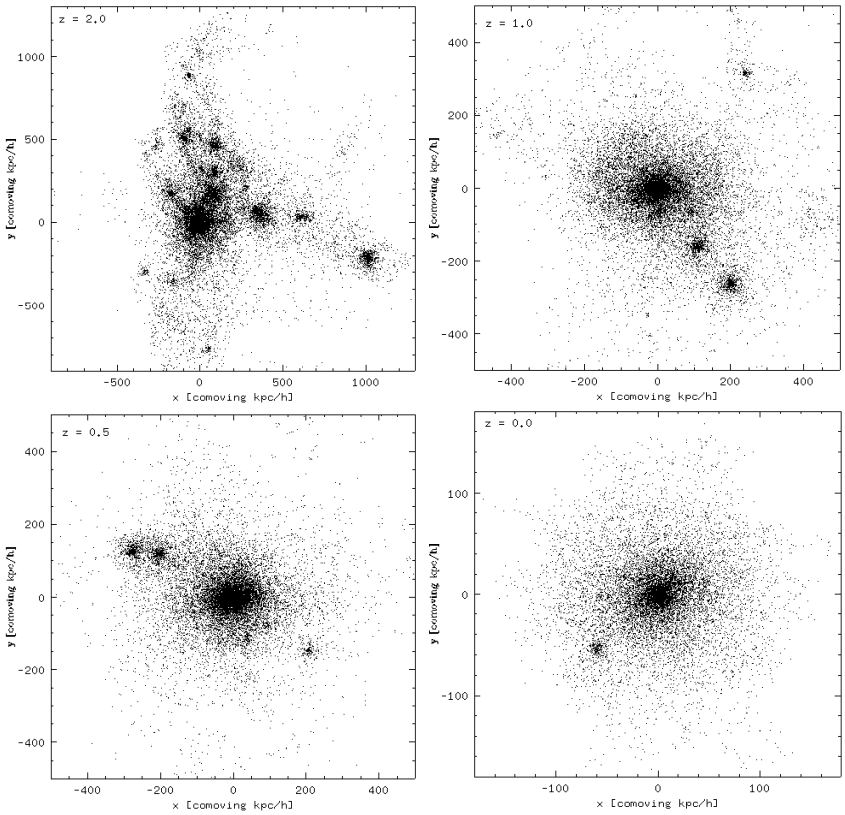

Figure 3.1: This figure represents our best cosmological halo, i.e. halo 48001, at four different redshifts (z = 2.0, z = 1.0, z = 0.5 and z = 0.0).

Chapter 4

Formation of the Milky Way in a cosmological context for the solar vicinity

In this chapter we study some cosmologically motivated infall laws to understand if the ΛCDM cosmology can reproduce the main chemical characteristics of a Milky Way-like spiral galaxy. We test several different gas infall laws, starting from that suggested in the two-infall model of Chiappini et al. (1997) for the chemical evolution of the Milky Way, but focusing on laws derived from cosmological simulations which follows a concordance ΛCDM cosmology. Moreover we also test some very simple infall laws, such as a constant and a linear infall law. These laws, probably, are not realistic, but they have the advantage to be simple and, therefore, they can be used to test the chemical evolution model before to adopt the cosmological infall laws.

To begin, we first give some information about the two infall model of Chiappini et al. (1997) and the nucleosynthesis prescriptions adopted.

4.1 The two infall model

Chiappini et al. (1997) were the first authors which proposed the existence of two main infall episodes for the formation of the Galactic components. They assumed that the first infall episode was responsible for the formation of the

halo and thick-disk stars, while the second infall episode formed the thin-disk component, with a longer timescale. The authors also included in the model a threshold in the gas density below which the star formation process stops.

In the model by Chiappini et al. (1997) the Galactic disk is approximated by a series of concentric annuli, 2 kpc wide, without exchange of matter between them. The basic equations are the same as in Matteucci & François (1989). The two main differences between the model by Chiappini et al. (1997) and Matteucci & François (1989) are the rate of mass accretion and the rate of star formation. Moreover, in the model by Chiappini et al. (1997) the material accreted by the Galactic thin disk comes mainly from extragalactic sources. These extragalactic sources could include, for instance, the high velocity clouds, the Magellanic Stream or a major accretion episode (see Beers & Sommer-Larsen 1995 and references therein). The two models have in common the "inside-out" formation of the thin disk, in the sense that both assume that the timescale for the disk formation increase with galactocentric distance (see section 5). This choice was dictated by the necessity of reproducing the abundance gradients along the Galactic disk.

The main equations regulating the model of Chiappini et al. (1997) are the same as described in chapter 2 (see eq. 2.23), except for the fact that they did not consider gas outflow.

The SFR adopted is a Schmidt (1955) law with a dependence on the surface gas density ($k = 1.5$, see Kennicutt 1998) and also on the total surface mass density (see Dopita & Ryder 1994). In particular, the SFR is based on the law originally suggested by Talbot & Arnett (1975) and then adopted by Chiosi(1980):

$$\psi(r,t) = \nu \left(\frac{\Sigma(r,t)\Sigma_{gas}(r,t)}{\Sigma(r_\odot,t)^2} \right)^{(k-1)} \Sigma_{gas}(r,t)^k, \tag{4.1}$$

where the constant ν is the efficiency of the star formation process and is expressed in Gyr^{-1}: in particular, $\nu = 2\,Gyr^{-1}$ for the halo and $1\,Gyr^{-1}$ for the disk ($t \geq 1\,Gyr$). The total surface mass density is represented by $\Sigma(r,t)$, $\Sigma(r_\odot,t)$ is the total surface mass density at the solar position, assumed to be $r_\odot = 8$ kpc (Reid 1993). The quantity $\Sigma_{gas}(r,t)$ represents the surface gas density and t represents the time. These choices of values for the parameters

allow the model to fit the observational constraints very well, in particular in the solar vicinity.

The IMF is that of Scalo (1986) normalized over a mass range of 0.1-100 $M_{\odot}$, assumed to be constant in space and time.

4.2 Nucleosynthesis prescriptions

One of the most important ingredients for chemical evolution models is represented by the nucleosynthesis prescriptions and consequently by the stellar yields.

The single stars in the mass range 0.8 $M_{\odot} \leq M \leq 8\ M_{\odot}$ (low and intermediate-mass stars) contribute to the Galactic enrichment through planetary nebula ejection and quiescent mass loss. They enrich the interstellar medium mainly in He, C, N and heavy s-process elements (e.g. Cescutti et al. 2006). We adopt the stellar yields for low and intermediate mass stars of van den Hoek & Groenewegen (1997) computed as functions of stellar metallicity, their case with variable mass loss (Chiappini et al. 2003).

These stars are also the progenitor of Type Ia supernovae (SNe), if they are in binary systems that originate from carbon deflagration of C-O white dwarfs. We adopt the single-degenerate progenitor scenario (Whelan & Iben, 1973; Han & Podsiadlowski 2004). Type Ia SNe contribute a substantial amount of Fe ($\sim$ 0.6 $M_{\odot}$ per event) and Fe-peak elements as well as non negligible quantities of Si and S. They also produce other elements, such as O, C, Ne, Ca, Mg and Ni, but in very small amounts compared to Type II SNe. We assume the stellar yields for Type Ia SNe from Iwamoto et al. (1999).

Massive stars (8 $M_{\odot} < M \leq 100\ M_{\odot}$) are the progenitor of core-collapse SNe which can be either Type II SNe or Type Ib/c SNe. These latter can arise from binary systems or Wolf-Rayet stars whereas Type II SNe originate from the massive stars in the lower mass range. Type II SNe mainly produce the so called α-elements, such as O, Mg, Ne, Ca, S and Si and Ti, but also some Fe and Fe-peak elements although in smaller amounts than Type Ia SNe. We adopt the stellar yields for massive stars by Woosley & Weaver (1995) with the suggested modifications of François et al. (2004).

However, the most important modifications concern some Fe-peak elements, except Fe itself, whereas for the α-elements, with the exception of Mg which has been increased relative to the original yields, the yields are substantially unmodified. The modifications of the yields in François et al. (2004) were required to fit at best and at the same time the [element/Fe] versus [Fe/H] patterns and the solar absolute abundances. We keep the same prescriptions here.

In this thesis we adopt the solar abundances by Asplund et al. (2005).

4.3 The infall laws

In testing the accretion laws, we started by adopting the two-infall law model, as suggested by Chiappini et al. (1997). This law presents two distinct peaks. During the first peak the halo and thick disk formed whereas during the second peak the thin disk was assembled. The two accretion events are considered to be independent from each other and only a very small fraction of the gas lost from the halo was assumed to have fallen onto the disk. The infall law that we indicate as $A(r,t)$ is expressed as:

$$A(r,t) = a(r)e^{-t/\tau_H(r)} + b(r)e^{-(t-t_{max})/\tau_D(r)}\,[M_\odot\ pc^{-2}\ Gyr^{-1}], \qquad (4.2)$$

where $a(r)$ and $b(r)$ are two parameters fixed by reproducing the total present time surface mass density along the Galactic disk. In particular, in the solar vicinity the total surface mass density $\Sigma_{tot} = 51 \pm 6 M_\odot\ pc^{-2}$ (see Boissier & Prantzos 1999). $t_{max} = 1.0$ Gyr is the time for the maximum infall on the thin disk, $\tau_H = 2.0$ Gyr is the time scale for the formation of the halo thick-disk and $\tau(r)$ is the timescale for the formation of the thin disk and is a function of the galactocentric distance (inside-out formation, Matteucci and François 1989; Chiappini et al. 2001). In particular, it is assumed that:

$$\tau_D = 1.033r(kpc) - 1.267\,[Gyr]. \qquad (4.3)$$

Besides this infall law, we tested other possible laws, such as a time constant infall rate. In particular:

$$A(r,t) = 3.80\,[M_\odot\ pc^{-2}\ Gyr^{-1}]. \tag{4.4}$$

This law is probably not realistic although Naab & Ostriker (2006) concluded that an almost constant infall law over the disk lifetime was to be preferred. Here we adopted it mainly for the purpose of comparison with more realistic laws. We adopted that particular value of the infall rate in order to reproduce the current infall rate (see Table 4.2), as well as the current total surface mass density.

The third infall law we tested is a linear infall law, given by:

$$A(r,t) = 6.57 - 0.4 \cdot t\,[M_\odot\ pc^{-2}\ Gyr^{-1}]. \tag{4.5}$$

Again, we used this particular expression in order to reproduce the current Σ_{tot} and infall rate.

The fourth adopted infall law is the same as that of Chiappini et al. (1997) but with pre-enriched infalling gas. The metallicity of the infalling gas which forms the disk was assumed to be 10 times lower than the present time interstellar medium (ISM) metallicity while the infalling gas which forms the halo is still primordial. The assumed chemical composition of the infalling gas does not assume solar abundance ratios but reflects the composition of the halo-thick disk.

Then, we tested the infall laws derived from the cosmological simulations performed with GADGET2 (Springel 2005), as described before. In particular, to derive the cosmological infall law we proceeded in the following way:

$$A(r,t) = a(r)0.19\frac{dM_{DM}}{dt}[M_\odot\ pc^{-2}\ Gyr^{-1}], \tag{4.6}$$

where 0.19 is the cosmological baryonic fraction and $a(r)$ is a normalization constant fixed to reproduce the current total surface mass density along the disk, in analogy with eq. (4.2). For the solar ring $a(r) = \frac{\Sigma(r_\odot,t_G)}{M_{Gal}}$, with $M_{Gal} = 0.19 M_{DM}$ being the baryonic mass of our Galaxy and t_G the Galactic lifetime. In Figure 4.1 we show the values of $a(r)$ versus the galactocentric distance.

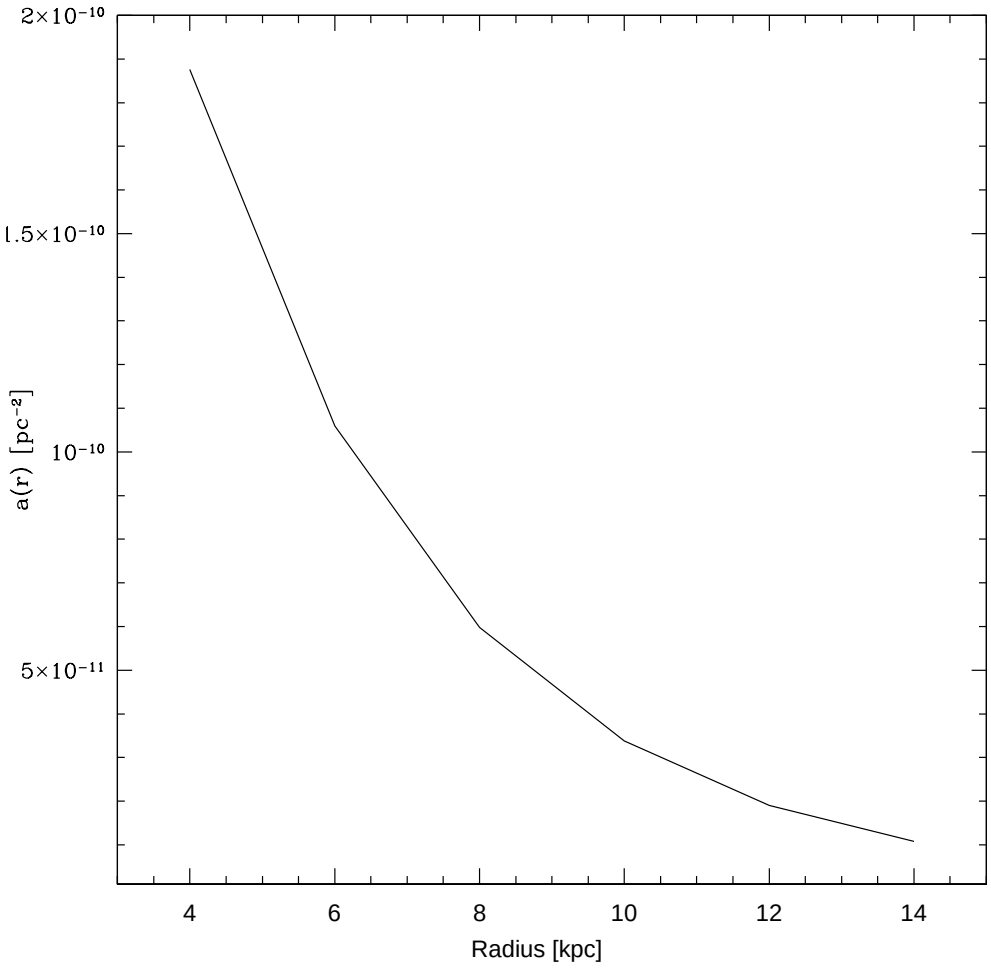

Figure 4.1: $a(r)$ vs radius. This normalization constant is fixed to reproduce the present time total surface mass density along the disk (see eq. 4.6).

One infall law is given by the arithmetic average of the infall laws derived for the four halos and the last infall law is that suggested by Naab & Ostriker (2006). In Table 4.1 we show the model parameters. The different models are identified mainly by their infall histories.

Our infall laws for the solar region (8 kpc from the Galactic center) are

Table 4.1: Models parameters. In the first column is the number of the model, in the second one the adopted infall law, in the third the time scale for the halo, in the fourth that for the disk and in the fifth the type of infalling gas. All the models adopt a threshold gas density for star formation in the disk of $7 M_{\odot} pc^{-2}$ and have the same nucleosynthesis prescriptions. The model by Naab & Ostriker (2006) is the only one that has a threshold also during the formation of the halo. Note that our best cosmological model is Model 5.

Model	Infall law $[M_{\odot} pc^{-2} Gyr^{-1}]$	τ halo [Gyr]	τ disk [Gyr]	Gas t = 0
1	Two-infall law	0.8	7	Primordial
2	3.80	-	-	Primordial
3	$6.57 - 0.40 \cdot T$	-	-	Primordial
4	Two-infall law	0.8	7	Enriched (1/10 Z_{today})
5	Group 48001	-	-	Primordial
6	Group 52888	-	-	Primordial
7	Group 56009	-	-	Primordial
8	Group 6460	-	-	Primordial
9	Mean	-	-	Primordial
10	Naab & Ostriker	-	-	Primordial

shown in Figure 4.2. The infall law derived for the best halo selected as representative of the Milky Way halo is very similar to the two-infall law by Chiappini et al. (1997).

We selected our best halo by choosing the one which has a very high redshift of the last major merger. This is to ensure the correct spin parameter for a Milky Way-like galaxy. The assembly history of this particular halo presents two distinct accretion peaks which produce an infall law very similar to the two-infall model by Chiappini et al. (1997). The only difference to the two-infall model is that in this case the two peaks are placed at a lower redshifts. After the two main peaks there are other smaller peaks. All models predict a current infall rate which is in good agreement with the observed one, as quoted by Naab & Ostriker (2006). Thus, according to the infall laws derived from cosmological simulations, the Galaxy had some large infall episodes at high redshift, followed by smaller ones.

In Fig. 4.3 we present the total surface mass density Σ_{tot}, expressed as

$M_{\odot}pc^{-2}$, as a function of time for all the models. Once again Models 1 and 4 (two-infall model with primordial and enriched infall, respectively) have the same Σ_{tot}. The linear model predicts the largest final amount of matter, equal to 51.88 $M_{\odot}$ pc^{-2}. The constant model has a linear growth (in this case Σ_{tot} is the integral of a constant infall law) and produces 49.98 $M_{\odot}$ pc^{-2}. Model 10, i.e. the model of Naab & Ostriker (2006), is the only one that starts to increase the amount of matter very slowly (in the solar neighbourhood). After 5 Gyr from the Big Bang it only reached 6.00 $M_{\odot}$ pc^{-2}. The cosmological models produce results that are quite similar to the two-infall model. At the beginning their growth is slower but after $\sim$ 3 - 3.5 Gyr their Σ_{tot} increases with a steeper slope, due to the peaks in the infall law.

The basic equations to follow the chemical evolution of our models can be seen in chapter 2.

4.4 Results for the solar neighborhood

We now present the chemical evolution obtained results. They are shown in Tables 4.2, 4.3 and 4.4. In Table 4.2 we show the predicted current star formation rates, the current infall and the current SNIa and SNII rates, compared with the corresponding observational values. In Table 4.3 we show the total amount of gas and the number of stars, the $\Sigma_{gas}/\Sigma_{tot}$ and the total surface mass density in a ring of 2 kpc centered at the Sun's galactocentric distance (8 kpc). Table 4.4 presents the predicted solar absolute abundances by mass for Fe, C, Mg, N, O and Si, namely the abundances in the ISM at the time of birth of the solar system 4.5 Gyr ago, compared with the observed ones by Asplund et al. (2005).

Figure 4.4 shows the star formation rate as a function of cosmic time for all the models. At high redshift there is a gap in the SFR for some of the models. This gap is due to the adoption of a threshold in the surface gas density below which star formation does not occur. In all models we have adopted a threshold equal to 7.0 $M_{\odot}$ pc^{-2} during the formation of the thin disk. Model 10, instead, adopting the infall law suggested by Naab & Ostriker (2006), has a star formation threshold equal to 7.0 $M_{\odot}$ pc^{-2} both for the halo and the disk.

Table 4.2: Current values for all the models and observed values as reported in Boissier & Prantzos (1999) and Chiappini et al. (2001).

Model	SFR $[M_\odot pc^{-2} Gyr^{-1}]$	Infall $[M_\odot pc^{-2} Gyr^{-1}]$	SNII rate $[pc^{-2} Gyr^{-1}]$	SNIa rate $[pc^{-2} Gyr^{-1}]$
1	2.66	1.100	0.00900	0.00330
2	4.55	3.800	0.01928	0.00411
3	2.81	1.320	0.01194	0.00391
4	2.66	1.100	0.00900	0.00332
5	2.65	0.528	0.00584	0.00366
6	2.69	2.273	0.01140	0.00347
7	2.65	0.126	0.00229	0.00366
8	4.01	0.998	0.01712	0.00412
9	2.69	0.979	0.01147	0.00381
10	4.72	3.406	0.02002	0.00397
Boissier & Prantzos (1999)	2-5	1.0-3.3	0.02	0.0042 ± 0.0016
Chiappini et al. (2001)	2.6	1.0	0.008	0.004

From Figure 4.4 we deduce that the constant infall model predicts a growing star formation rate at low redshifts, a trend that is not predicted by the other laws. On the other hand, the cosmological best model (Model 5) predicts a very important peak between 3 and 6 Gyr, which should correspond to the formation of the bulk of the stars in the thin disk. This peak is directly related to the trend of the infall law. After 10 Gyr from the Big Bang the threshold is easily reached in most of the models, thus causing the SFR to have an oscillating behavior.

In Figure 4.5 we present the SNIa rates for all the models. The cosmological law of Model 5 predicts a peak for the SNIa rate at about 6 Gyr. This is due to the fact that the SFR in this model has a large peak at about 5 Gyr. Thanks to this peak, many stars form and many SNIa explode after a delay of about 1 Gyr. All the models predict a SNIa rate between 0.003 and 0.004 SNe $pc^{-2}\ Gyr^{-1}$, in good agreement with the value given by Boissier & Prantzos (1999), i.e. 0.0042 ± 0.0016 .

We do not show the rates of SNe II since their behavior is like that of the SFR. Type II SNe are produced by massive stars that live only a few million years. For this reason, the behavior of the SNII rate is equivalent to that of the SFR.

Table 4.3: Current values for all the models and observed values as reported in Boissier & Prantzos (1999) and Chiappini et al. (2001)

Model	Gas $[M_{\odot}pc^{-2}]$	Stars $[M_{\odot}pc^{-2}]$	$\frac{\Sigma_{gas}}{\Sigma_{tot}}$	Σ_{tot} $[M_{\odot}pc^{-2}]$
1	7.00	35.24	0.1444	48.46
2	10.11	35.09	0.2024	49.98
3	7.42	38.66	0.1431	51.88
4	7.00	35.24	0.1444	48.46
5	6.99	36.13	0.1439	48.55
6	7.06	35.60	0.1455	48.53
7	7.00	36.69	0.1442	48.56
8	9.21	34.75	0.2056	48.55
9	7.06	36.32	0.1455	48.55
10	10.29	34.29	0.2099	49.04
Boissier & Prantzos (1999)	13 ± 3	35 ± 5	0.15 - 0.25	51 ± 6
Chiappini et al. (2001)	7.0	36.3	0.13	53.85

In Figure 4.6 we present the predicted $[Fe/H]$ as a function of time for all models. The model with a constant infall law (Model 2) and Model 10 never reach the solar abundance. The reason is that in both models the infall rate during the whole galactic lifetime is probably overestimated. In the model by Chiappini et al. (1997) (our Model 1) $[Fe/H]$ reaches a local peak at 1 Gyr, then decreases slightly to increase again. The small depression in $[Fe/H]$ is due to the predicted gap in the SFR just before the formation of the thin disk. The second infall episode coupled with the halt in the SF produces a decrease of $[Fe/H]$. We can see the same behavior in the cosmological models. In particular in Model 5 the peak is followed by a deeper depression of $[Fe/H]$ and this is due to the longer gap in the SFR predicted by this model (1-2 Gyr) as opposed to that predicted by Model 1, which is less than 1 Gyr. This is an important prediction and it can be tested via chemical abundances. Both Gratton et al. (1996) and Furhmann (1998) detected such an effect in the $[Fe/O]$ vs. $[O/H]$ and $[Fe/Mg]$ vs. $[Mg/H]$, respectively.

A very important constraint for the chemical evolution of the galaxies is represented by the G-dwarf metallicity distribution. This is the relative

Table 4.4: Predicted and observed solar abundances by mass (after 8.64 Gyr from the Big Bang)

Model	Fe	C	Mg	N	O	Si
1	0.162E-02	0.156E-02	0.774E-03	0.121E-02	0.592E-02	0.980E-03
2	0.987E-03	0.119E-02	0.585E-03	0.932E-03	0.461E-02	0.665E-03
3	0.149E-02	0.135E-02	0.778E-03	0.105E-02	0.602E-02	0.940E-03
4	0.111E-02	0.157E-02	0.691E-03	0.121E-02	0.547E-02	0.771E-03
5	0.169E-02	0.199E-02	0.797E-03	0.142E-02	0.608E-02	0.102E-02
6	0.917E-03	0.140E-02	0.604E-03	0.105E-02	0.483E-02	0.653E-03
7	0.107E-02	0.168E-02	0.701E-03	0.124E-02	0.559E-02	0.761E-03
8	0.126E-02	0.212E-02	0.796E-03	0.144E-02	0.635E-02	0.879E-03
9	0.111E-02	0.173E-02	0.716E-03	0.127E-02	0.570E-02	0.783E-03
10	0.531E-03	0.102E-02	0.439E-03	0.784E-03	0.362E-02	0.432E-03
Asplund & al. (2005)	0.116E-02	0.217E-02	0.601E-03	0.623E-03	0.540E-02	0.669E-03

number of G-dwarf stars as a function of $[Fe/H]$. We have used the data from Rocha-Pinto & Maciel (1996), Kotoneva (2002), Jorgensen (2000) and Wyse (1995). Our predicted metallicity distributions are shown in Figure 4.7. From this figure, it is clear that Model 10 predicts insufficient high metallicity stars. On the other hand, some of the cosmological models such as Model 7 and Model 8 predict too many metal-poor stars. Our best cosmological model, i.e. Model 5, shows a bimodal metallicity distribution, which is clearly at odds with the data. It is interesting to see that Model 9 gives a very good fit of the G-dwarf metallicity distribution.

The last constraint we study concerns the chemical abundances of several elements, such as O, Mg, Si, N and C. As it can be seen, abundance ratios at low metallicities depend essentially only on the stellar yields and so it is not surprising that the different models predict very similar results.

In Figure 4.8 the $[O/Fe]$ as a function of $[Fe/H]$ can be seen. Here, the range of $[Fe/H]$ has been restricted to -2.0 to $+0.3$ dex in order to better see the predictions relative to the transition between the halo-thick disk and the thin disk. In Figure 4.9 we show the same plots but for the whole range of $[Fe/H]$ down to -4.0 dex.

In Figure 4.8 one can see that cosmological models have a similar behavior to the model by Chiappini et al. (1997), except for a longer gap in the SF, which produces a loop in the predicted curves. Such loops arise when SF

stops, the α-elements are no longer produced whereas Fe continues to be produced. This induces the $[O/Fe]$ to decrease and also the $[Fe/H]$ ratio to decrease to a lesser extent, because of the accretion of primordial gas. Then when SF starts again the $[O/Fe]$ again increases. This loop is very prominant in some models and is not in agreement with the data, although some spread is present. Model 9 predicts a discontinuity in the $[O/Fe]$ vs. $[Fe/H]$ diagram, which happens at too low $[Fe/H]$. Observations of Feltzing and collaborators predict a discontinuity around $[Fe/H]$ = -0.5 which is well reproduced by the C97 model. Model 4, which is the same as Chiappini et al's model but with the pre-enriched gas, is acceptable. This is due to the fact that the metallicity of the pre-enriched infalling gas is not so different from the metallicity of the primordial infalling gas.

Figures 4.10 and 4.11 present the $[Mg/Fe]$ and the $[Si/Fe]$ as a function of $[Fe/H]$. The data in Figures 4.8, 4.9, 4.10 and 4.11 are from Cayrel et al. (2004) for the very metal poor stars and from the compilation of François et al. (2004) for all the others. Once again all the considerations made above for $[O/Fe]$ are valid for these other α-elements.

Two other important elements are C and N. It is important to underline that the results for C and N are much more uncertain than for the other elements discussed before since in this case the yields are extremely stellar model dependent. Figures 4.12 and 4.13 show the behavior of $[C/Fe]$ and $[N/Fe]$ as a function of $[Fe/H]$. The data in Figure 4.12 are from Spite et al. (2005) (magenta points), Carbon et al. (1987) (red points), Clegg, Lambert & Tomkin (1981) (cyan points), Laird (1985) (black points) and Tomkin et al. (1995) (green points). Figure 4.13 presents the data from Spite et al. (2005) (magenta points), Israelian et al. (2004) (blue points), Carbon et al. (1987) (red points), Clegg, Lambert & Tomkin (1981) (cyan points) and Laird (1985) (black points). From Figure 4.12 it can be seen once again that the cosmological models are very similar to the model by Chiappini et al. (1997). The predicted curves are different only for values of $[Fe/H]$ higher than -1.5 dex. The same holds for the $[N/Fe]$. In both cases, cosmological models have a particular behavior at high metallicities. This behavior is common to all the elements analysed and is due to the gap in the SFR at about 1 Gyr, as discussed before. In the cosmological models

this effect is larger because of the longer duration of the gap. However in the case of $[C/Fe]$ and $[N/Fe]$ we cannot draw any firm conclusion because of the large spread in the data.

Figures 4.14, 4.15 and 4.16 present the results obtained by using a different infall law, derived from the cosmological simulation but selecting different parameters. In this case we selected a halo which is not expected to produce a spiral galaxy, so we looked for a spin parameter lower than 0.04, a redshift of the last major merger lower than 2.5 and a redshift of formation lower than 1.0. Such a halo is perhaps more appropriate for an elliptical or S0 galaxy. We found a halo with the following characteristics:

- mass $= 2.15 \cdot 10^{12} M_{\odot}$
- $\lambda = 0.029$
- redshift of major merger = 0.50
- redshift of formation = 0.75 - 0.63.

Figure 4.14, 4.15 and 4.16 compare the results from this halo with Model 1 (two-infall law) and Model 5 (our best cosmological choice). The infall law is very different. In particular, it has a major peak at a redshift of about 0.3. This produces a peak at the same redshift in the star formation rate and, of course, in the SNII rate. Moreover, there is a strong depression in the $[Fe/H]$ ratio between 1.8 and 3 Gyr from the beginning of the simulation, difficult to reconcile with observations.

In Figures 4.15 and 4.16 we show the results for the $[O/Fe]$ and for the G-dwarf metallicity distribution. The main difference between this halo and Models 1 and 5 is that the loop placed at $[Fe/H] \sim -1.0$ is longer and predicts low values of $[O/Fe]$ at low $[Fe/H]$, which is not observed in Galactic stars. As far as the G-dwarf metallicity distribution is concerned, the halo forms too many stars with low metallicity as a consequence of the deep depression in the $[Fe/H]$ ratio (see the plot on the bottom right part of Figure 4.14), again not in agreement with the data, and resembles an early-type galaxy. This example confirms the importance of the cosmological assembly history of the DM halo in determining not only the morphological parameters of the galaxy it hosts, but also its chemical properties.

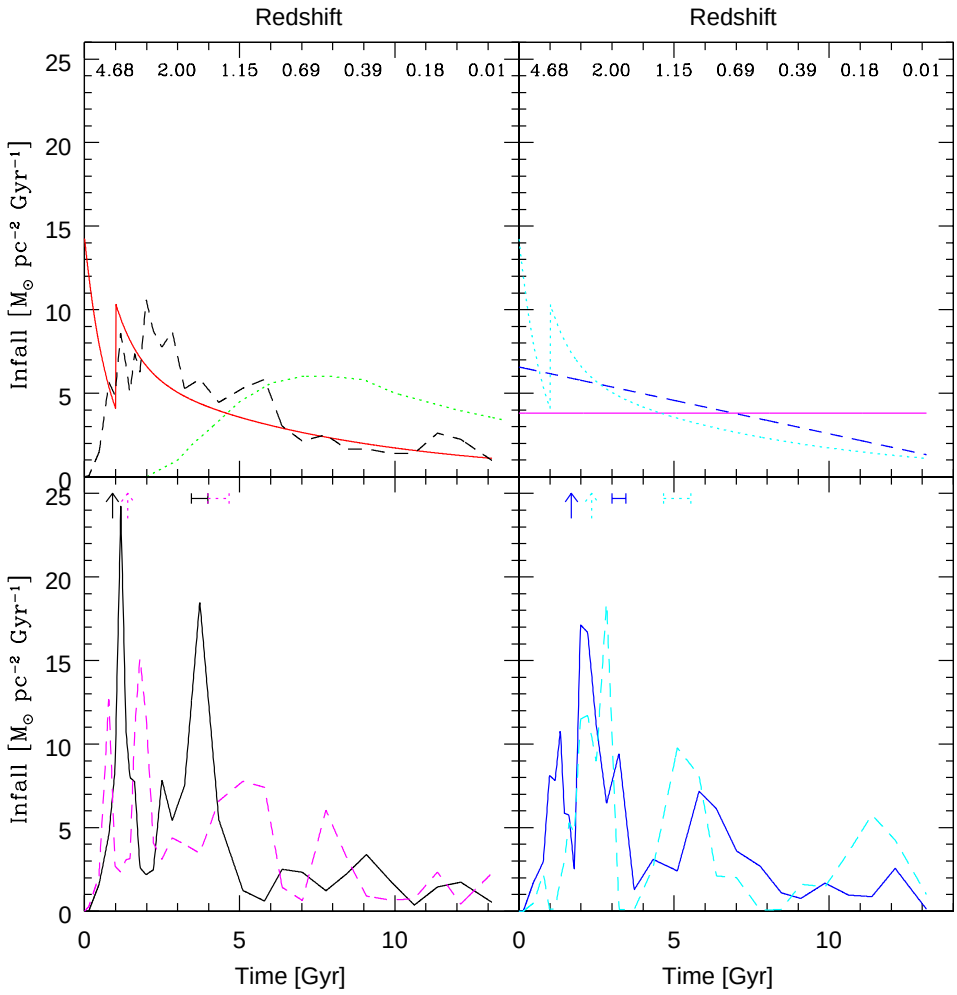

Figure 4.2: Infall vs time. Upper left panel: red solid line is the two-infall model (Model 1); black dashed line is the cosmological mean model (Model 9); green dotted line is the model by Naab & Ostriker (2006) (Model 10). Upper right panel: magenta solid line is the constant infall model (Model 2); blue dashed line is the linear infall model (Model 3); cyan dotted line is the pre-enriched model (Z_{inf} = 1/10 Z_{today}, Model 4). Bottom left panel: black solid line is Model 5; magenta dashed line is Model 6. Bottom right panel: blue solid line is Model 7; cyan dashed line is Model 8. In the bottom left panel the black solid arrow represents the redshift of last major merger for Model 5, the magenta dotted arrow the redshift of last major merger for Model 6, the black solid interval the redshift of formation for Model 5 and the magenta dotted interval the redshift of formation for Model 6. In the bottom right panel the blue solid arrow represents the redshift of last major merger for Model 7, the cyan dotted arrow the redshift of last major merger for Model 8, the blue solid interval the redshift of formation for Model 7 and the cyan dotted interval the redshift of formation for Model 8.

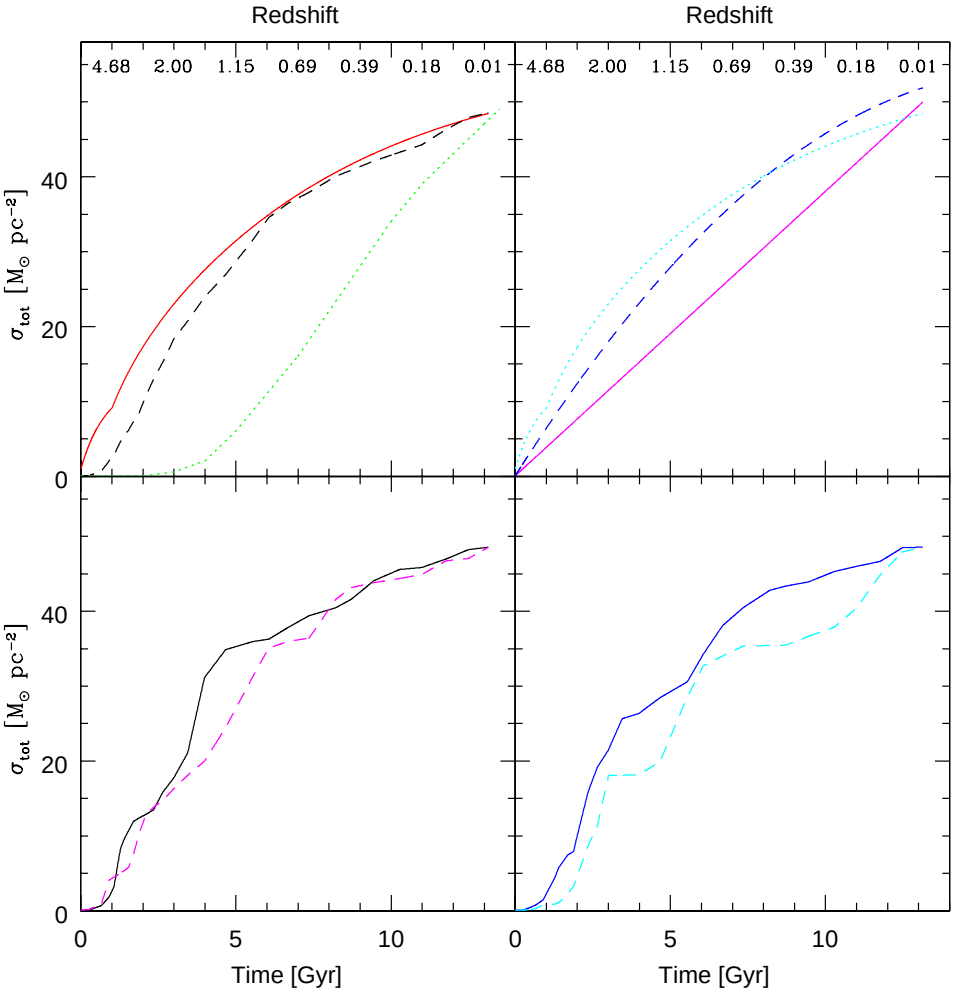

Figure 4.3: Σ_{tot} vs time. Upper left panel: red solid line is the two-infall model (Model 1); black dashed line is the cosmological mean model (Model 9); green dotted line is the model by Naab & Ostriker (2006) (Model 10). Upper right panel: magenta solid line is the constant infall model (Model 2); blue dashed line is the linear infall model (Model 3); cyan dotted line is the pre-enriched model ($Z_{inf} = 1/10\ Z_{today}$, Model 4). Bottom left panel: black solid line is Model 5; magenta dashed line is Model 6. Bottom right panel: blue solid line is Model 7; cyan dashed line is Model 8.

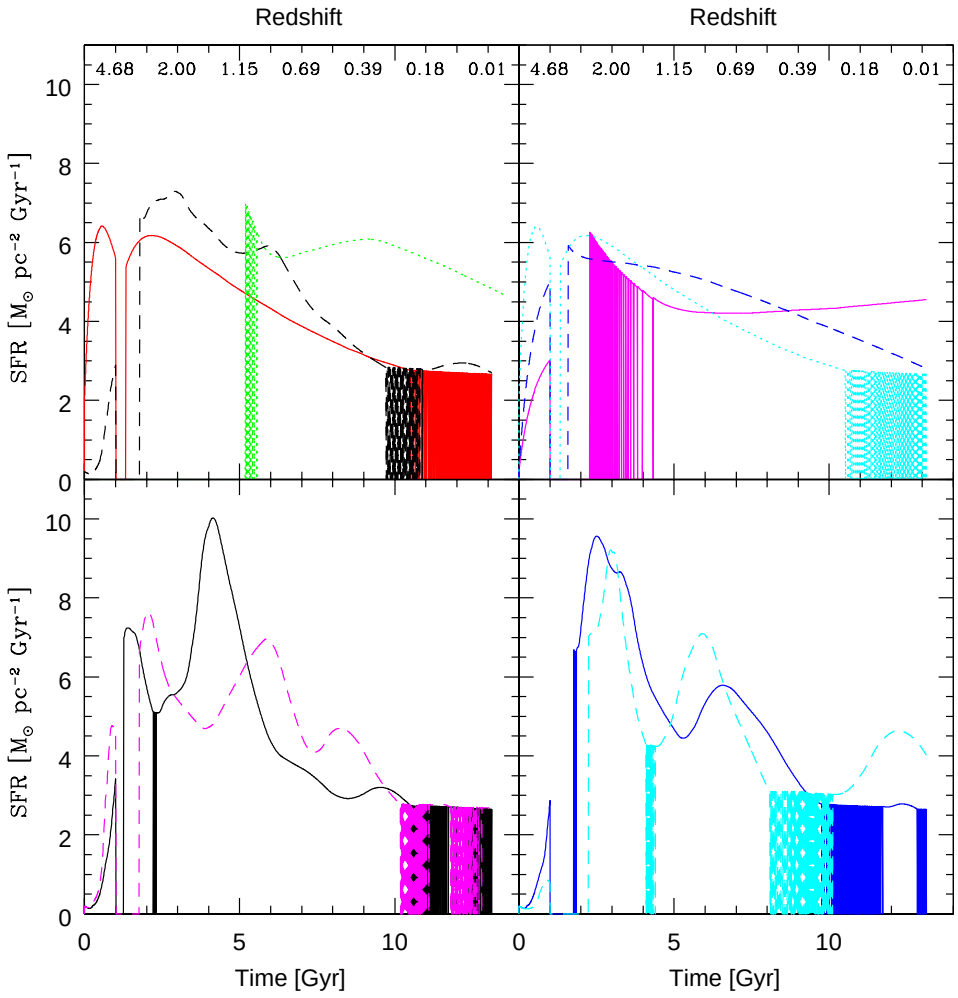

Figure 4.4: SFR vs time. Upper left panel: red solid line is the two-infall model (Model 1); black dashed line is the cosmological mean model (Model 9); green dotted line is the model by Naab & Ostriker (2006) (Model 10). Upper right panel: magenta solid line is the constant infall model (Model 2); blue dashed line is the linear infall model (Model 3); cyan dotted line is the pre-enriched model (Z_{inf} = 1/10 Z_{today}, Model 4). Bottom left panel: black solid line is Model 5; magenta dashed line is Model 6. Bottom right panel: blue solid line is Model 7; cyan dashed line is Model 8.

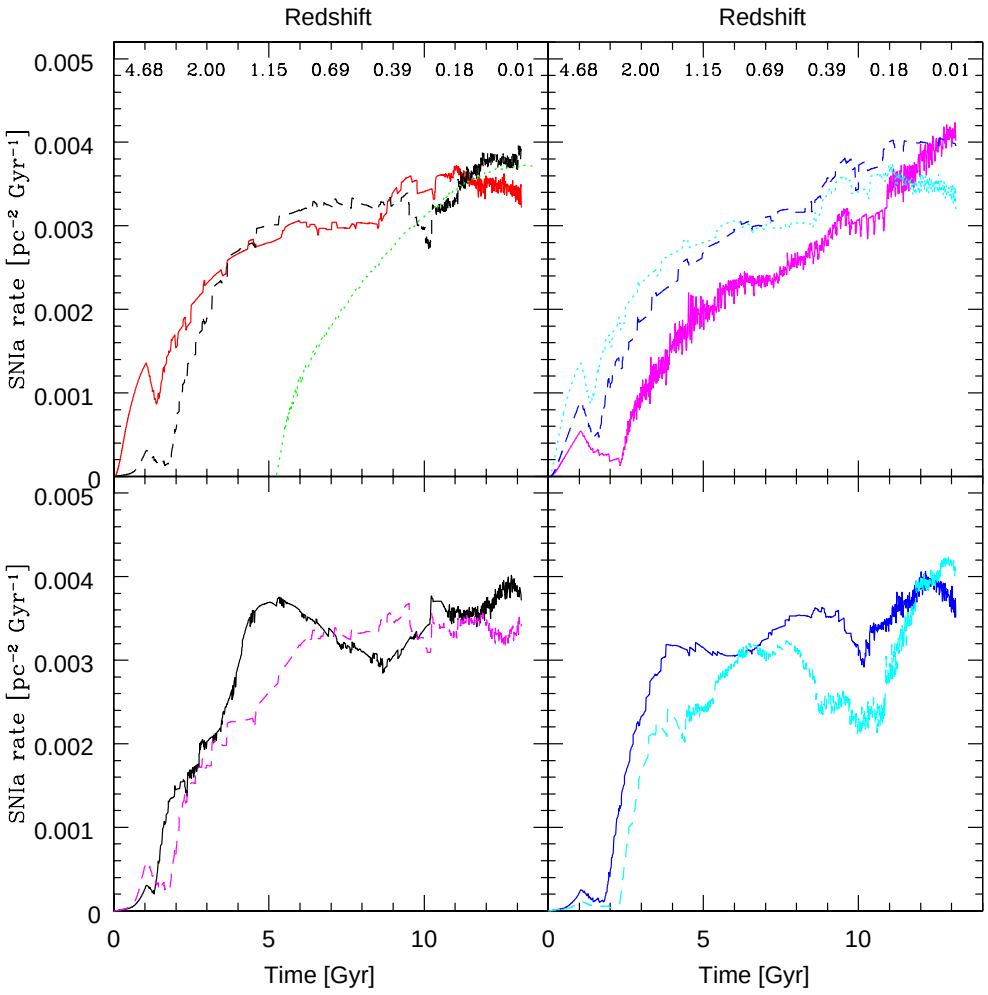

Figure 4.5: SNIa rate vs time. Upper left panel: red solid line is the two-infall model (Model 1); black dashed line is the cosmological mean model (Model 9); green dotted line is the model by Naab & Ostriker (2006) (Model 10). Upper right panel: magenta solid line is the constant infall model (Model 2); blue dashed line is the linear infall model (Model 3); cyan dotted line is the pre-enriched model ($Z_{inf} = 1/10\ Z_{today}$, Model 4). Bottom left panel: black solid line is Model 5; magenta dashed line is Model 6. Bottom right panel: blue solid line is Model 7; cyan dashed line is Model 8.

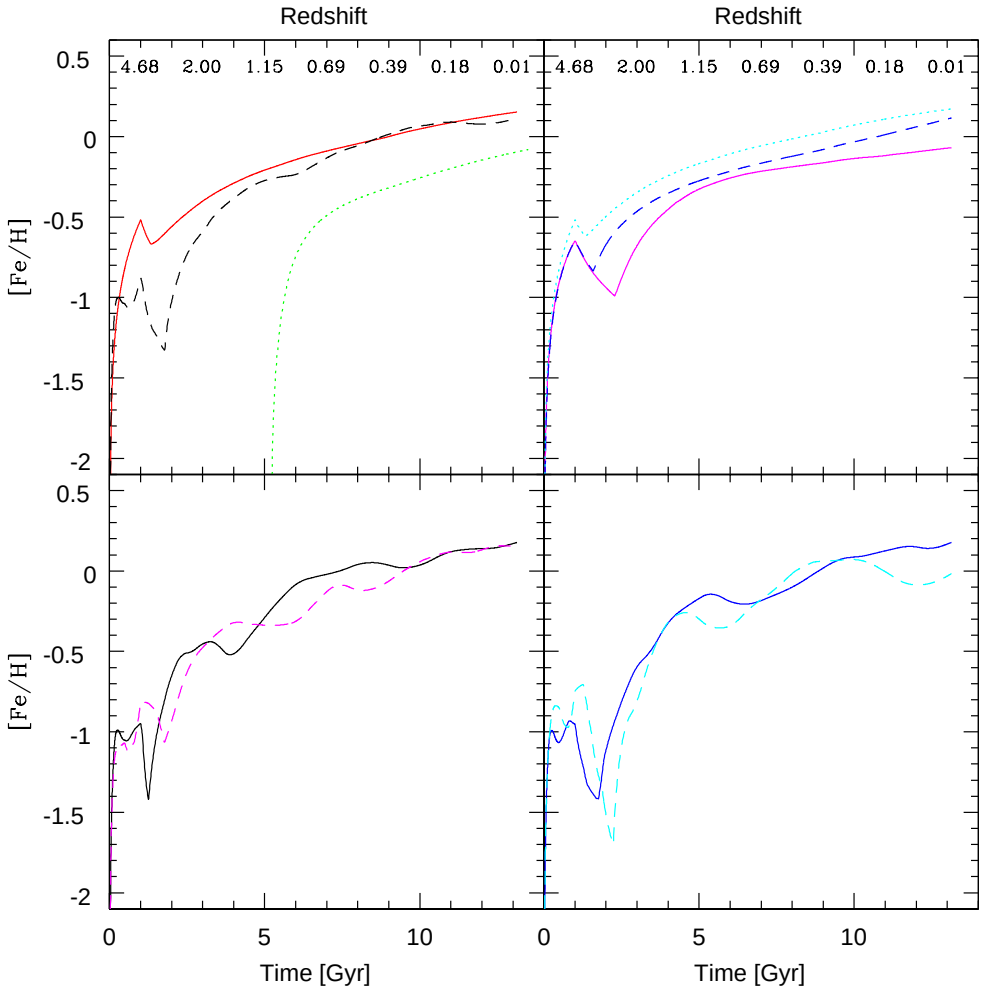

Figure 4.6: $[Fe/H]$ vs time. Upper left panel: red solid line is the two-infall model (Model 1); black dashed line is the cosmological mean model (Model 9); green dotted line is the model by Naab & Ostriker (2006) (Model 10). Upper right panel: magenta solid line is the constant infall model (Model 2); blue dashed line is the linear infall model (Model 3); cyan dotted line is the pre-enriched model ($Z_{inf} = 1/10\ Z_{today}$, Model 4). Bottom left panel: black solid line is Model 5; magenta dashed line is Model 6. Bottom right panel: blue solid line is Model 7; cyan dashed line is Model 8.

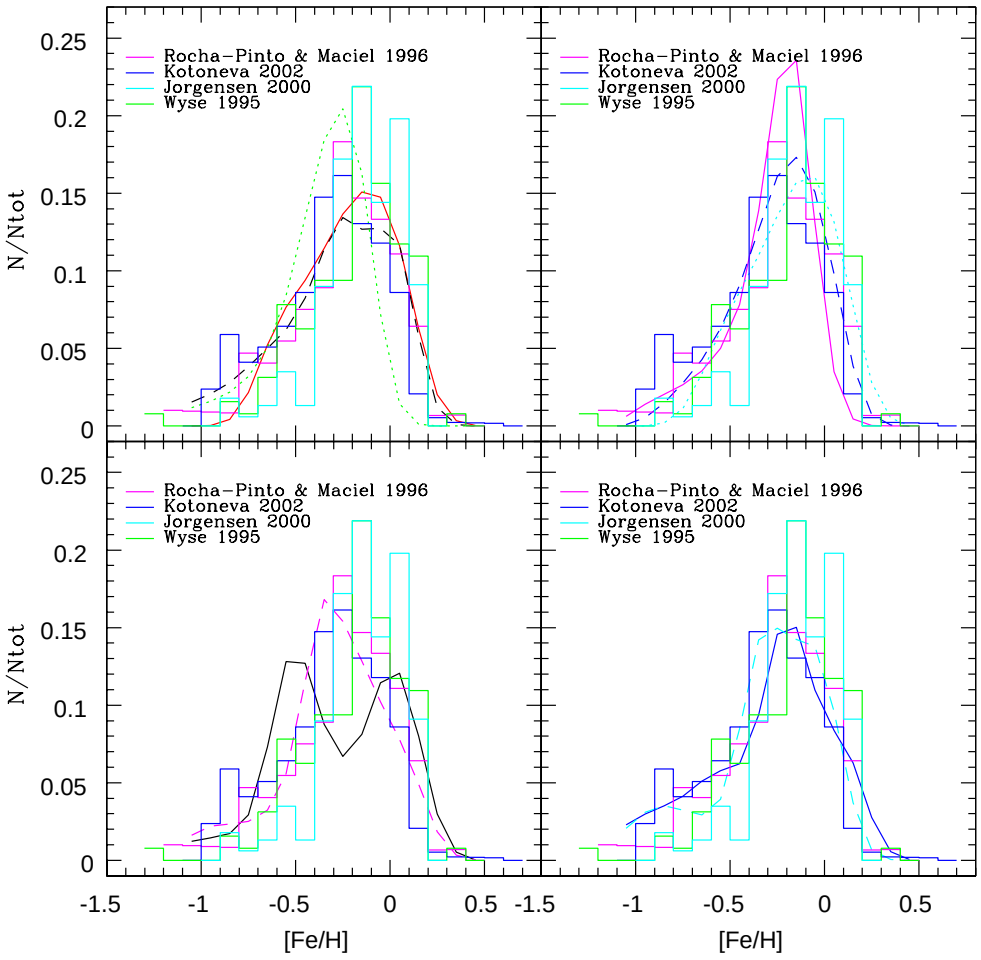

Figure 4.7: G-dwarf metallicity distribution. Upper left panel: red solid line is the two-infall model (Model 1); black dashed line is the cosmological mean model (Model 9); green dotted line is the model by Naab & Ostriker (2006) (Model 10). Upper right panel: magenta solid line is the constant infall model (Model 2); blue dashed line is the linear infall model (Model 3); cyan dotted line is the pre-enriched model ($Z_{inf} = 1/10\ Z_{today}$, Model 4). Bottom left panel: black solid line is Model 5; magenta dashed line is Model 6. Bottom right panel: blue solid line is Model 7; cyan dashed line is Model 8.

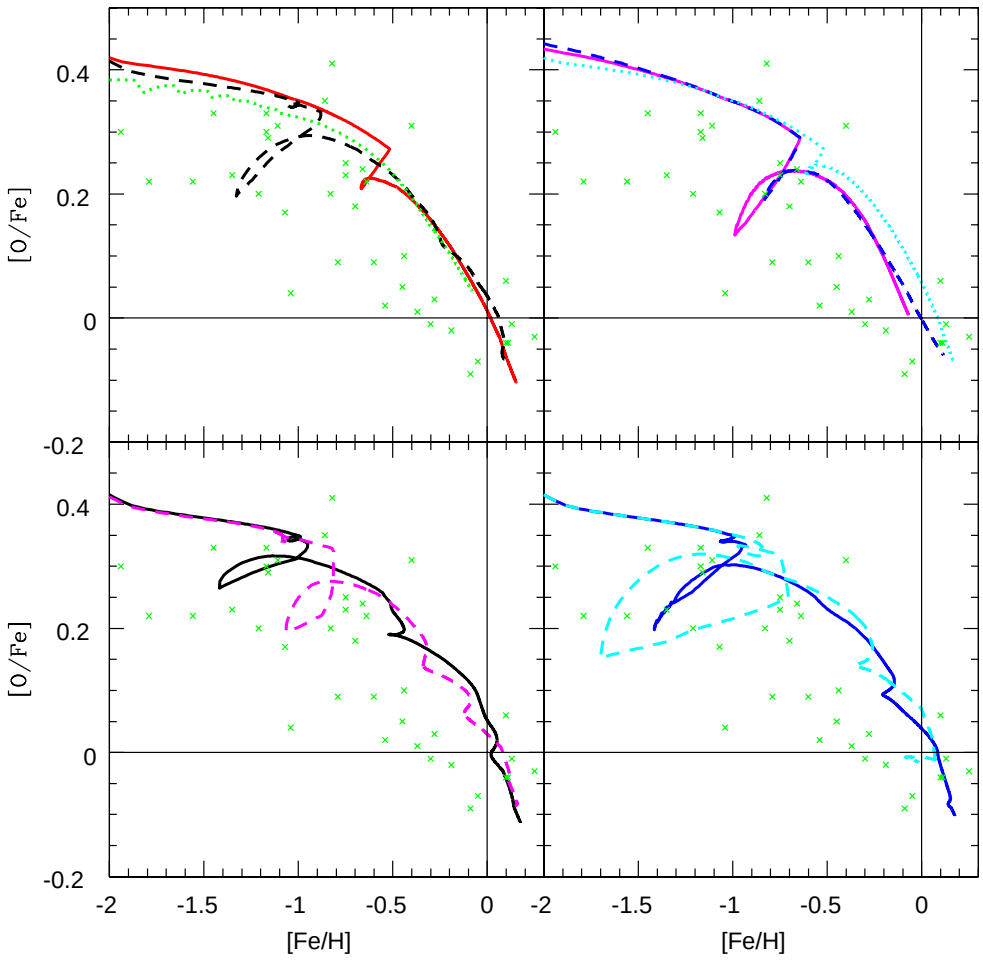

Figure 4.8: $[O/Fe]$ vs $[Fe/H]$. Upper left panel: red solid line is the two-infall model (Model 1); black dashed line is the cosmological mean model (Model 9); green dotted line is the model by Naab & Ostriker (2006) (Model 10). Upper right panel: magenta solid line is the constant infall model (Model 2); blue dashed line is the linear infall model (Model 3); cyan dotted line is the pre-enriched model ($Z_{inf} = 1/10\ Z_{today}$, Model 4). Bottom left panel: black solid line is Model 5; magenta dashed line is Model 6. Bottom right panel: blue solid line is Model 7; cyan dashed line is Model 8. The data are from François et al. (2004) (green crosses).

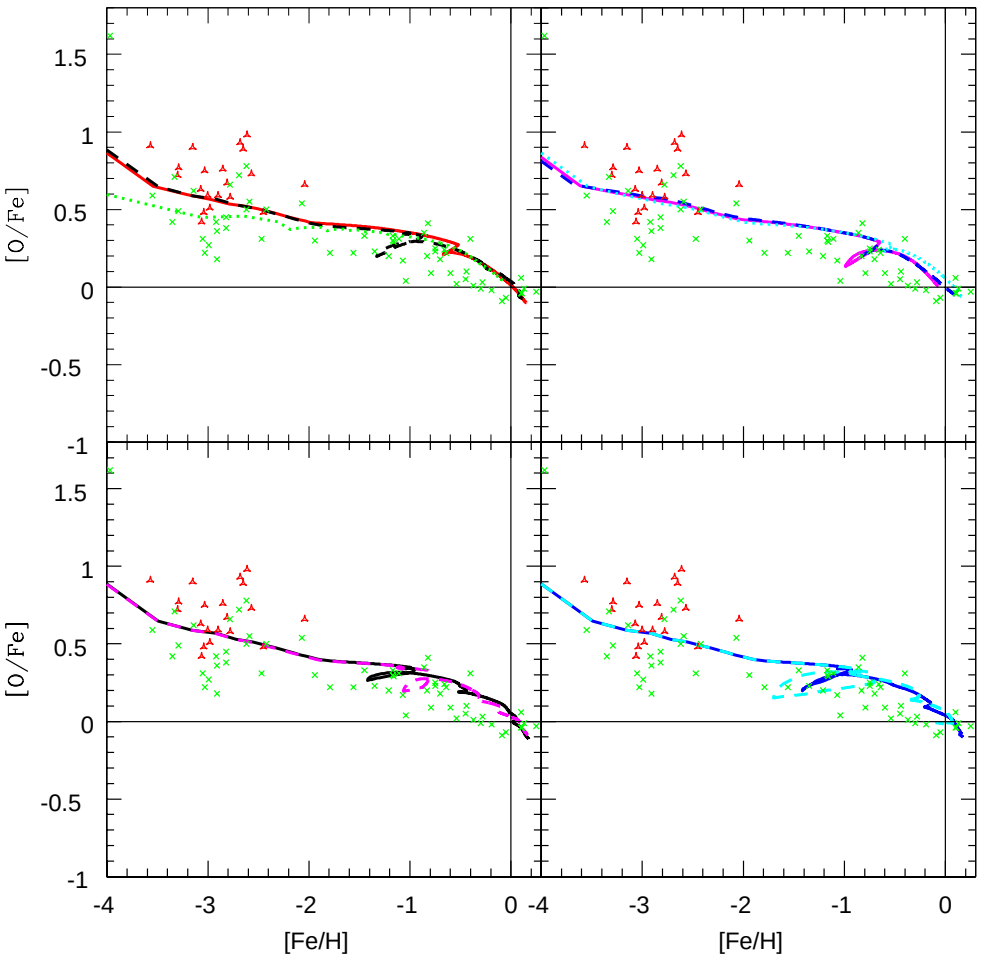

Figure 4.9: $[O/Fe]$ vs $[Fe/H]$. Upper left panel: red solid line is the two-infall model (Model 1); black dashed line is the cosmological mean model (Model 9); green dotted line is the model by Naab & Ostriker (2006) (Model 10). Upper right panel: magenta solid line is the constant infall model (Model 2); blue dashed line is the linear infall model (Model 3); cyan dotted line is the pre-enriched model ($Z_{inf} = 1/10\ Z_{today}$, Model 4). Bottom left panel: black solid line is Model 5; magenta dashed line is Model 6. Bottom right panel: blue solid line is Model 7; cyan dashed line is Model 8. The data are from: Cayrel et al. (2004) (red triangles) and François et al. (2004) (green crosses).

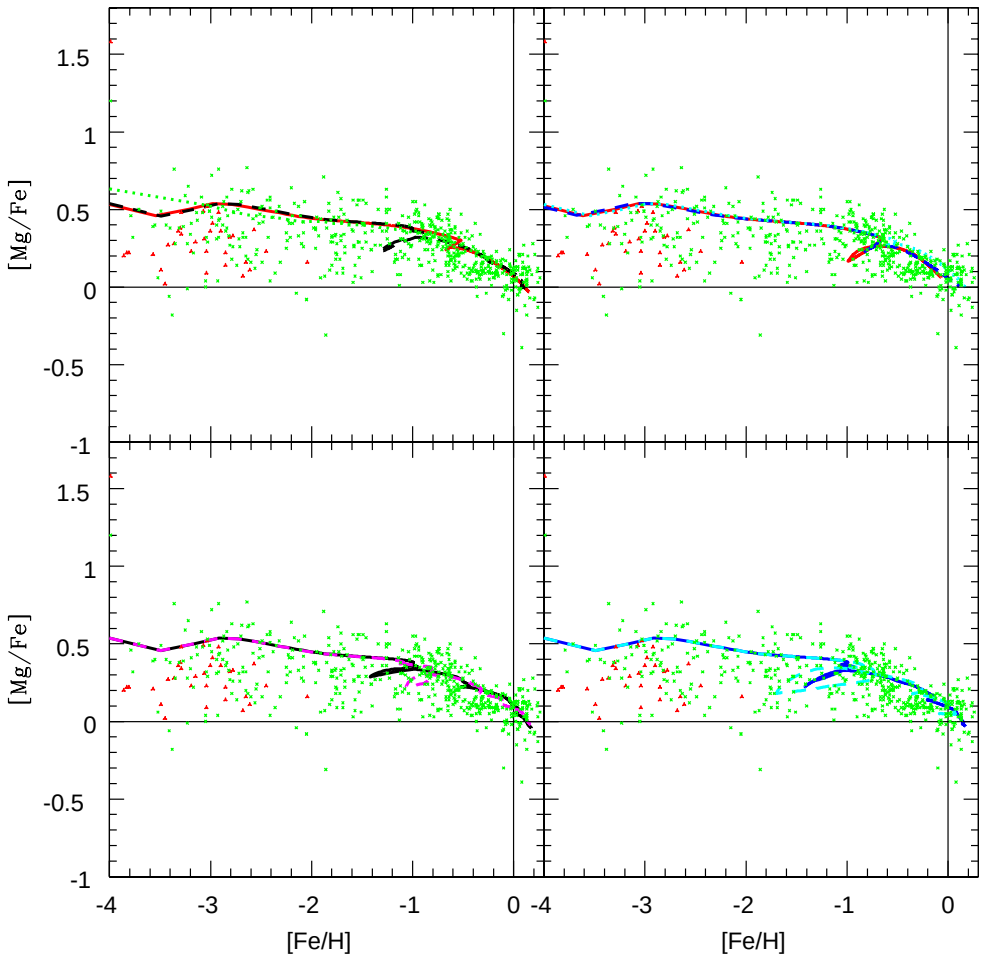

Figure 4.10: $[Mg/Fe]$ vs $[Fe/H]$. Upper left panel: red solid line is the two-infall model (Model 1); black dashed line is the cosmological mean model (Model 9); green dotted line is the model by Naab & Ostriker (2006) (Model 10). Upper right panel: magenta solid line is the constant infall model (Model 2); blue dashed line is the linear infall model (Model 3); cyan dotted line is the pre-enriched model ($Z_{inf} = 1/10\ Z_{today}$, Model 4). Bottom left panel: black solid line is Model 5; magenta dashed line is Model 6. Bottom right panel: blue solid line is Model 7; cyan dashed line is Model 8. The data are from: Cayrel et al. (2004) (red triangles) and François et al. (2004).

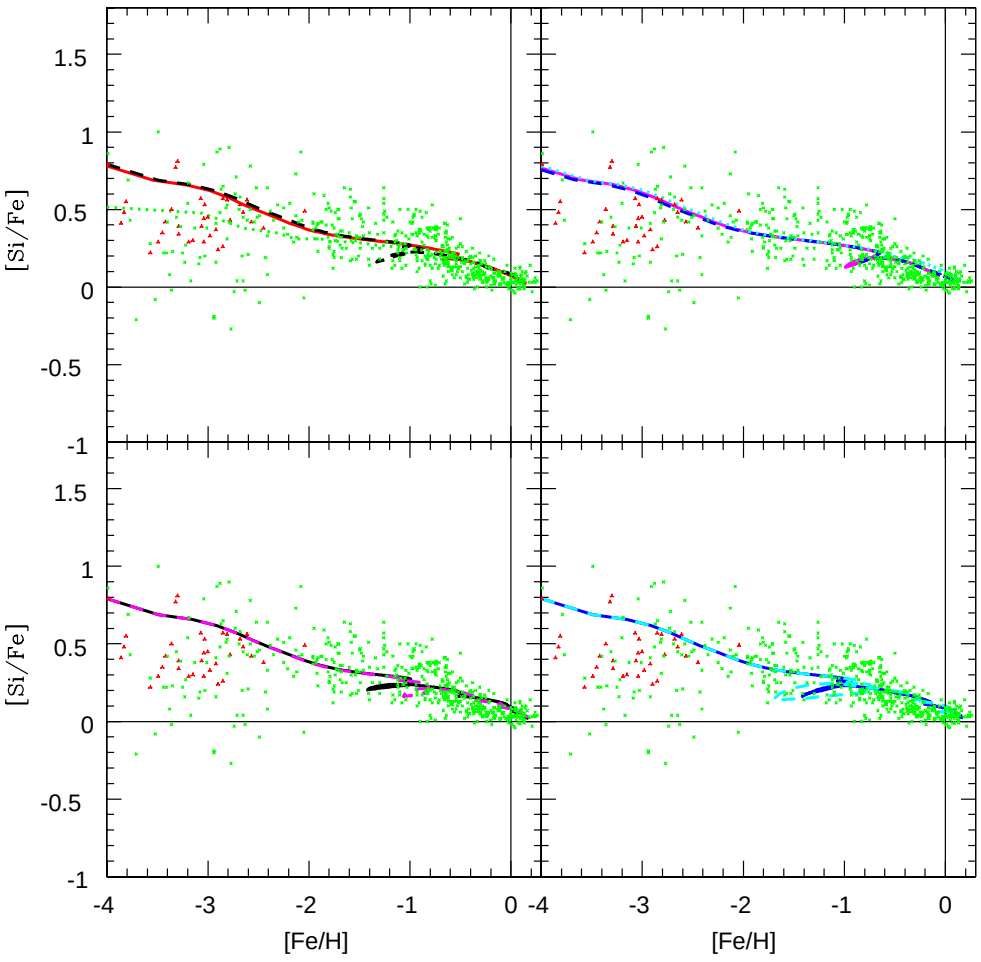

Figure 4.11: $[Si/Fe]$ vs $[Fe/H]$. Upper left panel: red solid line is the two-infall model (Model 1); black dashed line is the cosmological mean model (Model 9); green dotted line is the model by Naab & Ostriker (2006) (Model 10). Upper right panel: magenta solid line is the constant infall model (Model 2); blue dashed line is the linear infall model (Model 3); cyan dotted line is the pre-enriched model ($Z_{inf} = 1/10\ Z_{today}$, Model 4). Bottom left panel: black solid line is Model 5; magenta dashed line is Model 6. Bottom right panel: blue solid line is Model 7; cyan dashed line is Model 8. The data are from: Cayrel et al. (2004) (red triangles) and François et al. (2004).

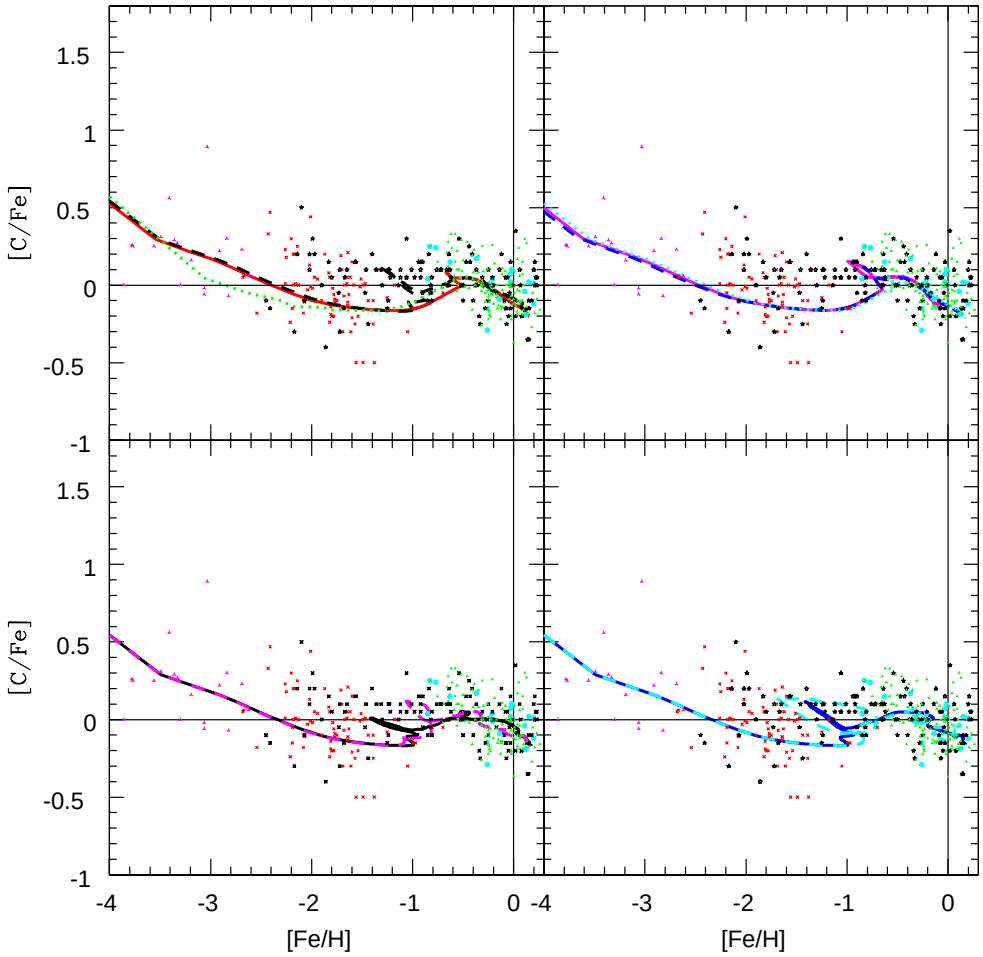

Figure 4.12: $[C/Fe]$ vs $[Fe/H]$. Upper left panel: red solid line is the two-infall model (Model 1); black dashed line is the cosmological mean model (Model 9); green dotted line is the model by Naab & Ostriker (2006) (Model 10). Upper right panel: magenta solid line is the constant infall model (Model 2); blue dashed line is the linear infall model (Model 3); cyan dotted line is the pre-enriched model (Z_{inf} = 1/10 Z_{today}, Model 4). Bottom left panel: black solid line is Model 5; magenta dashed line is Model 6. Bottom right panel: blue solid line is Model 7; cyan dashed line is Model 8. The data are from: Spite et al. (2005) (magenta stars with three arms), Carbon et al. (1987) (red crosses), Clegg, Lambert & Tomkin (1981) (cyan circles), Laird (1985) (black stars with five arms) and Tomkin et al. (1995) (green triangles).

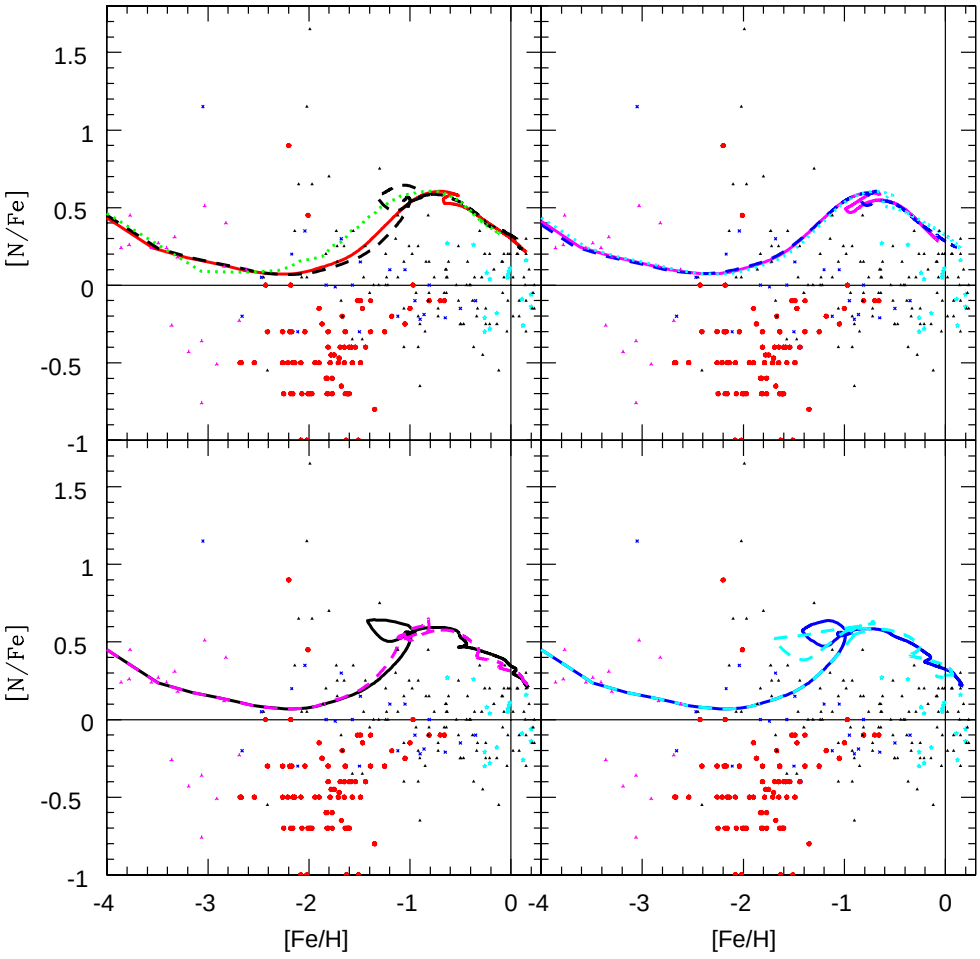

Figure 4.13: $[N/Fe]$ vs $[Fe/H]$. Upper left panel: red solid line is the two-infall model (Model 1); black dashed line is the cosmological mean model (Model 9); green dotted line is the model by Naab & Ostriker (2006) (Model 10). Upper right panel: magenta solid line is the constant infall model (Model 2); blue dashed line is the linear infall model (Model 3); cyan dotted line is the pre-enriched model ($Z_{inf} = 1/10\ Z_{today}$, Model 4). Bottom left panel: black solid line is Model 5; magenta dashed line is Model 6. Bottom right panel: blue solid line is Model 7; cyan dashed line is Model 8. The data are from: Spite et al. (2005) (magenta stars with three arms), Israelian et al. (2004) (blue crosses), Carbon et al. (1987) (red circles), Clegg, Lambert & Tomkin (1981) (cyan stars with five arms) and Laird (1985) (black triangles).

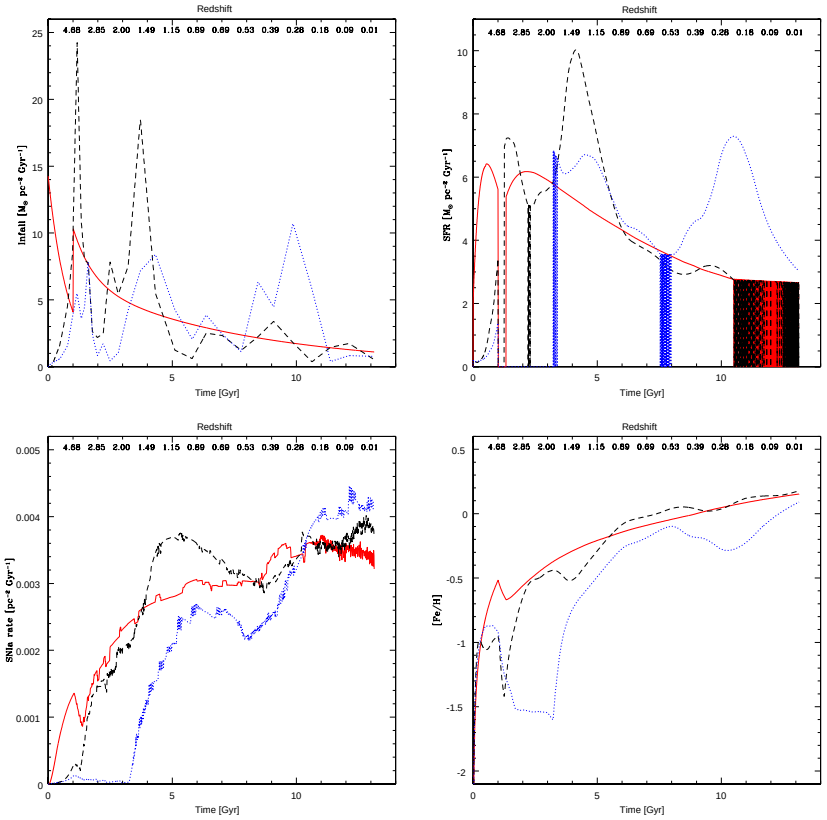

Figure 4.14: The infall law (upper left panel), the star formation rate (upper right panel), the SNIa rate (bottom left panel) and the $[Fe/H]$ (bottom right panel) as a function of time for the two-infall model (Model 1, red solid line), for Model 5 (black dashed line) and for the halo 20912 (blue dotted line).

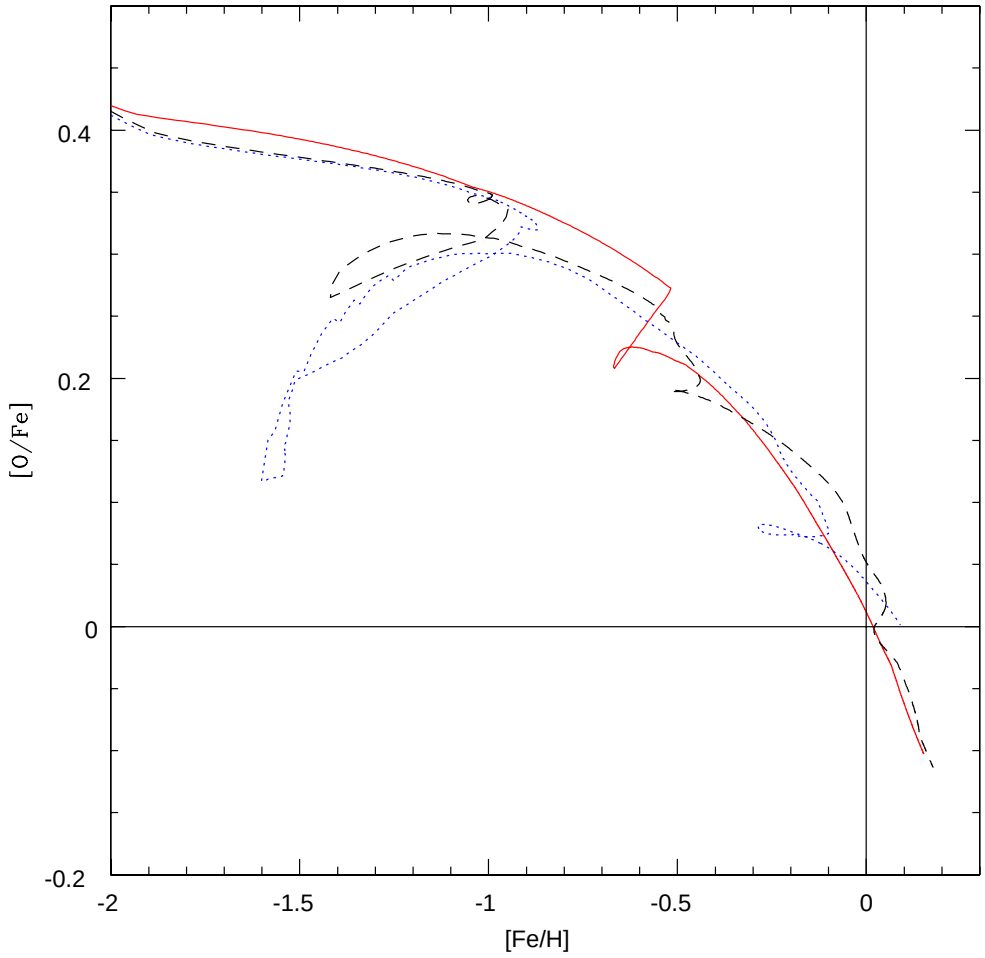

Figure 4.15: This plot represents the $[O/Fe]$ as a function of $[Fe/H]$. The red solid line represents the two-infall model (Model 1), the black dashed line represents Model 5 and the blue dashed line the halo 20912.

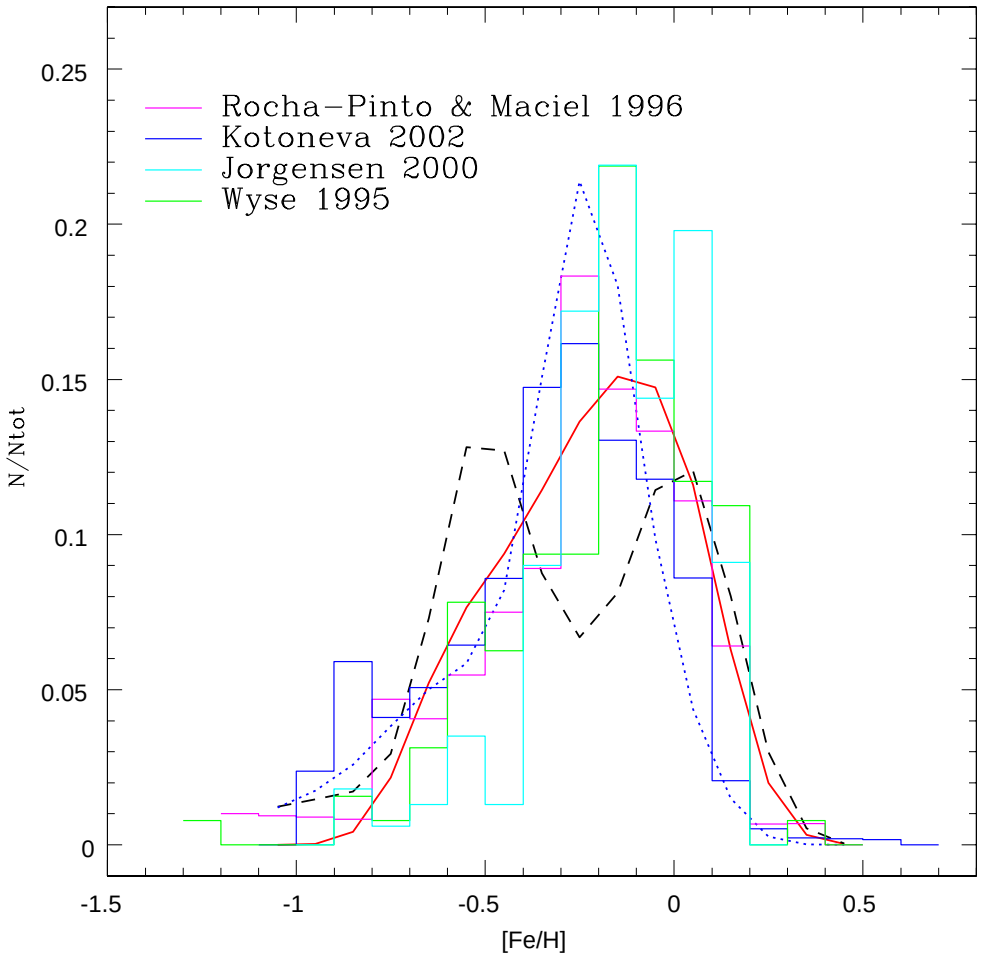

Figure 4.16: G-dwarf metallicity distribution for the two-infall model (red solid line), Model 5 (black dashed line) and for the halo 20912 (blue dashed line).

Chapter 5

Formation of the Milky Way disk in a cosmological context

In the previous chapter we have concentrated on results produced for the solar neighbourhood. Now we extend our results to the whole Galactic disk, in order to understand if our best cosmological model can well reproduce all the observables.

In Fig. 5.1 we show the infall law derived for Model 5 (our best halo, see chapter 4) for three galactocentric distances (4, 8 and 14 kpc). The derived infall laws have the same functional form for the whole Milky Way, but the normalization constant (see section 4.3) is different for different Galactic regions. In this case no assumptions are used about the timescales of disk formation at any radius.

In Figure 5.2 we show the O abundance gradient as predicted by Model 1 and Model 5 (see chapter 4), compared with a compilation of data including Cepheids (see Cescutti et al. 2007). As one can see, the O gradient predicted by Model 5 flattens for $r < 8$ kpc whereas it agrees very well with the slope predicted by Model 1 (the original two-infall model) for $r \geq 8$ kpc. Model 1 contains the assumption of an inside-out formation of the disk, as described by eq. (4.3), whereas in Model 5 no such assumption is made. In spite of that, the two predicted gradients are similar and we cannot reject the O gradient predicted by Model 5 on the basis of the comparison with data. The reason for that probably resides in the adoption of the star formation

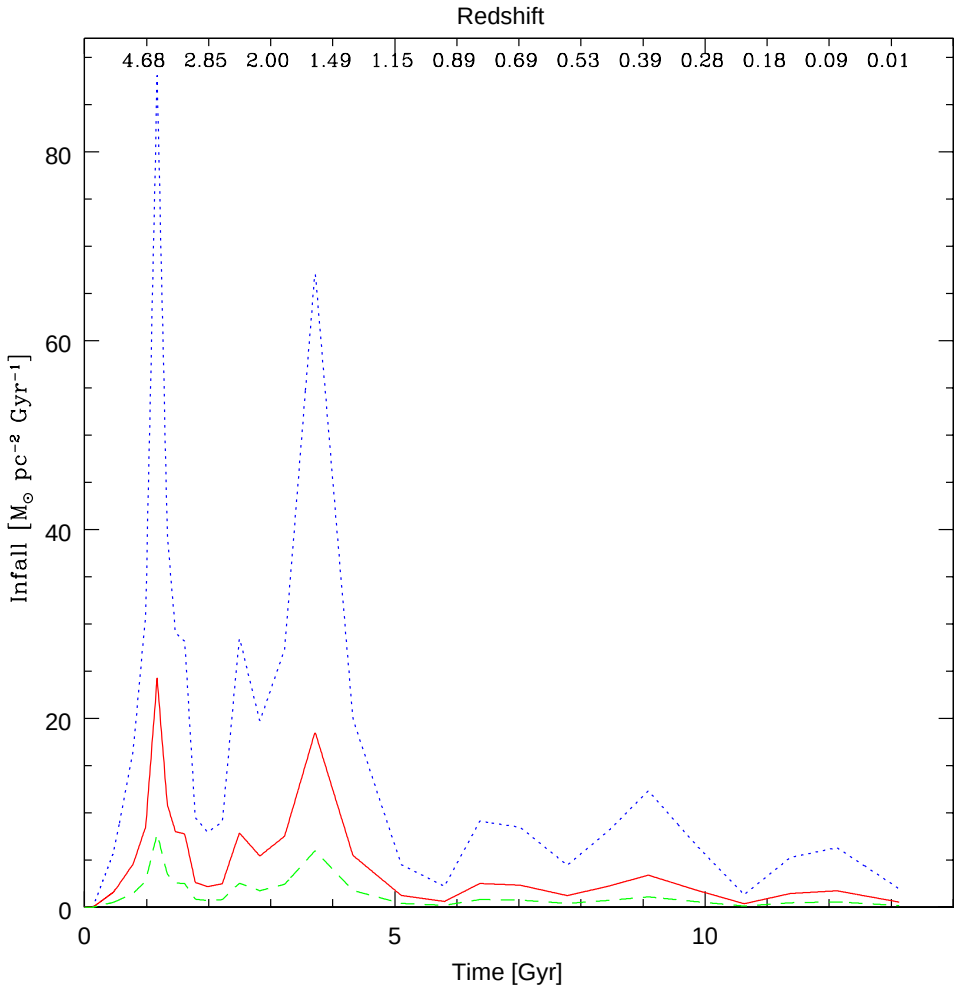

Figure 5.1: The infall law of our best cosmological halo, i.e. halo 48001, at three different radii (4 kpc: blue dotted line; 8 kpc: red solid line; 14 kpc: green dashed line).

threshold which acts mainly at large galactocentric distances where the gas density is lower. This effect predominates over the increase of the timescale for disk formation.

In this chapter we study the abundance gradients along the Galactic disk and their dependence upon four variables in order to understand if it is possible to well reproduce all the observed values. The considered variable

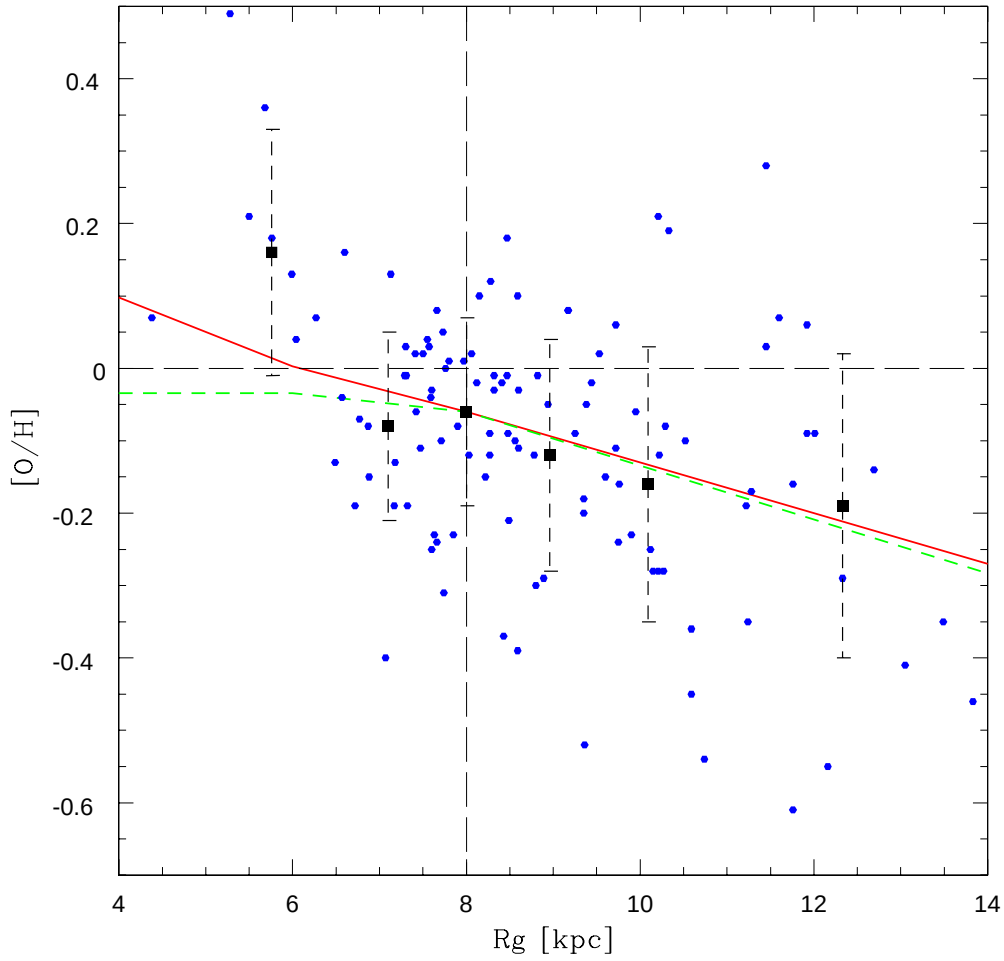

Figure 5.2: Predicted and observed *O* abundance gradients in the galactocentric distance range 4 - 14 kpc. The continuous line is the prediction of the two-infall model, the dashed line is the prediction of Model 5. The data points are from Cepheids. The large squares with error bars represent averages of the points with their errors (see Cescutti et al. 2007 and reference therein).

are: a threshold in the surface gas density regulating star formation, the star formation efficiency, the timescale for the formation of the thin disk and the total surface mass density of the stellar halo. Chiappini et al. (2001) explored the effect of the same parameters on the abundance gradients.

We compare our model predictions to observational data relative to abundance gradients along the disk. Andrievsky et al. (2002a-c, 2004) and Luck et al. (2003) measured the abundances of all the selected elements (O, N and Fe) in a sample of 130 Galactic Cepheids found in the galactocentric distance range from 5 to 17 kpc. These variable stars have a distinct role in the determination of radial abundance gradients for several reasons. First, they are usually bright enough that they can be observed at large distances, providing accurate abundances; second, their distances are generally well determined, as these objects are often used as distance calibrators; third, their ages are also well determined. They generally have ages close to a few hundred million years. So we can assume that they are representative of the present day gradients.

We also compare our results with the observational data collected by Simpson et al. (1995), Afflerbach et al. (1997) and Gummersbach et al. (1998) for the N gradient from HII regions and with those collected by Chen, Hou & Wang (2003), Twarog et al. (1997) and Carraro et al. (1998) for the Fe gradient from open clusters. We also compare our model results with the star formation rate and the surface gas density as functions of the galactocentric distance by adopting the data collected by Rana (1991). He took the average HI distribution from Blitz et al. (1983), Gordon & Burton (1976) and Garwood & Dickey 1989 and two distinct H_2 distributions: one from Bronfman (1986) and the other from Robinson et al. (1988), Wouterloot et al. (1990) and Digel et al. (1990). Moreover he took the radial dependences of the present surface density of the star formation rate from Rana & Wilkinson (1986).

The considered variables to test our models are:

- **Threshold.** In the original model by Chiappini et al. (1997) the threshold in the surface gas density was equal to 4 $M_{\odot}\ pc^{-2}$ during the formation of the halo and to 7 $M_{\odot}\ pc^{-2}$ during the formation of the thin disk. When the surface gas density was lower than these values the SFR stopped. Here we switch off the threshold in all the models.

- **SF efficiency (ν).** In Chiappini et al. (1997) and in chapter 4 the star formation efficiency was assumed to be constant along the disk.

Here we use, for some models, a SF efficiency which is a function of radius. This approach is already known (see Boissier & Prantzos 1999) and such a dependence has been proposed on the basis of large-scale instabilities in rotating discs. Even in Carigi (1996) the author used a model in which the star formation efficiency was variable with radius ($\nu(r) \propto r^{-1}$, as already seen in Prantzos & Aubert 1995). We adopt several ad hoc variations of the parameter ν as a function of radius plus the law adopted in Boissier & Prantzos (1999). All the adopted laws are shown in Table 1.

- **Timescale for the formation of the disk (τ).** In Chiappini et al. (1997) the Galactic disk forms inside-out. This means that the inner parts of the galactic disk formed first than the outer ones. This type of formation was introduced to explain the Galactic gradients. Even in Carigi (1996) the author used a model in which the infall timescale for the disk was variable with radius. In chapter 4, instead, we do not use an inside-out scenario since the cosmologically derived infall law does not contain such process. So in this case the parameter τ cannot be changed.

  In some of the models we use a constant timescale while in others we use the prescription used in Chiappini et al. (1997), namely:

$$\tau = 1.03\, r - 1.27\ [Gyr], \tag{5.1}$$

  where r is the galactocentric radius in kpc. Other authors have also studied an inside-out formation of the disk by assuming a linear dependence of τ on r (e.g. Matteucci & François 1989, Carigi 1996, Boissier & Prantzos 1999).

- **Surface halo mass density (Σ_{halo}).** In Chiappini et al. (1997) the projected halo mass density was a constant parameter. Here we use both a halo density which is a function of radius and a constant one, as in Chiappini et al. (2001). In particular, it follows this equation:

$$\Sigma_{halo} = \frac{136}{r}\ [M_{\odot}\ pc^{-2}], \tag{5.2}$$

where r is the radius in kpc. The value of 136 is adopted in order to have a surface halo mass density equal to 17 $M_{\odot}\ pc^{-2}$ at the solar neighbourhood. The halo density is important in determining the slope of the gradient at large galactocentric distances, where the disk density is very low (see Chiappini et al. 2001).

In Table 5.1 we present the models and all the parameters which characterize them. The second column indicates the presence or the absence of a threshold, the third column the type of variation of the SF efficiency (the values of ν for Model 3 are for 2.5, 7.5 and 12.5 kpc), the fourth shows if the galaxy forms inside-out or not and the fifth if the halo density is constant or if it is a function of radius. In the sixth column we show the type of infall law used and in the seventh column the SFR.

Table 5.1: Models parameters. The second column indicates the presence or the absence of a threshold, the third column the type of SF efficiency, the fourth if the galaxy forms inside-out and the fifth if the halo density is constant or if it is a function of radius. In the sixth column we show the type of infall law used and in the seventh column the SFR. The values of ν for Model 3 are for 2.5, 7.5 and 12.5 kpc.

Model	Threshold	ν (4 - 6 - 8 - 10 - 12 - 14 kpc)	τ	Σ_{halo}	Infall law	SFR
C08	yes	const	/	/	cosmological	eq. (1)
C97	yes	const	1.03 · R - 1.27	const	two-infall law	eq. (1)
1	no	const	/	/	cosmological	eq. (1)
2	no	8.0 - 4.0 - 1.0 - 0.5 - 0.2 - 0.05	/	/	cosmological	eq. (1)
3	no	4.0 - 1.0 - 0.1	/	/	cosmological with inside-out	eq. (1)
4	no	const	const	const	two-infall law	eq. (1)
5	no	const	1.03 · R - 1.27	const	two-infall law	eq. (1)
6	no	9.0 - 3.0 - 1.0 - 0.3 - 0.1 - 0.03	1.03 · R - 1.27	$\propto$ 1/R	two-infall law	eq. (1)
7	no	$0.1 \cdot 8/R$	const	/	one-infall law	eq. (2)

Model C08 is our best cosmological model (see chapter 4, Model 5). It has the threshold only during the formation of the disk and a constant star formation efficiency ν.

Model C97 is the original model of Chiappini et al. (1997). It has a threshold, both during the formation of the halo and thick-disk component and during the formation of the thin disk. It has a star formation efficiency constant along radius and equal to $\nu = 1.0\ Gyr^{-1}$, an inside-out prescription and a constant surface halo density along radius.

5.1 Models C08, C97, 1 and 2

In Figures 5.3 and 5.4 the results for Model C97, compared with those predicted by Model C08 and with observations, can be seen. Figure 5.3, upper panel, presents the SFR normalized at the solar neighbourhood value. The data are from Rana (1991) (green dotted line) while the red dashed line represents Model C08. The black solid line represents Model C97. It can be seen that both Model C97 and Model C08 have no SF in the outer part of the disk, both having a threshold in the surface gas density below which the SF stops. The bottom panel of Figure 5.3 shows the current surface gas density along the radius. The data are, once again, from Rana (1991). In this case Model C97 and Model C08 produce very similar results. Moreover both the models reproduce very well the lower values of Rana (1991).

Figure 5.4 shows the evolution of $[O/H]$, $[N/H]$ and $[Fe/H]$ along the radius for Models C97 and C08. The model results are normalized to the Asplund et al. (2005) solar abundances in all the models. The data are from a compilation by Cescutti et al. (2007) (blue dots, Cepheids stars), from Gummersbach et al. (1998) (red squares, B stars), from Simpson et al. (1995) and Afflerbach et al. (1997) (green triangles, HII regions) and from Chen, Hou & Wang (2003), Carraro et al. (1998) and Twarog et al. (1997) (cyan crosses, open clusters). The black squares are the mean values inside each bin only for the compilation by Cescutti et al. (2007) and the error bars are the standard deviations. It can be seen that Model C97 reproduces quite well the data, even in the inner part of the disk, since the slope is more pronounced than that of Model C08. As already said, Model C08 is too flat in the inner part of the disk. For this reason we test several parameters in order to better reproduce the inner abundance gradients. In the outer parts of the galactic disk the slope of Model C08 is more pronunced than that of Model C97.

Figures 5.5 and 5.6 show the results for Model 1, compared with those predicted by Model C08 and with observations. Model 1 is equal to Model C08, except for the lack of the threshold. We can see that Model 1 reproduces very well the $SFR/SFR_{\odot}$, much better than Model C08. However, Model 1 can not reproduce the surface gas density in the outer parts of the disk,

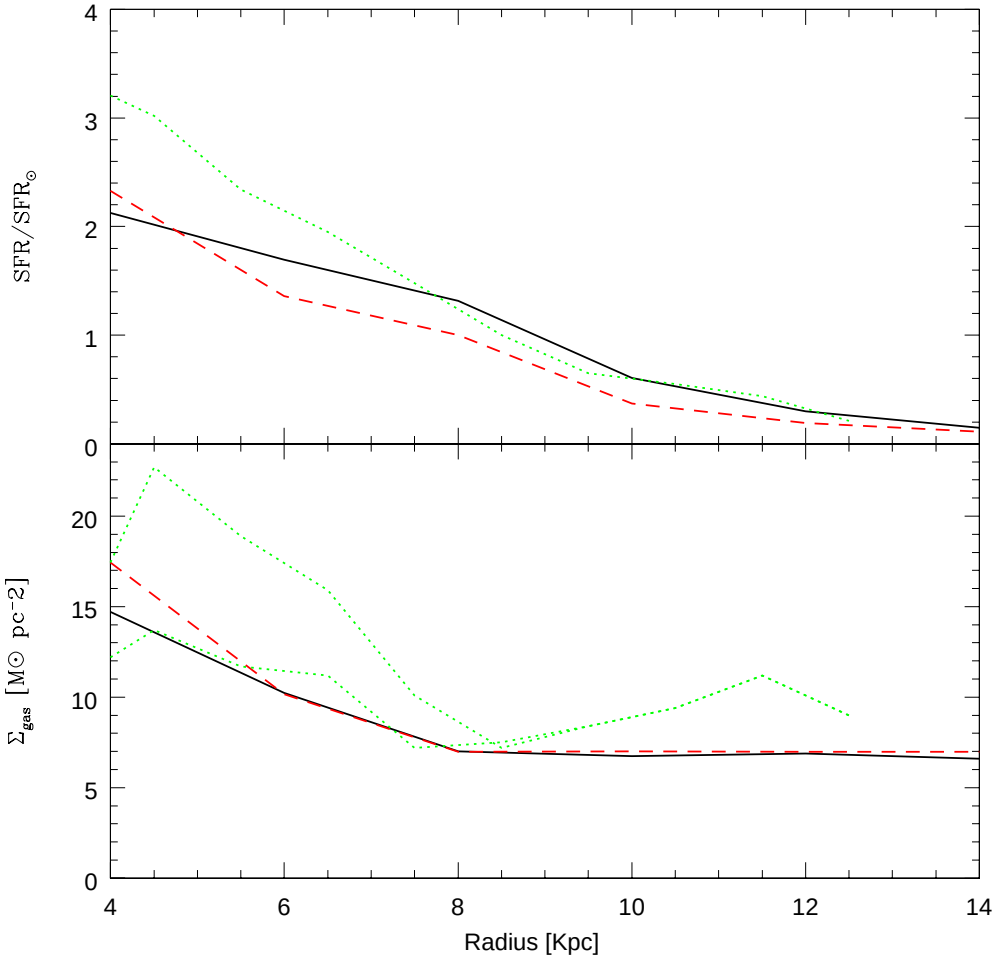

Figure 5.3: $SFR/SFR_{\odot}$ and surface gas density vs radius for Model C97 (black solid line) and for Model C08 (red dashed line). The data are from Rana (1991) (green dotted lines, representing the lower and the maximum values for the gas).

since the obtained values are too low respect to the observed values.

Figure 5.6 shows the abundance gradients for Model 1, compared with the results of Model C08. The data are the same of Figure 5.4. In this case the lack of a threshold in the surface gas density makes the abundances gradients completely flat. Therefore, simply removing the threshold from

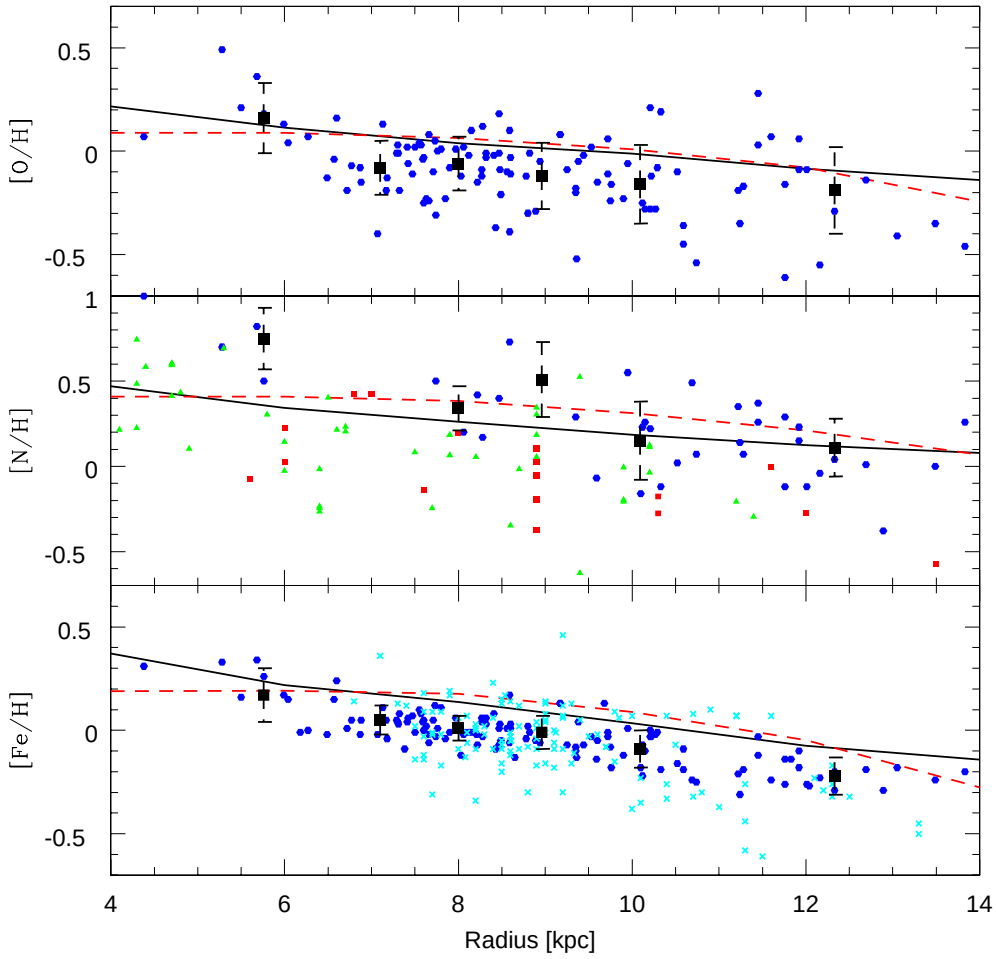

Figure 5.4: $[O/H]$, $[N/H]$ and $[Fe/H]$ vs radius for Model C97 (black solid line) and for Model C08 (red dashed line). The data are from a compilation by Cescutti et al. (2007) (blue dots, Cepheids), from Gummersbach et al. (1998) (red squares, B stars), from Simpson et al. (1995) and Afflerbach et al. (1997) (green triangles, HII regions) and from Chen, Hou & Wang (2003), Carraro et al. (1998) and Twarog et al. (1997) (cyan crosses, open clusters). The black squares are the mean values inside each bin only for the compilation by Cescutti et al. (2007) and the error bars are the standard deviations.

Model C08, it is not possible to reproduce the chemical abundances along the galactic disk, neither in the inner parts nor in the outers. So in the next

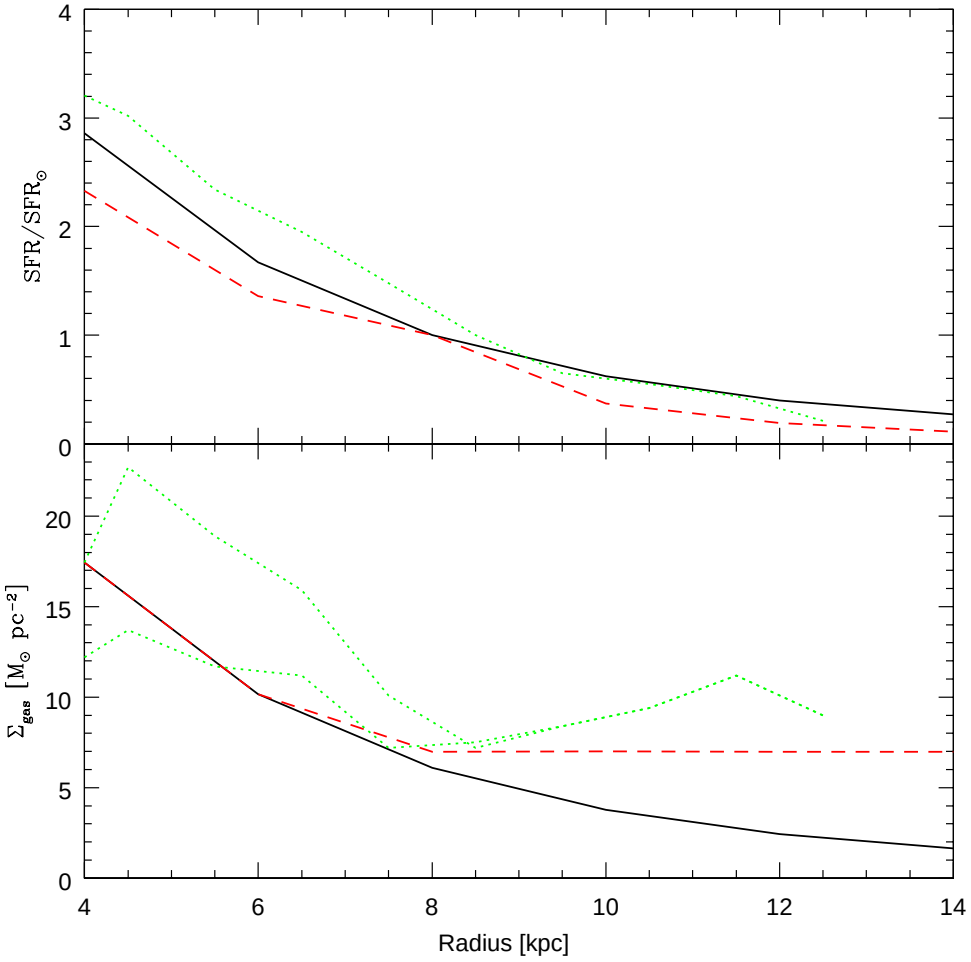

Figure 5.5: $SFR/SFR_\odot$ and surface gas density vs radius for Model 1 (black solid line) and for Model C08 (red dashed line). The data are the same of Figure 5.3.

model (Model 2) we also use a variable star formation efficiency along radius.

In Figures 5.7 and 5.8 the results obtained for Model 2, compared with those predicted by Model C08 and with observations, can be seen. Model 2 has the same infall law of Model C08 but in this case there is no threshold during the formation of the galactic disk. Moreover, in Model 2 we use a star formation efficiency which is a function of radius.

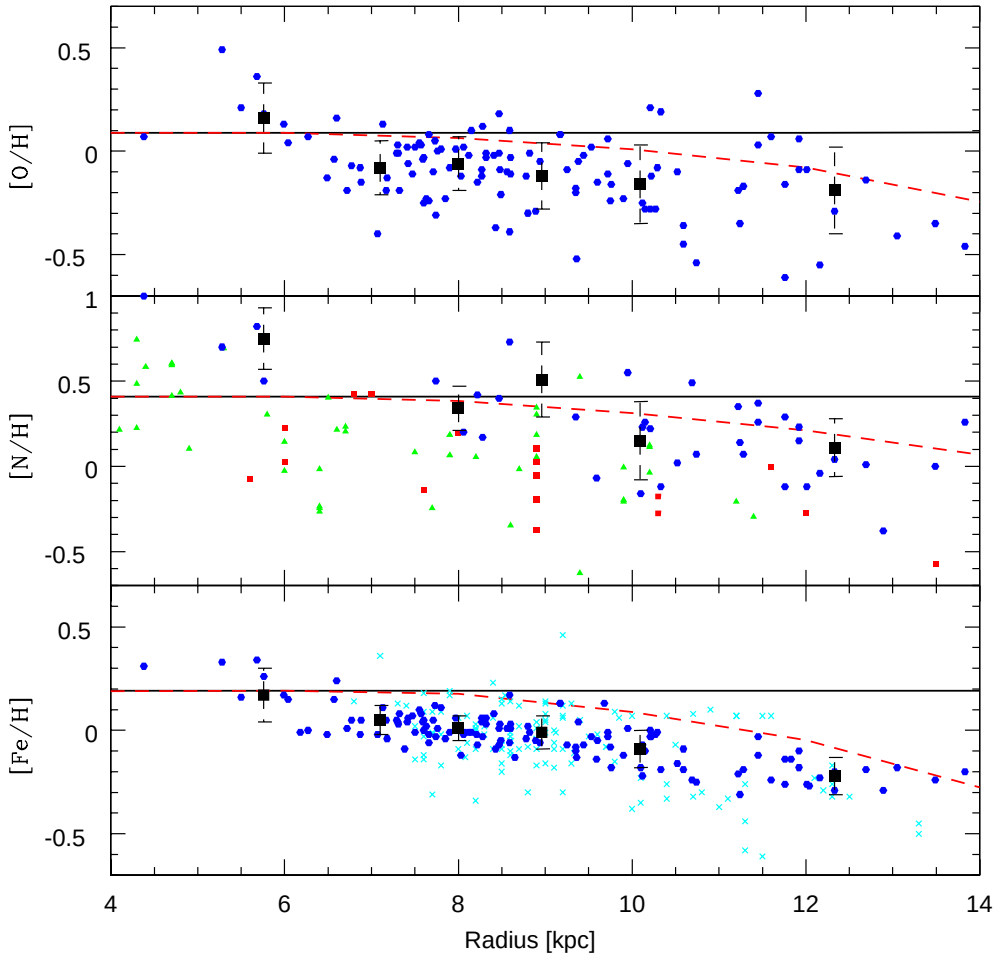

Figure 5.6: $[O/H]$, $[N/H]$ and $[Fe/H]$ vs radius for Model 1 (black solid line) and for Model C08 (red dashed line). The data are the same of Figure 5.4.

In Figure 5.7, upper panel, it can be seen that Model 2 is in better agreement with the data then Model C08, especially in the outer part of the disk. Model C08 has a $SFR/SFR_{\odot}$ equal to zero in the outer parts of the disk, and it is due to the presence of the threshold. From the bottom panel of Figure 5.7 we can see that Model C08 is in quite good agreement with the data, whereas Model 2 predicts a surface gas density at variance with the

observations: it predicts a too low SF in the inner disk because of the high SF efficiency.

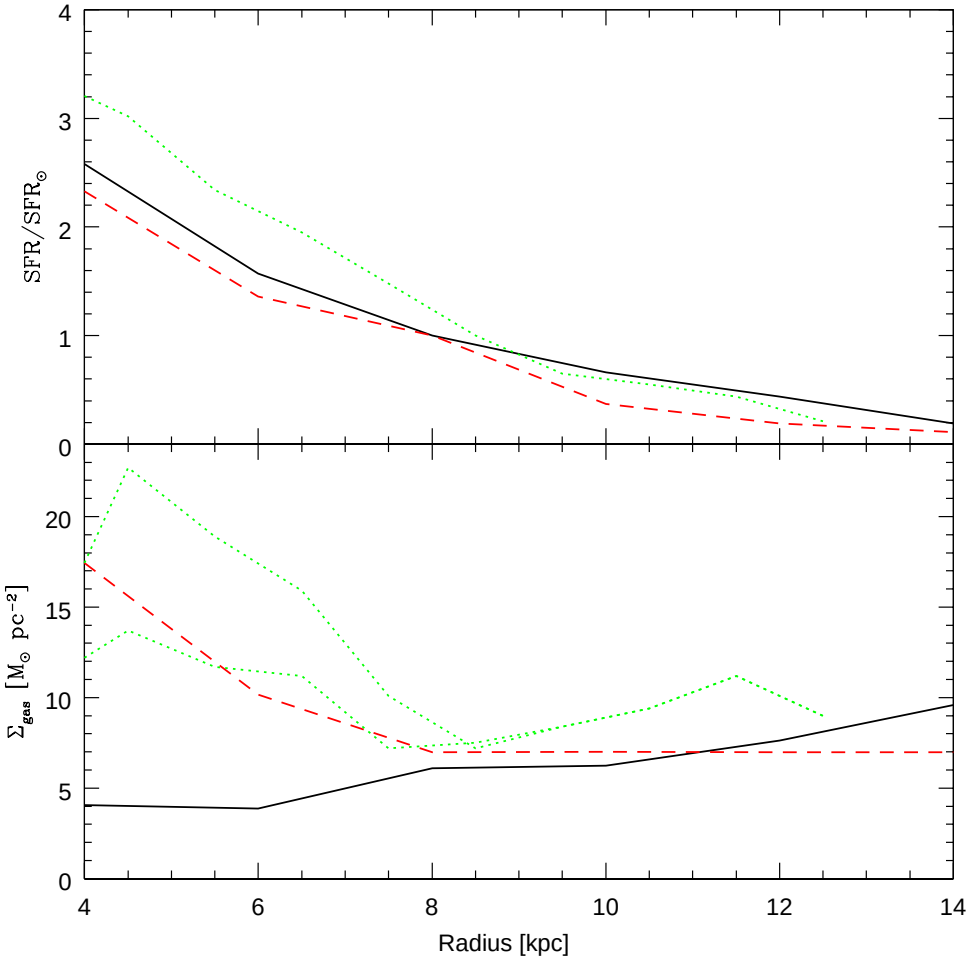

Figure 5.7: $SFR/SFR_\odot$ and surface gas density vs radius for Model 2 (black solid line) and for Model C08 (red dashed line). The data are the same of Figure 5.3.

Figure 5.8 shows the evolution of $[O/H]$, $[N/H]$ and $[Fe/H]$ along the radius for Models 2 and C08. Using no threshold and a star formation efficiency variable with radius again we cannot reproduce, as we hoped, the gradients in the inner parts of the disk. We can only increase the slope of the

gradients, relative to Model C08 in the outer parts. However it is still not sure from the observational point of view if the gradients are flatter towards the inner parts or not.

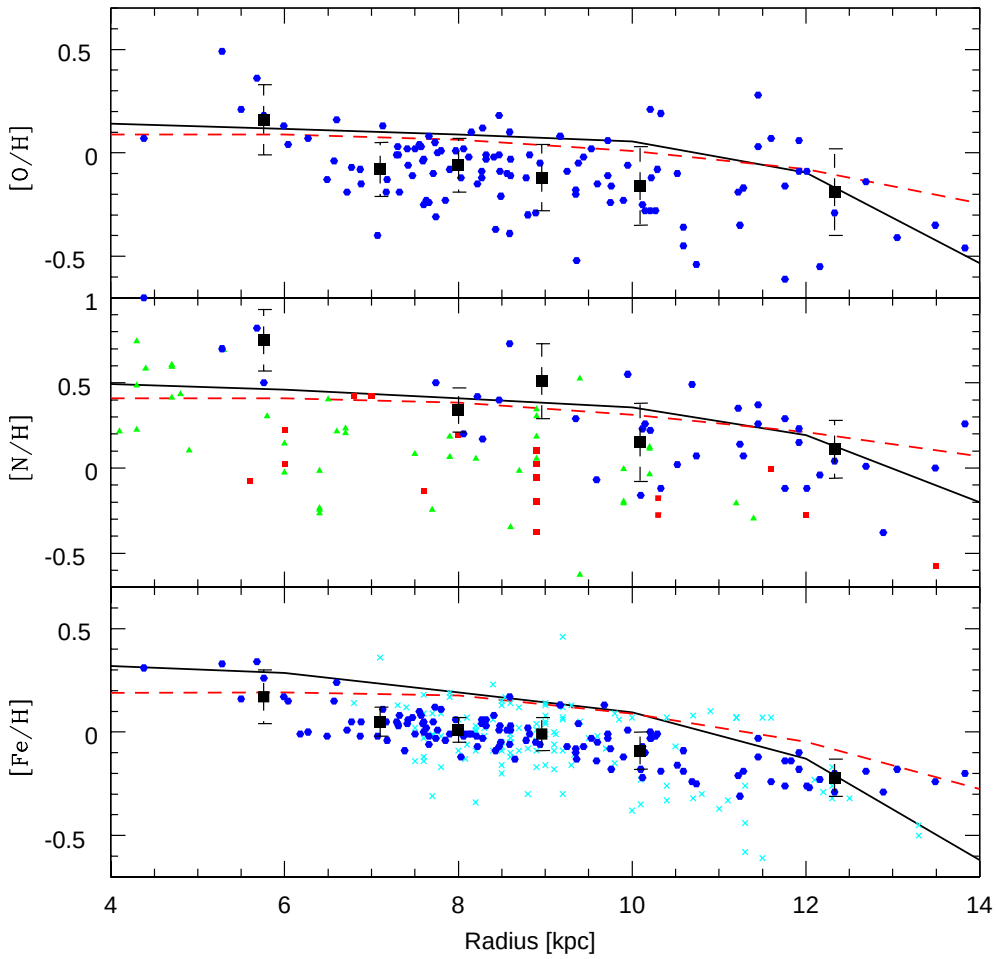

Figure 5.8: $[O/H]$, $[N/H]$ and $[Fe/H]$ vs radius for Model 2 (black solid line) and for Model C08 (red dashed line). The data are the same of Figure 5.4.

Since it is not possible to well reproduce at the same time the surface gas density and the abundance gradients along the galactic disk using the cosmologically derived infall law by C08 without the threshold or without

the threshold and adopting a SF efficiency variable along radius, we now try a new approach. As we said, model C08 assumed that the derived infall laws have the same functional form for the whole Milky Way, but that the normalization constant is different for different Galactic regions.

5.2 The cosmological infall law with inside-out

We then tried to derive infall laws having different functional form along the disk. To do this we divided the galactic disk in three zones. The first includes the central 5 kpc of the disk, the second is a radial shell starting at 5 kpc and ending at 10 kpc whereas the third shell has inner and outer radii of 10 and 15 kpc. Having the coordinates of each DM particle of the main progenitor at every redshift, we calculated the total mass included in every shell, deriving three different cosmological infall laws for the three zones. It is well-known (Helmi et al. 2003 and references therein) that the build-up of a Galaxy-sized DM halo proceeds in an inside-out fashion, with the mass of the inner part of the halo being in place at high redshift, while its outer part still accretes mass up to low redshift. We wanted to determine if a cosmological, standard resolution simulation can still capture such a behaviour. This in order to verify if it is possible to use such a simulation to build a cosmological inside-out barionic accretion law, without resorting to high-resolution resimulation of single halos with DM only or with more comples physics. It is also known that re-simulation of single halos, with gas physics, a star formation prescription and some effective form of SN energy feedback can reproduce an inside-out formation of disk galaxies (Governato et al. 2007, Abadi et al. 2003a,b). Such numerical simulations are however computationally very expensive and the properties of the simulated galaxy somehow depend on the sub-grid prescription for the various astrophysical processes. Our aim is to see whether we can obtain similar results using a much simpler numerical approach.

Then we tested these laws in the chemical evolution model, using no threshold and a star formation efficiency which changes with radius. In

Figures 5.9 and 5.10 the results can be seen.

Figure 5.9 shows that Model 3 reproduces very well the observed SFR, especially between 9 and 12.5 kpc. The slope of the curve of observable data is very similar to that of Model 3. Only at 2.5 kpc the predicted SFR is slightly larger than the observed. However the improvement respect to model C08 is clear and it is mainly due to the lack of a threshold in the superficial gas density. In the bottom panel it can be seen that Model 3 has a too low Σ_{gas} respect to the observable data and model C08. However it is interesting to note that the behavior of the curve is quite similar to that of the observable data since the increasing of the superficial gas density observed by Rana (1991) in the outer part of the disk is also predicted by Model 3. Moreover the value at 2.5 kpc is equal to that given by the observable data. However at this distance the Galaxy shows a complex mix of bar, bulge and molecular ring and so we do not expect this kind of chemical evolution models to explain the behavior of the data for galactocentric distances shorter than 3-4 kpc.

Figure 5.10 shows the obtained $[O/H]$, $[N/H]$ and $[Fe/H]$ along the radius for Model 3. It can be seen that in the case of O and N the results are quite similar to those of model C08, even if the slope produced by Model 3 is more pronunced. The slope is even more evident in the case of $[Fe/H]$, especially for the outer part of the disk. However, not even Model 3 can well reproduce the slope in the inner part of the Galaxy, in spite of the fact that the accretion law contains an inside-out effect. This is due to the mild inside-out effect predicted by the infall law which can be attributed to the relatively low resolution that our cosmological simulation can achieve on a single halo, especially at high redshifts.

5.3 Changing the parameters in the C97 models

After this study on the cosmological model by C08, we considered the model by Chiappini et al. (1997), trying to find the best combination of parameters to well reproduce the $SFR/SFR_{\odot}$, the surface gas density and the

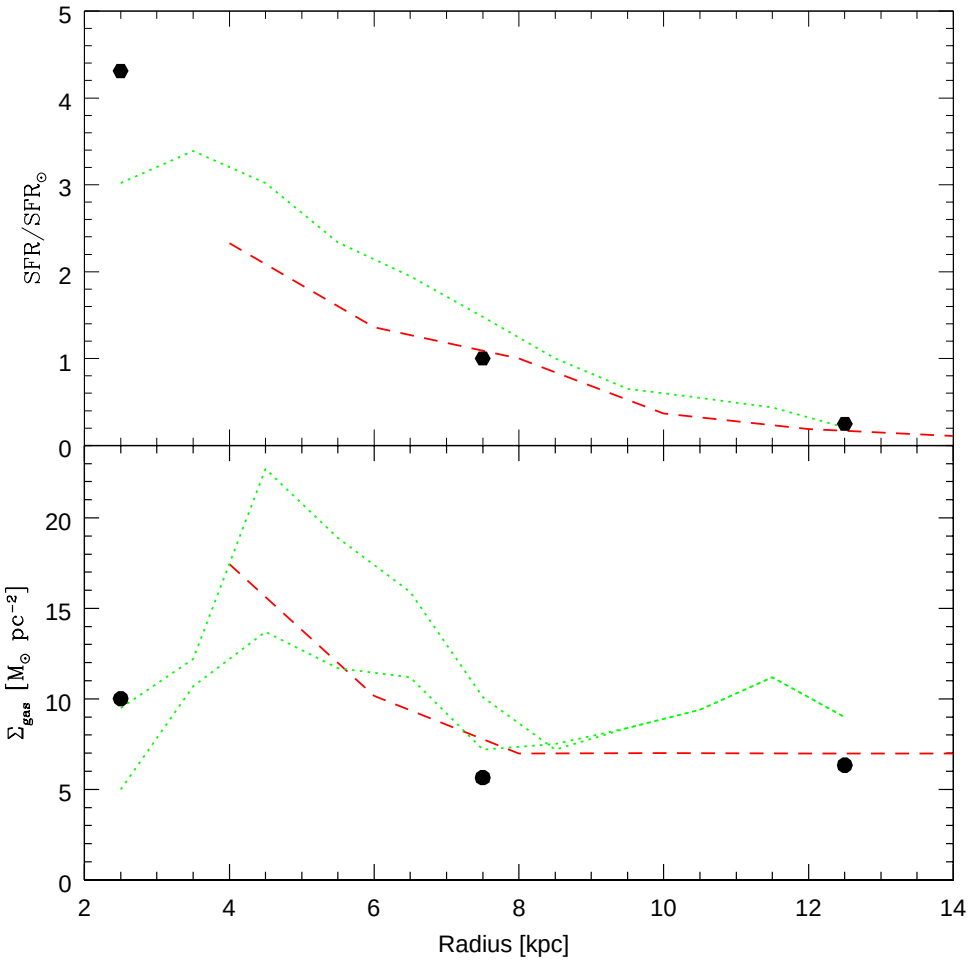

Figure 5.9: $SFR/SFR_\odot$ and surface gas density vs radius for Model 3 (black points) and for Model C08 (red dashed line). The data are the same of Figure 5.3.

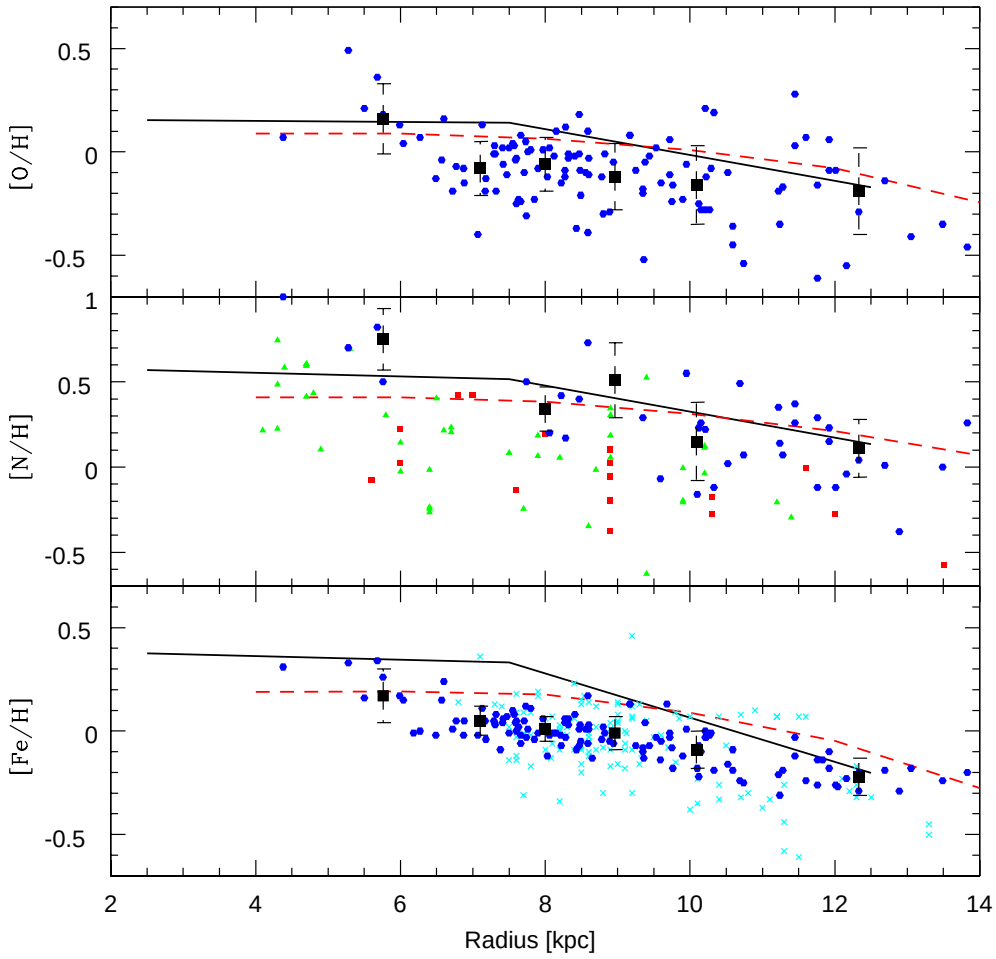

Figure 5.10: $[O/H]$, $[N/H]$ and $[Fe/H]$ vs radius for Model 3 (black solid line) and for Model C08 (red dashed line). The data are the same of Figure 5.4.

abundance gradients along the Galactic disk, as done with Model C08. The considerations done in this section are different from those presented in Chiappini et al. (2001) since we do not consider any threshold in the surface gas density. In this case we studied the behavior of the parameters in four different models, comparing every model with Model C08.

Figures 5.11 and 5.12 show the results for Model 4. This Model has no threshold and the SF efficiency ν, τ and Σ_{halo} are constants. In Figure 5.11 it can be seen that the predicted star formation rate of Model 4 agrees very well with the data by Rana (1991). However Σ_{gas} is too low in the outer parts of the disk, even if in the inner parts it agrees quite well with the observed values.

Figure 5.12 shows the $[O/H]$, $[N/H]$ and $[Fe/H]$ along radius for Model 4. We can see that in the inner disk the abundance gradients are flat, while in the outer parts they even increase, in contrast with the observed data. Therefore, it is not possible to reproduce the abundance gradients without the threshold and when ν, τ and Σ_{halo} are constants. This is due to the fact that with a constant τ the disk evolution is too quick to allow the formation of abundance gradients, and that the star formation never stops (absence of the threshold) and the halo surface mass density is constant with galactocentric distance. In this case, in fact, the star formation in the halo overcomes that in the outer disk and produces higher abundances than in the more realistic case of a fading surface halo mass density.

Figures 5.13 and 5.14 show Model 5, compared to Model C08. Model 5 has no threshold (neither in the halo nor in the disk), a constant star formation efficiency, a variable τ along the disk and a constant surface halo density. From Figure 5.13 it can be seen that the star formation rate predicted by Model 5 is in quite good agreement with the data by Rana (1991), especially for the outer parts of the galaxy. However the amount of gas is too low, even if compared with the lower values by Rana (1991).

Figure 5.14 shows the abundance gradients along the galactic disk for Model 5. In the inner part of the disk the $[O/H]$, $[N/H]$ and $[Fe/H]$ ratios are not flat as in Model C08, reproducing better the observed data. Nevertheless, beyond 10 kpc the gradients become positive at variance with the observations. So we can say that a model without threshold and with a

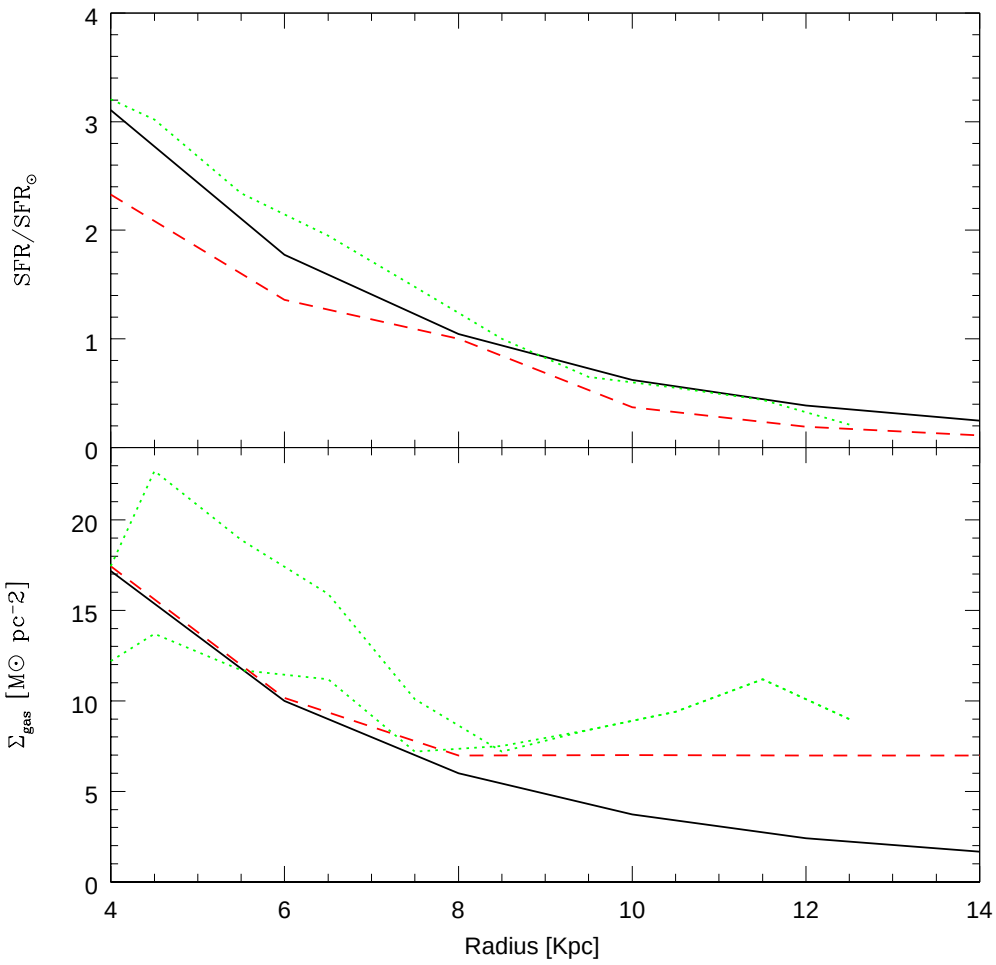

Figure 5.11: $SFR/SFR_{\odot}$ and surface gas density vs radius for Model 4 (black solid line) and for Model C08 (red dashed line). The data are the same of Figure 5.3.

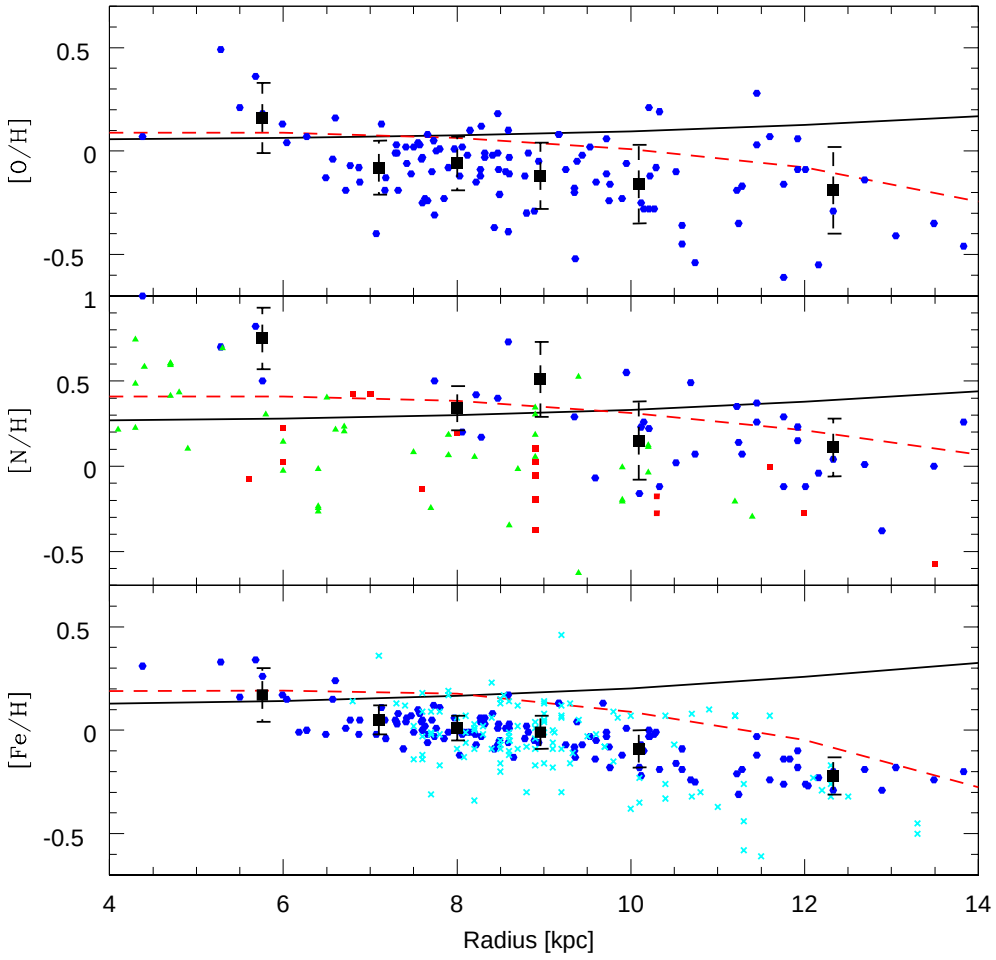

Figure 5.12: $[O/H]$, $[N/H]$ and $[Fe/H]$ vs radius for Model 4 (black solid line) and for Model C08 (red dashed line). The data are the same of Figure 5.4. It can be seen that in the outer part of the disk the gradients increase. In fact, being the halo surface mass density constant along the galactic disk and since there is no threshold in the surface gas density, the star formation in the halo overcomes that in the outer disk.

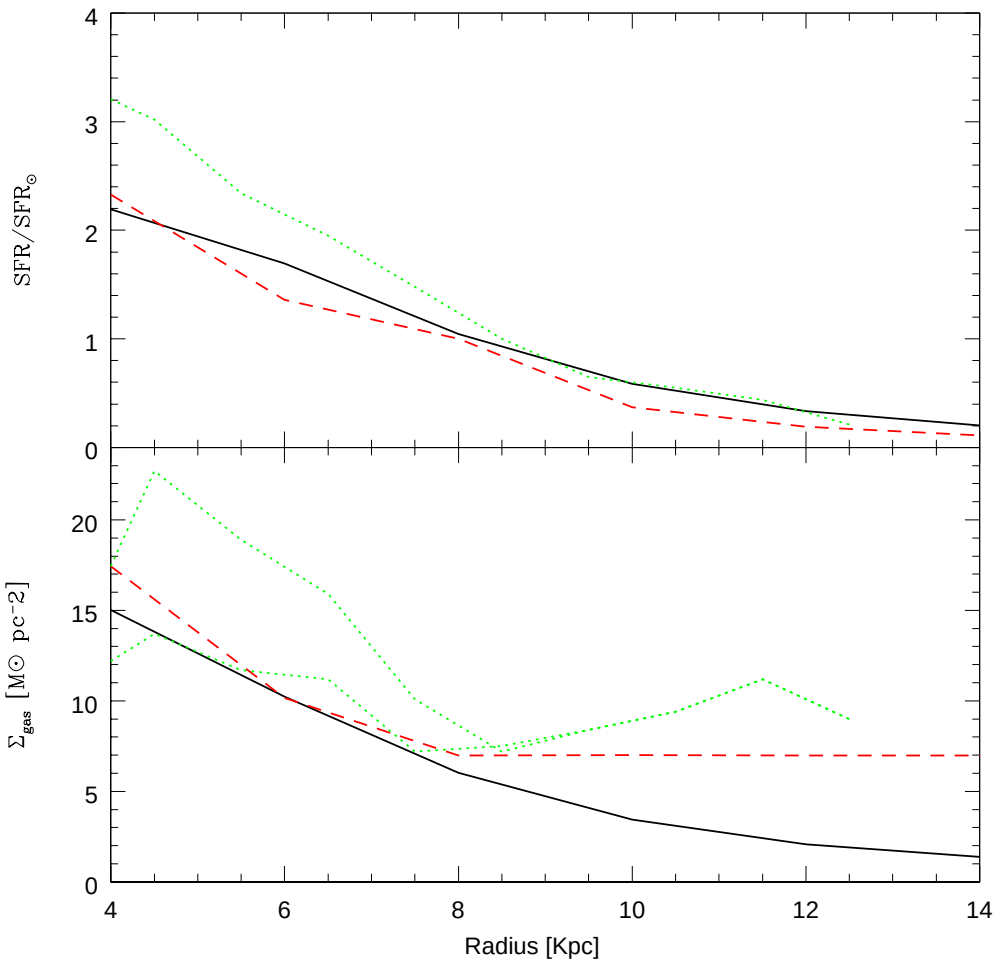

Figure 5.13: $SFR/SFR_{\odot}$ and surface gas density vs radius for Model 5 (black solid line) and for Model C08 (red dashed line). The data are the same of Figure 5.3.

variable τ cannot well reproduce the data, especially in the outer disk. This effect happens because we use a two-infall model. The models of Prantzos and collaborators, for example, without a threshold and with radially varying timescales, do reproduce the abundance gradients since they only model the disk.

Figures 5.15 and 5.16 show the $SFR/SFR_{\odot}$, Σ_{gas} and the $[O/H]$, $[N/H]$ and $[Fe/H]$ gradients for Model 6. This model has no threshold, a star formation efficiency which changes strongly with radius, an inside-out prescription and a surface halo density which is a function of radius. From Figure 5.15 it can be seen that the SFR is in good agreement with the data, especially in the outer parts of the disk. On the other hand, the surface gas density increases along radius, at variance with the observations which show that there is more gas in the inner parts of the disk.

In Figure 5.16 we can see that the abundance gradients have a slope which is quite similar to the slope of the data, mainly for the $[Fe/H]$ ratio. Even in the inner parts the gradients are in quite good agreement with the data. However, we cannot say that this model can reproduce all the observations, since it cannot reproduce the correct behavior of Σ_{gas}.

The last model we present is Model 7. Its results are shown in Figures 5.17 and 5.18. This model has no threshold, a star formation efficiency which follows that one given by Boissier & Prantzos (1999) and no inside-out prescription. In this model we assume only one episode of accretion where halo forms first and then the disk follows. It differs from all the other models also because it adopts a simple Schmidt law for star formation. It can be seen that the SFR agrees well with the data by Rana (1991), while the surface gas density is too low in the inner part of the Galactic disk. This is again due to a too high SF efficiency in the inner disk.

From Figure 5.18 we can see that Model 7 predicts abundance gradients which are in good agreement with the observed data, especially for the outer parts of the Galactic disk. Therefore we can say that this is the only case with no threshold and no inside-out prescription where it is possible to well reproduce abundance gradients, although the surface gas density is too low in the inner part of the Galaxy.

In table 5.2 we summarize model successes and failures for abundance

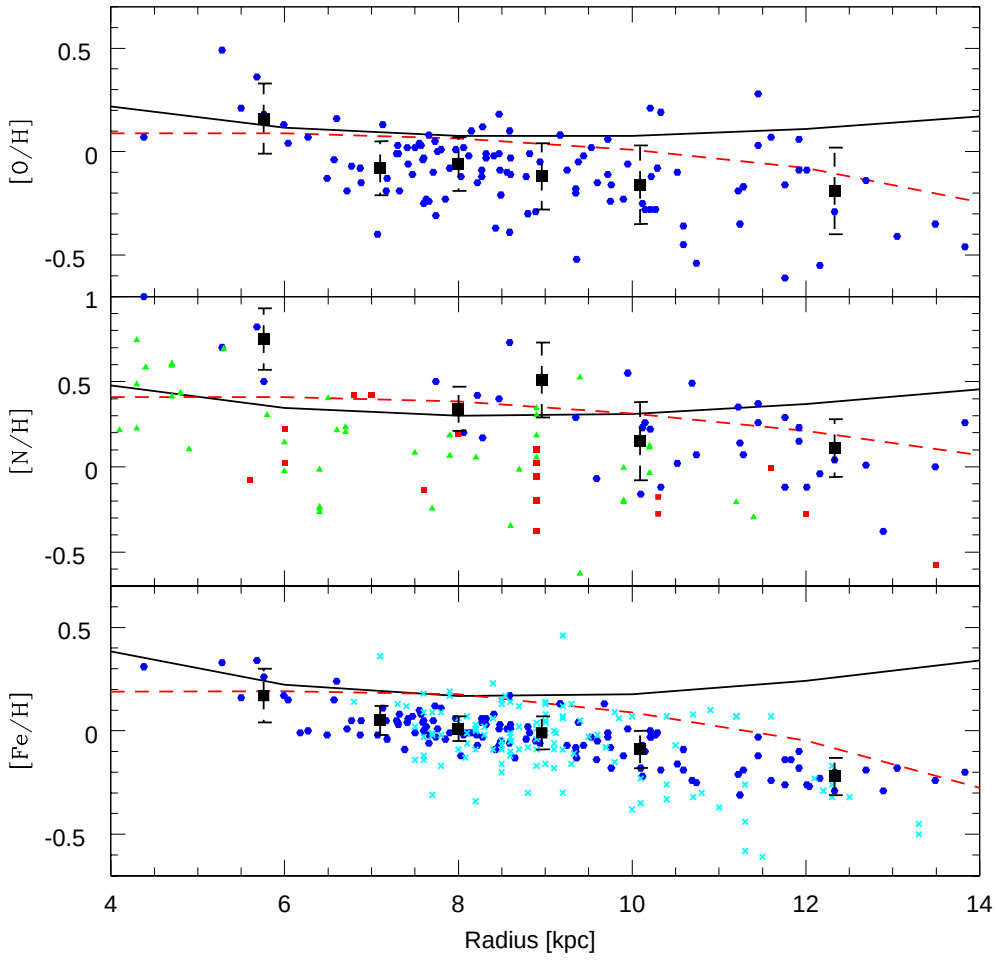

Figure 5.14: $[O/H]$, $[N/H]$ and $[Fe/H]$ vs radius for Model 5 (black solid line) and for Model C08 (red dashed line). The data are the same of Figure 5.4. This model shows that the presence of a variable τ along the galactic disk steepens the inner gradients, without however reducing the positive slope in the outer disk, as seen in Fig. 5.12.

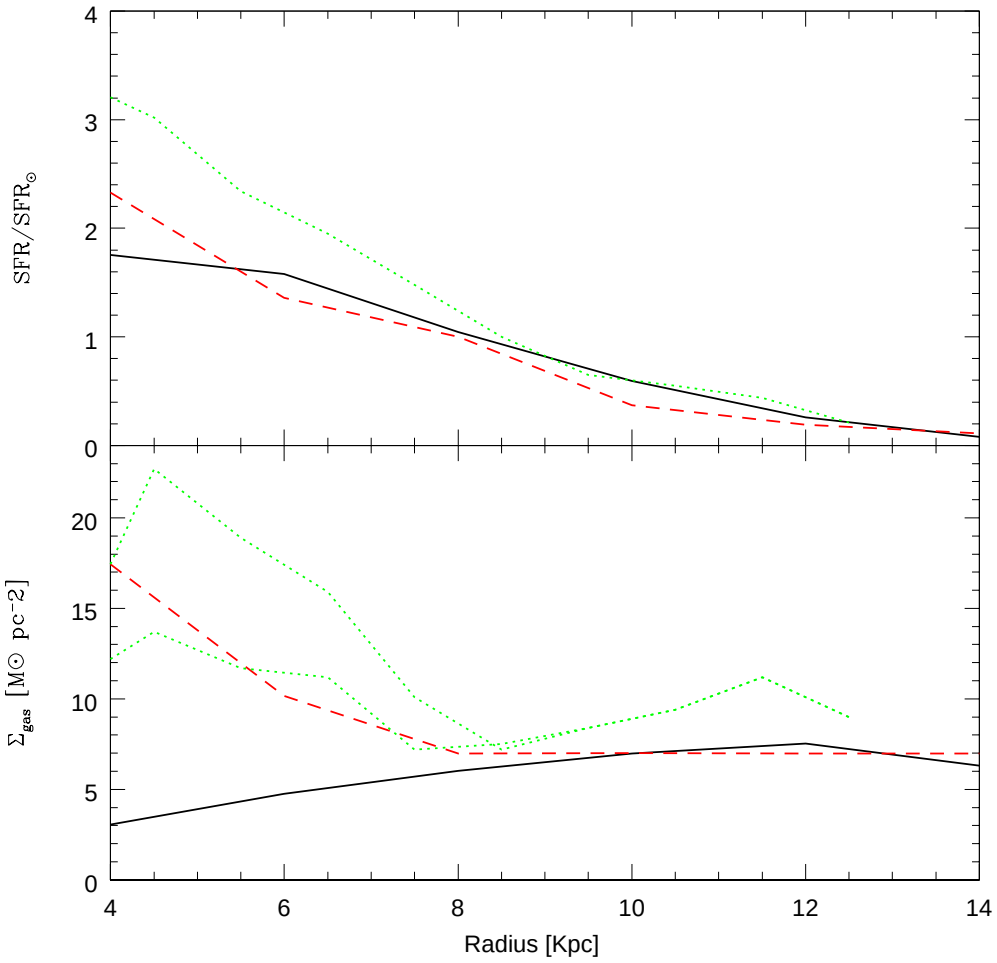

Figure 5.15: $SFR/SFR_{\odot}$ and surface gas density vs radius for Model 6 (black solid line) and for Model C08 (red dashed line). The data are the same of Figure 5.3.

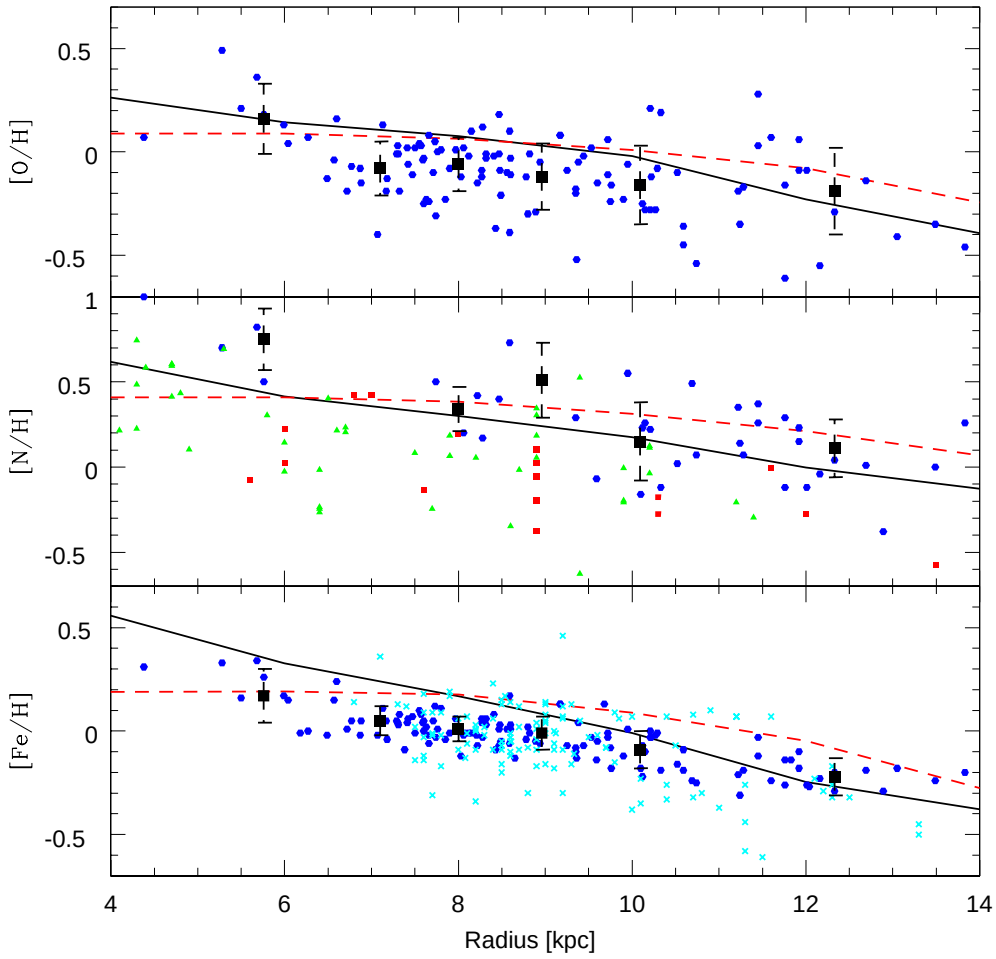

Figure 5.16: $[O/H]$, $[N/H]$ and $[Fe/H]$ vs radius for Model 6 (black solid line) and for Model C08 (red dashed line). The data are the same of Figure 5.4.

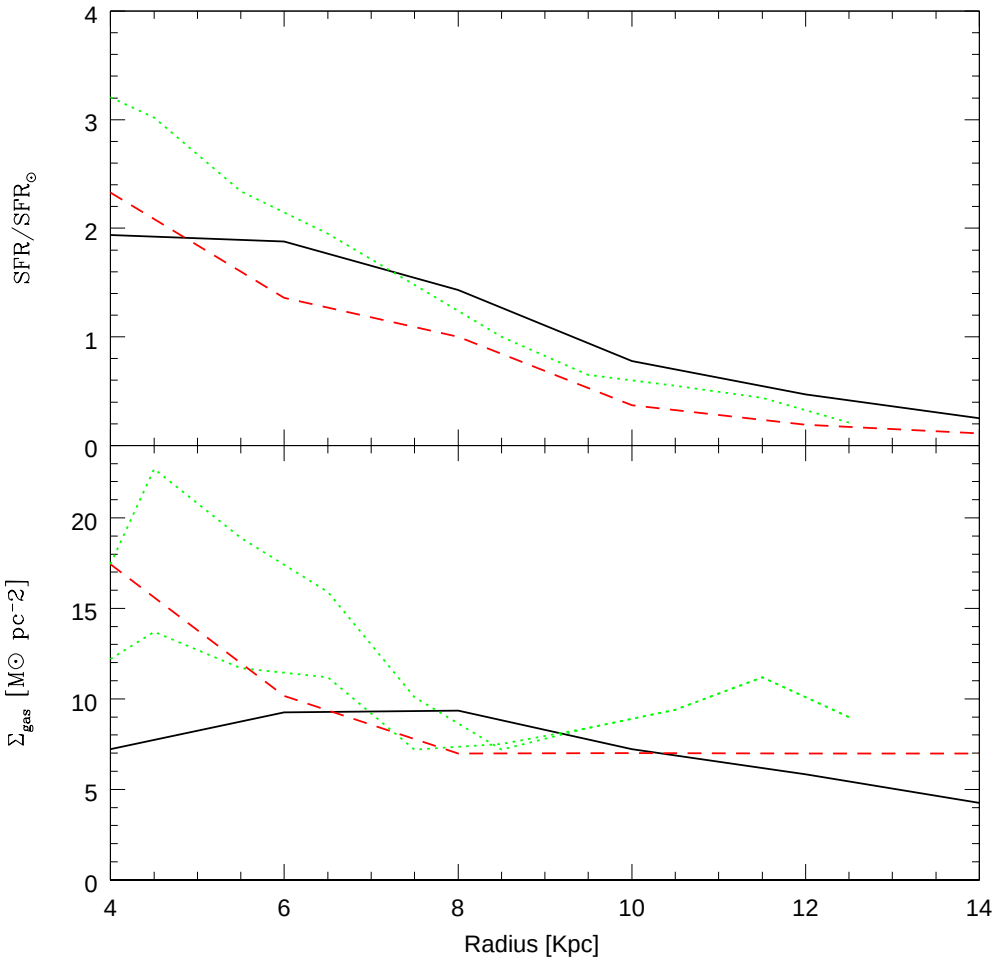

Figure 5.17: $SFR/SFR_{\odot}$ and surface gas density vs radius for Model 7 (black solid line) and for Model C08 (red dashed line). The data are the same of Figure 5.3.

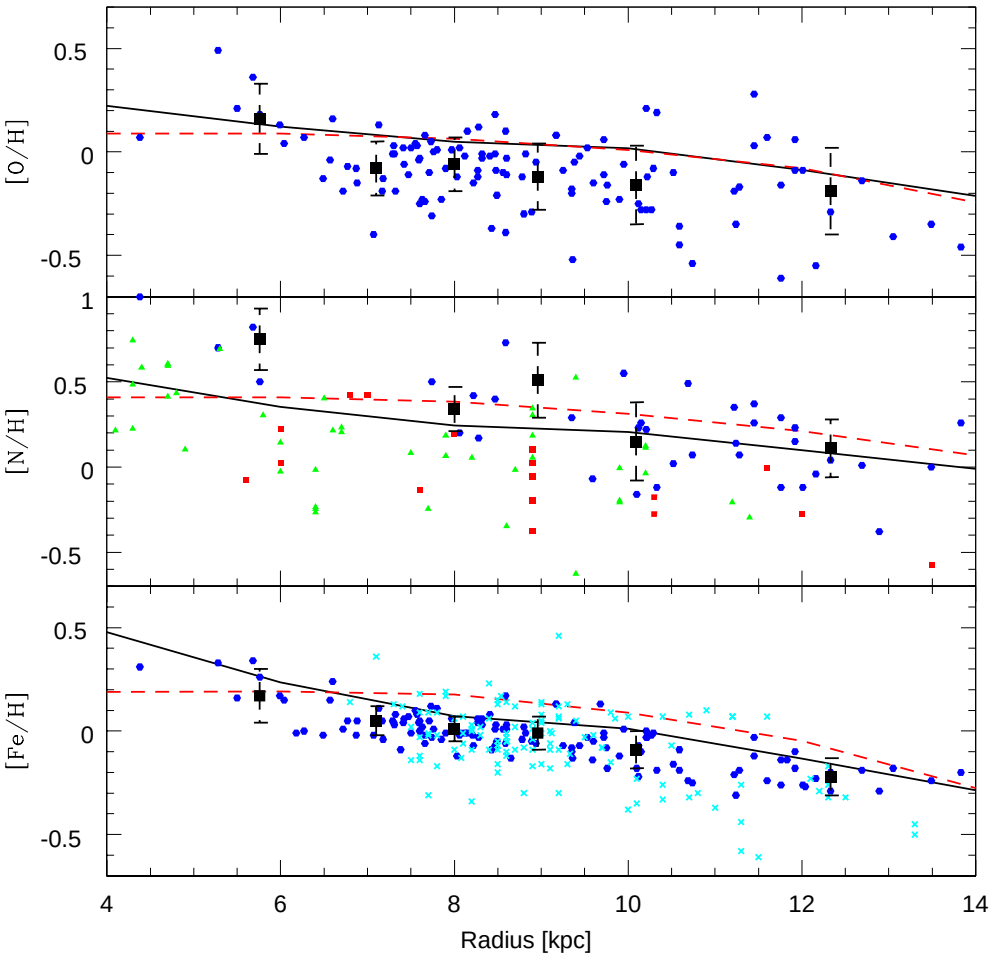

Figure 5.18: $[O/H]$, $[N/H]$ and $[Fe/H]$ vs radius for Model 7 (black solid line) and for Model C08 (red dashed line). The data are the same of Figure 5.4.

trends, surface gas densities and star formation rates.

Table 5.2: Models successes and failures. The second column shows the successes while the third column the failures.

Model	Successes	Failures
1	good agreement for the $SFR/SFR_{\odot}$	Σ_{gas} not reproduced in the outer Galactic disk abundance gradients completely flat
2	good agreement for the $SFR/SFR_{\odot}$ increased slope of the gradients in the outer disk	too low Σ_{gas} in the inner disk abundance gradients too flat in the inner disk
3	good agreement for the $SFR/SFR_{\odot}$ Σ_{gas} increases in the outer part of the disk slope of abundance gradients more pronunced in the outer disk	too low Σ_{gas} abundance gradients too flat in the inner disk
4	good agreement for the $SFR/SFR_{\odot}$	Σ_{gas} not reproduced in the outer Galactic disk abundance gradients increase along the galactic disk
5	good agreement for the $SFR/SFR_{\odot}$ slope of abundance gradients more pronunced in the inner disk	Σ_{gas} not reproduced in the outer Galactic disk abundance gradients increase in the outer Galactic disk
6	good agreement for the $SFR/SFR_{\odot}$ abundance gradients in good agreement with the observed data	Σ_{gas} increases along radius
7	good agreement for the $SFR/SFR_{\odot}$ abundance gradients in good agreement with the observed data	Σ_{gas} too low in the inner part of the Galactic disk

Chapter 6

Elliptical formation

In this chapter we study the effect of a cosmologically motivated infall law for the formation of a mean elliptical galaxy in order to understand its impact on the formation of the spheroids. We use the same simulation adopted to study Milky Way-like galaxies, even if in this case the parameter to identify the dark matter halos are different. In particular we consider the spin parameter, connected to the angular momentum of a galaxy. The novelty of this approach to model the formation of an elliptical galaxy consists in the fact that we identify a posteriori a possible dark matter halo which can host an elliptical galaxy.

Our approach is very simple. In particular ellipticals are tipically found in clusters of galaxies, whereas in our simulation we model an isolated elliptical galaxy. In a galaxy cluster there are some important physical processes (i.e. ram-pressure stripping, tidal stripping, harassment among others) that we do not consider in our DM-only simulation and that can influence the properties and the amount of the gas. Another important process that we do not consider is that ellipticals are likely to accrete not only gas during the mergers but also already formed stars. In this case, details on baryons properties become important and they cannot be ignored.

Other authors studied the formation and evolution of ellipticals, but with a different approach. Among the others, Thomas, Greggio & Bender (1999) adopted two different scenarios for the formation of an elliptical galaxy: a fast clumpy collapse and the merger of two spirals similar to the Milky Way.

Pipino & Matteucci (2006), instead, adopted an analitical infall law to study the formation and the chemical evolution of an elliptical galaxy.

6.1 Introduction to elliptical galaxies

Elliptical galaxies show an important uniformity in their photometric and chemical properties. The first proposed scenario of elliptical formation was the monolithic collapse scenario (Larson 1974; Matteucci & Tornambè 1987; Arimoto & Yoshii 1987; Chiosi & Carraro 2002). Ellipticals are assumed to have formed at high redshift as a result of a rapid collapse of a gas cloud. This gas is rapidly converted into stars by means of a very strong burst, followed by a galactic wind powered by supernovae and stellar winds. The wind, carring out the residual gas from the galaxy, inhibites further star formation. Minor episodes of star formation, related to gas accretion from the surrounding medium or interactions with neighbours, are not excluded, although they do not influence the galactic evolution.

The second proposed scenario for elliptical formation was the hierarchical clustering scenario. Hierarchical semi-analytic models predict that ellipticals are formed by several merging episodes which trigger starbursts and regulate the chemical enrichment of the system (White & Rees 1978). In this case massive ellipticals form at relatively low redshifts through major mergers between spiral galaxies (e.g. Kauffmann & White 1993; Kauffmann & Charlot 1998).

The high-redshift formation of elliptical galaxies is supported by observations showing also an increase in the strength of the metal absorption lines (mass-metallicity relation, e.g. Carollo, Danziger & Buson 1993; Gonzalez 1993; Davies, Sadler & Peletier 1993; Trager et al. 1998, 2000b) and a reddening of the stellar light (colour-magnitude relation, e.g. Bower et al. 1992) with the velocity dispersion of the galaxies. In other words, the most massive ellipticals are also the most metal-rich. This was interpreted by Larson (1974) as resulting from the galactic winds that should occur later in the most massive objects, allowing the star formation process to continue for a longer period. In the last years, however, this interpretation has been challenged. This because there was increasing evidence that the [Mg/Fe] ratio in the

dominant stellar population is larger than zero in the core of bright galaxies (e.g. Faber, Worthey & Gonzalez 1992), suggesting that the star formation lasted for a period shorter than the time at which the pollution from type Ia SNe becomes important (Matteucci 1994; Weiss, Peletier & Matteucci 1995). Moreover, the [Mg/Fe] ratio in the cores of elliptical galaxies increases with galactic mass (Worthey et al. 1992; Weiss et al. 1995; Kuntschner 2000) indicating that higher mass galaxies are, on average, older, more metal-rich and more α-enhanced than lower mass galaxies. Moreover the largest galaxies formed their stars $\sim$ 13 Gyr ago, whereas the mean age of low-mass objects is only $\sim$ 4 Gyr (e.g. Nelan et al., 2005) in a manner resembling the 'inverse wind model' of Matteucci (1994). This is clearly at variance with the scenario of Larson. Other possible solutions to the increase on [Mg/Fe] as a function of galactic mass are a variable initial mass function (IMF) and/or a decrease of the DM content as a function of galactic mass (Matteucci, Ponzone & Gibson 1998). In Pipino & Matteucci (2004) the authors showed that the majority of the optical properties of elliptical galaxies can be simultaneously reproduced under the assumption that the formation process, occurring at high redshift (as in the monolithic collapse scenario), is stronger and faster in more massive objects with respect to the less massive ones. On the other hand, evidences favouring the hierarchical scenario are represented by the observed interacting galaxies, ellipticals with disturbed morphologies (e.g. Kormendy & Djorgovski 1989).

Evidences of very recent (but very modest) star formation in early-type galaxies come from the Galaxy Evolution Explorer (GALEX) data (e.g. Yi et al. 2004, Salim et al. 2005). The sensitivity of GALEX to very low star formation rates ($\sim 10^{-3} M_{\odot}\mathrm{yr}^{-1}$, Salim et al. 2005) provide us with more reliable data on recent minor episodes of star formation in ellipticals. Therefore one cannot completely rule out the possibility of late mergers, although they do not represent the main process of galaxy formation as they seem to be limited only to (a fraction of) the low mass objects. Monolithic models, obviously, cannot reproduce recent star formation if there is not late-time accretion of satellites. The cosmological model, instead, has a residual star formation by definition. For this reason it is interesting to compare it with the data by GALEX.

Kaviraj et al. (2008a) showed that the medium value of recent star formation in early-type galaxies, defined by the authors as the mass fraction of stars that form in a galaxy within the last 1 Gyr of look-back time in its rest frame, is ~ 5.5 per cent.

A residual star formation at low redhshift seems quite common in Brightest Cluster Galaxies (BGCs) hosted in cool-core clusters (Hicks & Mushotzky 2005, O'Dea et al. 2008, Bildfell et al. 2008). Using Bildfell et al. (2008) sample, Pipino et al. (2008b) demonstrate, *for the first time*, a one-to-one correspondence between blue cores in elliptical galaxies and a UV-enhancement observed using GALEX. However, it should be said that only a small fraction of elliptical galaxies is showing current star formation. In any case it is interesting to understand if this supposed recent star formation really exists or not and how it can influence the chemical evolution of ellipticals.

Generally, models for the formation of normal ellipticals predict that the star formation rate stopped several Gyrs ago. In fact, besides the models quoted before, Merlin & Chiosi (2006) found that the star formation in early-type galaxies was completed within 4 Gyr, showing that a strong wind occurred. The same was found by Kawata & Gibson (2003a). They showed that the star formation stops abruptly at an early epoch due to the galactic wind. In another paper (Kawata & Gibson 2003b) the authors showed that the radiative cooling becomes more efficient, and thus the gas infall rate increases, with decreasing mass of elliptical galaxies.

6.2 The cosmological infall law

As already said, here we use the same cosmological simulation described in Chapter 3. In this case, however, we need a DM halo which can host an elliptical galaxy, not a spiral one. Therefore to identify the DM halos that can host an elliptical galaxy we used selection criteria different than those adopted to select a MW-like spiral galaxy. The first one is the mass of the halo. We want to study a mean elliptical galaxy, so it is important to chose an interval of masses in which we can find it. The second characteristic is the spin parameter. This parameter is a measure of the angular momentum of the halo and, therefore, we look for a small spin parameter in order to be

sure to consider a DM halo which can host an elliptical galaxy. These are the selectioned characteristics:

- mass between $1 \cdot 10^{12} M_{\odot}$ and $5 \cdot 10^{12} M_{\odot}$;
- spin parameter $\lambda < 0.04$;

We found 22 DM halos compatible with our selection criteria. We label them with their F-o-F group number. We assumed that the baryonic matter follows the same accretion pattern as the dark matter and that it represents 19% (the cosmological baryon fraction) of all the infalling matter. In this way, we obtained the baryon infall law from the mass accretion history of each halo.

Having 22 infall laws and knowing that elliptical galaxies form the bulk of their stars rapidly, we looked for a halo with a consistent mass accretion history at high redshift. This characteristic, in conjunction with a low spin parameter, was found only in one halo, being representative of a general elliptical galaxy. One may argue that this halo is not so representative, being these three characteristics not essential to characterize an elliptical galaxy. However the mass, the spin parameter and the redshift of formation of a galaxy are the same parameter used in Chapter 4 to identify a spiral galaxy similar to the Milky Way, where we obtained good results.

6.3 The model by Pipino & Matteucci (2004)

We implement the cosmologically motivated infall law into the Pipino & Matteucci (2004) (hereafter PM04) chemical evolution model for elliptical galaxies. This model is an updated version of the multizone model of Martinelli et al. (1998) and Pipino et al. (2002). For the star formation rate ψ they adopted the following law:

$$\psi(t) = \nu \cdot \frac{\rho_{gas}(t)}{\rho_{gas}(0)}. \tag{6.1}$$

The constant ν, representing the star formation efficiency, is an increasing function of the galactic mass in order to reproduce the 'inverse wind model' (Matteucci 1994; Matteucci et al. 1998).

For type Ia SNe they assumed a progenitor model made of a C-O white dwarf plus a red giant (Whelan & Iben 1973). The resulting rate is:

$$R_{SNIa} = A \int_{M_{Bm}}^{M_{BM}} \psi(M_B) \int_{\mu_m}^{0.5} f(\mu)\psi(t - \tau_{M2})\, d\mu\, dM_B. \qquad (6.2)$$

(Greggio & Renzini 1983; Matteucci & Greggio 1986), where M_B is the total mass of the binary system, $M_{Bm} = 3M_\odot$ and $M_{BM} = 16M_\odot$ are the minimum and maximum masses allowed for the adopted progenitor systems, respectively. $\mu = M_2/M_B$ is the mass fraction of the secondary and μ_m is its minimum value. The constant A represents the fraction of binary systems in the IMF which are able to give rise to SNIa explosions.

For the infall law PM04 adopted the expression:

$$\Big[\frac{dG_i(t)}{dt}\Big]_{infall} = X_{i,infall}\; C\; e^{-t/\tau}. \qquad (6.3)$$

where $X_{i,infall}$ describes the chemical composition of the accreted gas, assumed to be primordial, and τ is the infall time-scale. C is a constant obtained by integrating the infall law over time and requiring that $\sim 90\%$ of the initial gas has been accreted at the time when the galactic wind occurs.

Differently from PM04, here we use the yields by Woosley & Weaver (1995).

6.4 Results for an elliptical galaxy

We study three different models. Model 1 is the same model as in Pipino & Matteucci (2004), with the difference that we on purpose turned off the galactic wind (a natural consequence of SN feedback), in order to have a residual star formation rate at low redshift; Model 2, instead, is exactly the same model as in Pipino & Matteucci (2004). The wind occurs after 0.92 Gyr from the beginning of the formation of the galaxy, when the thermal energy of the gas heated by SNe (II and Ia) equates the binding energy of the gas, thus halting the star formation. Model 3 is our cosmological model. In this case, we maintained all the characteristics of Model 1, but changing the infall law. In this case we do not have galactic wind since we want to have a residual present time star formation rate.

In Table 6.1 we show the assumed luminous mass and star formation efficiency (i.e. the star formation rate per unit mass of gas) and the time of formation (time at which the galaxy accreted half of its mass) for all the models. It can be seen that Model 3 needs a much longer time to accumulate half of its mass (a factor of 10 compared to models 1 and 2).

Table 6.1: Luminous mass, star formation efficiency and time of formation for all the models.

Model	M_{LUM} $[M_\odot]$	ν	τ [Gyr]
1	$1.32 \cdot 10^{11}$	10	0.4
2	$1.08 \cdot 10^{11}$	10	0.3
3	$1.32 \cdot 10^{11}$	10	4.0

In subsection 6.4.1 we show several plots where we compare the three models. In the upper panels of each plot it can be seen Model 1, i.e. the model by Pipino & Matteucci (2004) without wind. In the middle panels we show the same model, but with the wind (Model 2). In the bottom panel it can be seen Model 3, i.e. the cosmological model without wind. We show the different infall laws and total masses, the star formation rate and the SNIa rate, the behavior of the [Fe/H] ratio as a function of time and, finally, the [O/Fe] and [Mg/Fe] as a function of [Fe/H].

In subsection 6.4.2 we present some comparisons of our results with observable data given by Thomas et al. (2005), Mannucci et al. (2008) and Kaviraj (2008b). In particular, we show the mean values for [Fe/H], [Mg/H] and [Mg/Fe] for each model, the current SNIa and SNII rates and the mass in stars formed in the last 1.0 and 6.2 Gyr by each model.

6.4.1 Comparison between the three models

Figure 6.1 shows the infall laws for all the models as a function of time. The infall law of Model 1 and 2 has a peak at high redshift, and lasts for 1 Gyr. In particular, the infall law of Model 2 becomes equal to zero after the peak, since the wind starts. The infall law of Model 3, as we know, is cosmologically derived. It does not present a peak, having an important accretion episode

between 2 and 5 Gyr and several minor episodes during the whole formation of the galaxy.

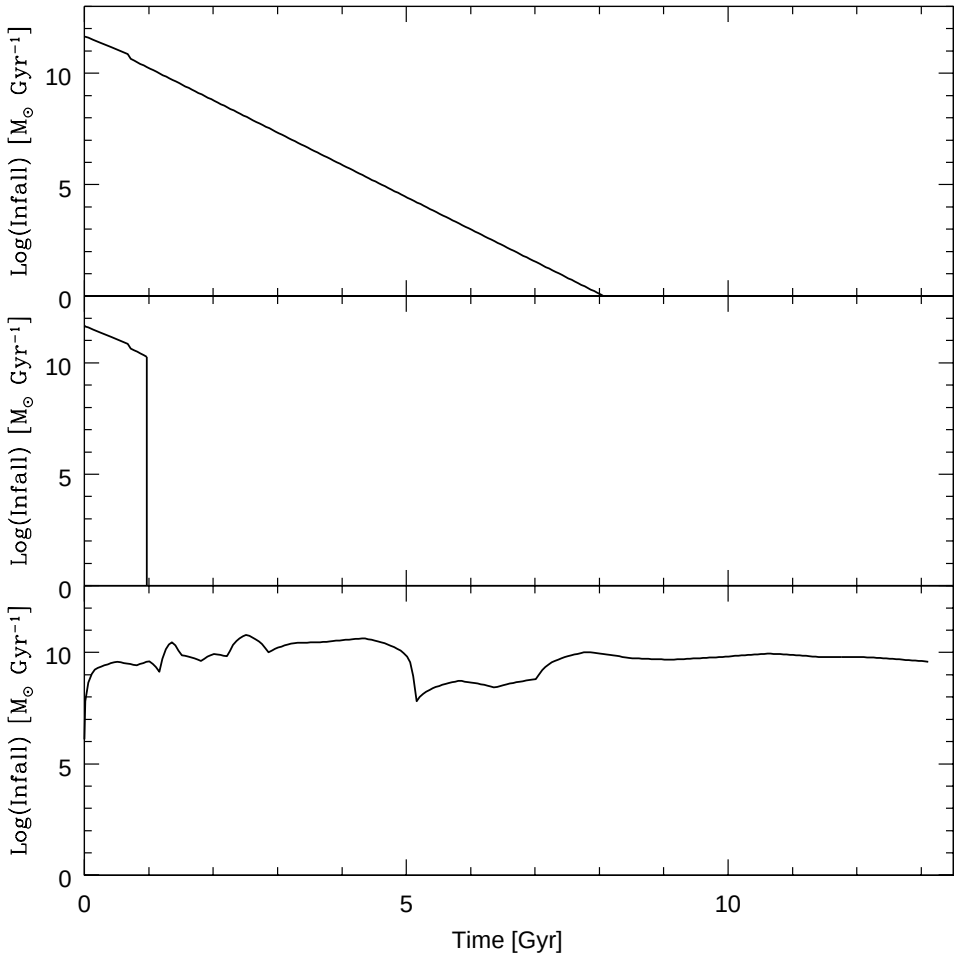

Figure 6.1: The gas infall rate vs time for the three models. Upper panel: Model 1; Middle panel: Model 2; Bottom panel: Model 3.

In Figure 6.2 it can be seen the total mass of all the models as a function of time. The mass of Model 1 increases during the first Gyr of formation, remaining constant when the infall law rapidly decreases. Model 2 has the same behavior during the first Gyr, whereas it slightly decreases after 1 Gyr,

since the wind starts and part of the gas is ejected. The mass accretion history of Model 3, instead, is very different from those of Model 1 and 2. It increases very slowly until $\sim$ 2.5 Gyr, when the slope increases. Then, between $\sim$ 4.8 and $\sim$ 7.5 Gyr it remains more or less constant, starting to increase again up to the end of the formation of the galaxy.

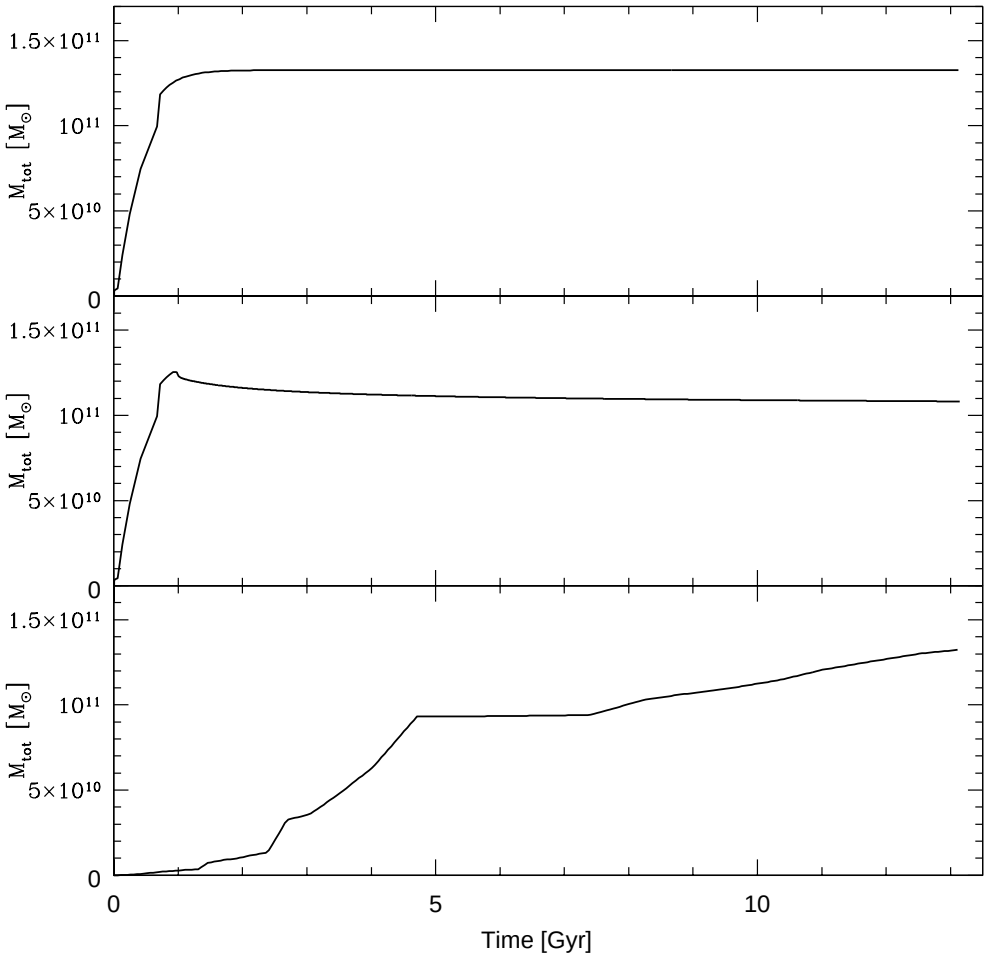

Figure 6.2: Total mass vs time for the three models. Upper panel: Model 1; Middle panel: Model 2; Bottom panel: Model 3.

Figure 6.3 shows the star formation rate as a function of time for the

three models. It can be seen that it is very similar to the infall rate of each model. The difference between Model 1 and 2 is that, when the wind starts, the SFR of Model 2 suddenly becomes equal to zero, whereas in Model 1 it goes to zero very slowly. In Model 3 the SFR never stops, since in this case there is no wind and the infall rate is always different from zero.

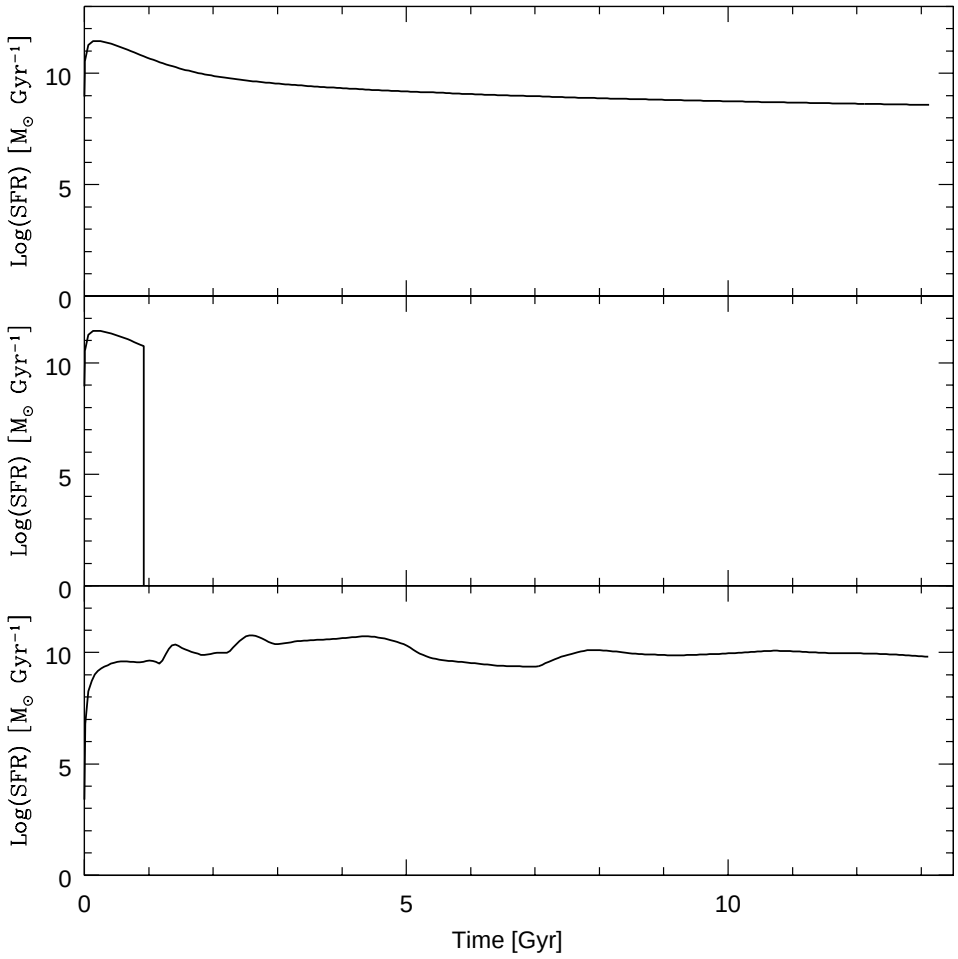

Figure 6.3: The star formation rate (SFR) vs time for the three models. Upper panel: Model 1; Middle panel: Model 2; Bottom panel: Model 3.

In Figure 6.4 it can be seen the SNIa rate as a function of time. The

behavior of Model 1 and 2 are very similar, even if the SNIa rate of Model 2 decreases more rapidly. Model 3 produces a large amount of SNIa between 2 and 7 Gyr, when the infall rate is larger. After this interval the SNIa rate becomes nearly constant until the end of the evolution. We do not present a plot for SNII because, being the life of their progenitor very brief, their behavior traces out the SFR.

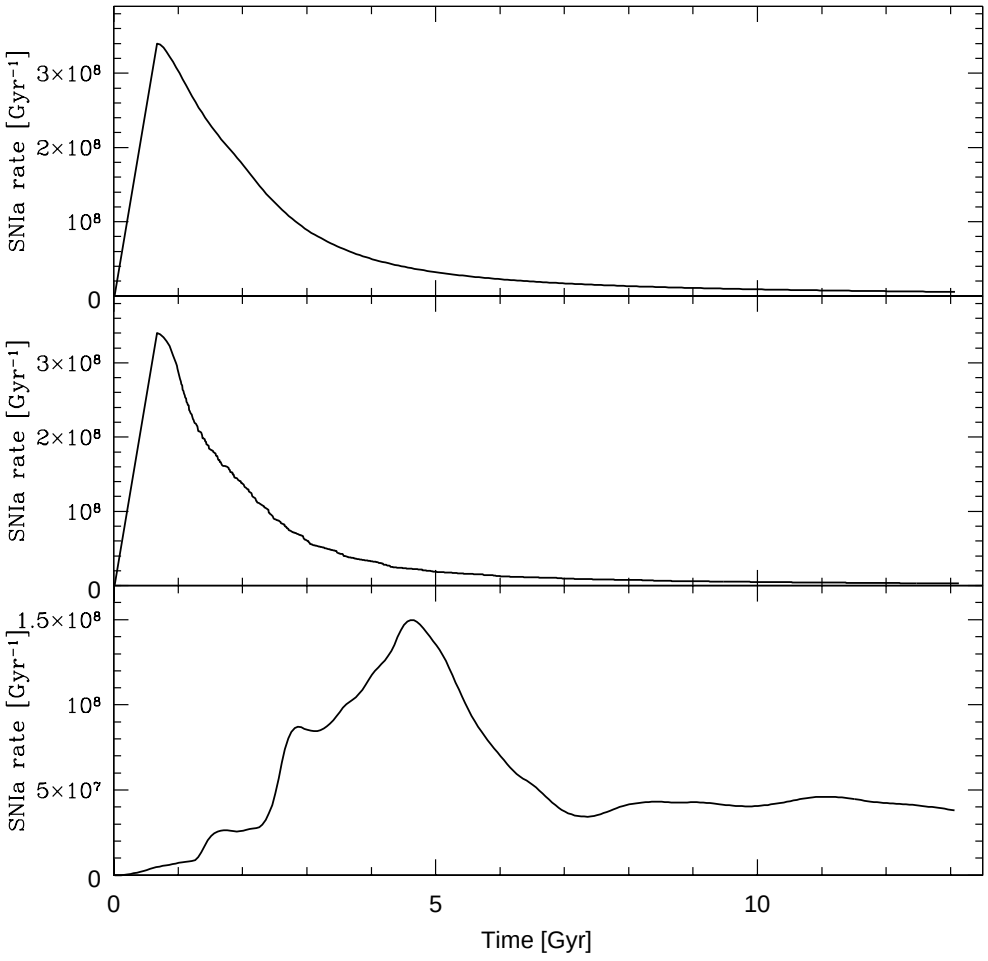

Figure 6.4: The SNIa rate vs time for the three models. Upper panel: Model 1; Middle panel: Model 2; Bottom panel: Model 3.

Figure 6.5 presents the [Fe/H] as a function of time for all the models. Both Model 1 and Model 2 reach the largest value for the [Fe/H] ratio after about 2 Gyr from the beginning of the formation. After this peak the [Fe/H] slightly decreases, in particular in Model 2 where, at the end, [Fe/H] $\sim$ 1.2. In Model 3 the [Fe/H] ratio has a behavior very different form that of Model 1 and 2. In the first three Gyrs the [Fe/H] has several peaks and depressions. The latter are due to the two peaks in the infall rate, at 1.5 and 2.5 Gyr which dilute the Fe abundance because the infalling gas is assumed to have a primordial chemical composition (no metals). After the first peaks the [Fe/H] ratio increases rapidly, then becoming constant for more or less two Gyr, decreasing again and then keeping constant and equal to $\sim$ 1.0 dex at the end of the present time.

In Figure 6.6 it can be seen the [Mg/Fe] as a function of [Fe/H]. All the three models initially have the same behavior. However the [Mg/Fe] of Model 3 starts to decrease at lower metallicities than in Model 1 and 2. In Model 3 the changing in slope happens at [Fe/H] $\sim$ -1, whereas in Model 1 and 2 it happens at [Fe/H] $\sim$ 0. In Model 1 and 2 the [Mg/Fe] becomes equal to zero at [Fe/H] $\sim$ 0.4, whereas in Model 3 the [Mg/Fe] ratio becomes zero when the [Fe/H] $\sim$ 0.1. This is due to the longer and less efficient star formation predicted by Model 3. In fact, different star formation histories produce different [α/Fe] abundance patterns, favoring high values for a large interval of [Fe/H] in regimes of long and brief star formation (Matteuccci, 2001). The high and short star formation rate produced [Mg/Fe] ratios in excellent agreement with those measured in the Bulge (Ballero et al. 2007) and in ellipticals (Pipino & Matteucci 2004).

6.4.2 Comparison with observables

In order to study the mean properties of the stellar component in ellipticals, we need to average quantities related to the mean abundance pattern of the stars, which, in turn, can allow a comparison with the observed integrated spectra[1]. To this scope, we recall that both real and model galaxies are made

[1]We recall that in elliptical galaxies it is not possible to resolve single stars and, hence, determine the stellar metallicity distribution.

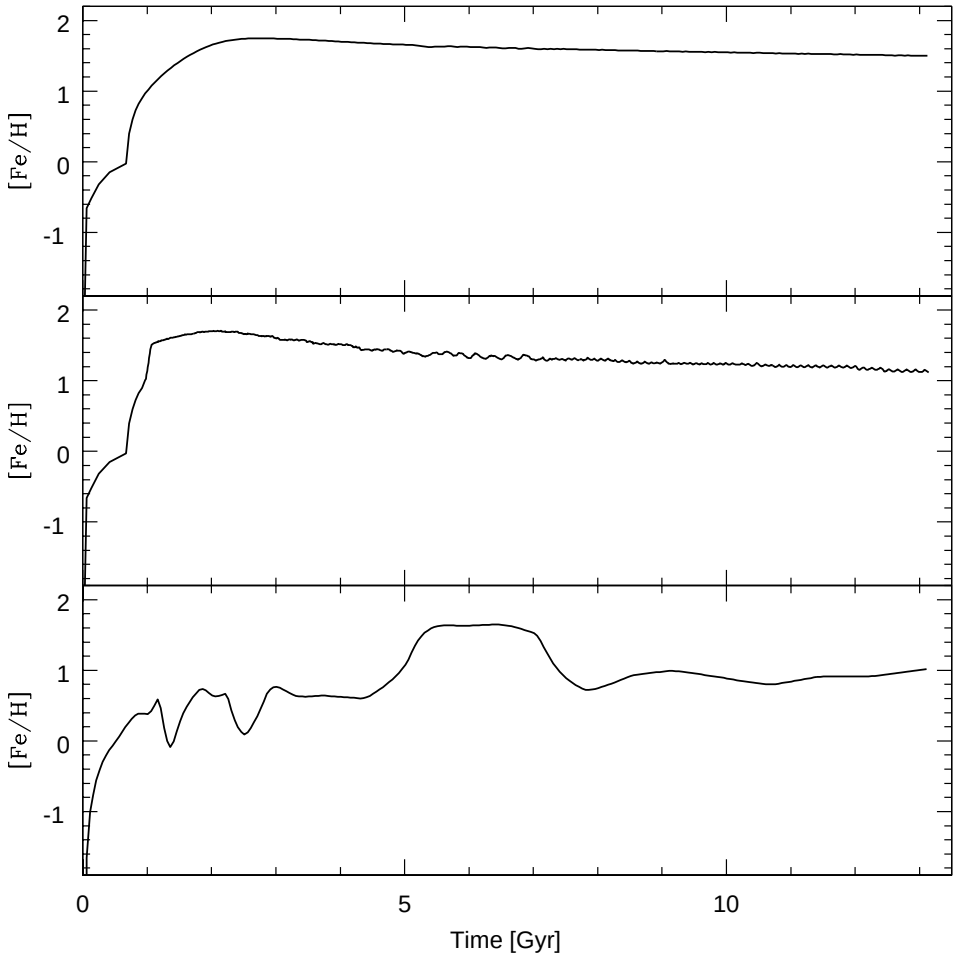

Figure 6.5: [Fe/H] vs time for the three models. Upper panel: Model 1; Middle panel: Model 2; Bottom panel: Model 3.

of CSP, namely a mixture of several SSP, differing in age and chemical composition according to the galactic chemical enrichment history, weighted with the SF rate. On the other hand, the observed line-strength indices are usually tabulated only for SSPs as functions of their age, metallicity and (possibly) α-enhancement. In particular we make use of the mass-weighted mean stellar metallicity as defined by Pagel & Patchett (1975, see also Matteucci 1994):

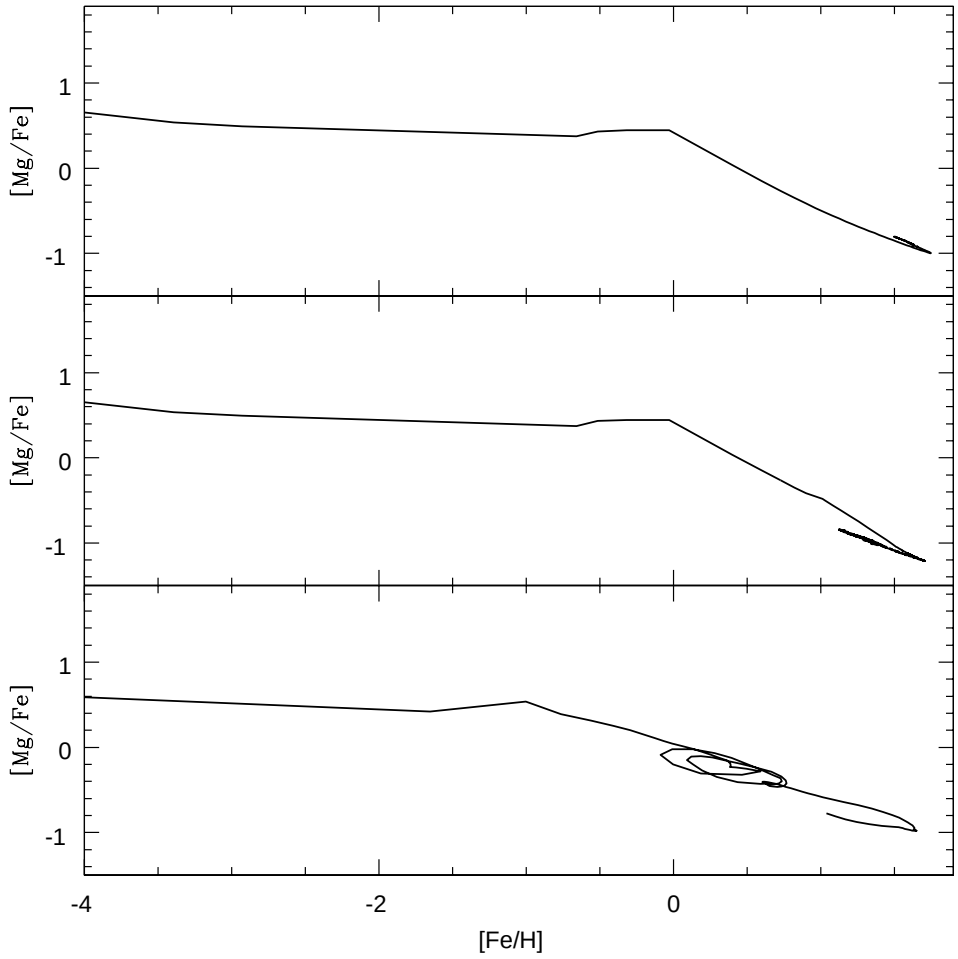

Figure 6.6: [Mg/Fe] vs [Fe/H] for the three models. Upper panel: Model 1; Middle panel: Model 2; Bottom panel: Model 3.

$$< Z >= \frac{1}{S_f} \int_0^{S_f} Z(S)\, dS. \tag{6.4}$$

where S_f is the total mass of stars ever born contributing to the light at the present time and Z is the metal abundance (by mass) in the gas out of which an amout of stars S formed. In practice, we make use of the stellar

mass distribution as a function of Z in order to derive the mean metallicity in stars.

In Table 6.2 we show the mean value for [Fe/H], [Mg/H] and [Mg/Fe] for all the models. The mean values for Model 1 and Model 3 are taken during the whole lifetime of the galaxy, while in Model 2 the mean values are representative for the whole period prior to the wind. It can be seen that the [Mg/Fe] value for Model 3 is too low and it is in contrast with the values given by Thomas et al. (2005), where for an elliptical galaxy of the same mass the value of the fit of the observed data is ~ 0.2 dex

Table 6.2: Mean values for [Fe/H], [Mg/H] and [Mg/Fe] for all the models. The time for Model 2 is the time at which the wind occurs.

Model	Time [Gyr]	[Fe/H]	[Mg/H]	[Mg/Fe]
1	13.12	0.677	0.358	0.434
2	0.92	-0.078	0.270	0.511
3	13.12	0.777	0.299	-0.304

However, Thomas et al. (2004) found that a non-negligible fraction of low-mass ellipticals in their sample shows evidences of a young (i.e. age < 2 Gyr) and metal-rich ($[Z/H] \sim 0.2$) stellar population which represents $\sim 10 - 20\%$ of their total stellar mass. These values are independent from the environment and the typical $[\alpha/\mathrm{Fe}]$ of this population are ~ 0.2 dex lower than the bulk of the stars, as expected if the young component formed out of gas strongly polluted by SNIa.

As seen in the introduction, evidences of very recent (but modest) star formation in early-type galaxies come from the GALEX data. In Table 6.3 we show the mass in stars formed in the last 1 and 6.2 Gyr by the three models, comparing it with the total amount of stars and with the observed values by Kaviraj (2008b). We can see that Model 2 does not form stars in the last 6.2 Gyr. These is due to the presence of a wind which stops the star formation at early times. Model 3 predicts very well the mass of stars formed in the last Gyr, whereas it produce less stars than expected in the last 6.2 Gyr. The residual star formation of Model 1, instead, cannot reproduce neither the amount of stars formed in the last Gyr (according to

Galex) nor those formed in the last 6.2 Gyr, being the obtained values too low. We recall, however, that elliptical galaxies with some residual recent star formation are only a minor fraction of the whole class of ellipticals; therefore the disagreement between Model 1 and the GALEX observations is not emphasizing any model deficiency.

Table 6.3: Mass in stars formed in the last 1.0 and 6.2 Gyr for all the models compared with the total amount of stars. Observed values by Kaviraj (2008b).

Model	M_* [$M_\odot$] (last 1.0 Gyr [z = 0.08])	M_* [$M_\odot$] (last 6.2 Gyr [z = 0.7])	M_* [$M_\odot$] (13.12 Gyr)
1	$4.17 \cdot 10^8$ (0.21%)	$3.66 \cdot 10^9$ (1.85%)	$1.98 \cdot 10^{11}$
2	0.00 (0.00%)	0.00 (0.00%)	$1.58 \cdot 10^{11}$
3	$7.95 \cdot 10^9$ (4.25%)	$5.54 \cdot 10^{10}$ (29.63%)	$1.87 \cdot 10^{11}$
Kaviraj (2008b)	1 - 6 %	5 - 13 %	

Table 6.4 shows the current SNIa and SNII rate for the three models. They are compared with the observed values by Mannucci et al. (2008) and they are in units of SNuM (SN per century per $10^{10} M_\odot$ of stellar mass). We can see that Model 3 predicts too large an amount of SNIa and SNII. In particular the value of SNIa for Model 3 is at ~ 32 standard deviations from the observed mean.

As seen in Table 6.4, the SN rates for Model 3 are too high with respect to the observed data given by Mannucci et al. (2008). From Table 6.3 we can see that this is due to the residual star formation of Model 3, not seen in the other two models (especially in Model 2), but confirmed by GALEX. Therefore we find a remarkable lack of consistency between the star formation rates inferred by GALEX and the limits on the the SN rates. In fact, in principle we should be able to observe SNII events if the star formation is still on-going. However, the lower brightness of SNII, combined with the fact that the recent star formation takes place in the the bright centres of the galaxies, implies that the probability of finding SNII with current surveys is probably quite low (Mannucci et al. 2007).

Table 6.4: Current SNIa rate and SNII rate in SNum for the three models. Observed values by Mannucci et al. (2008).

Model	SNIa rate [SNuM]	SNII rate [SNuM]
1	0.060	0.028
2	0.046	0.000
3	0.673	0.767
Mannucci et al. (2008)	$0.058^{+0.019}_{-0.015}$	< 0.017

Chapter 7

Conclusions

We have tested different gas infall laws for models of the formation of the Milky Way and especially cosmologically derived infall laws, obtained by means of cosmological simulations for the formation of the DM halo of the Milky Way. In particular, we assumed that the accretion law for the DM halo holds also for the baryonic matter. We found four different DM halos with properties compatible with a disk galaxy and one in particular seemed better than the others. All these infall laws were then compared with the one proposed by Chiappini et al. (1997), called the two-infall law, which predicts that there were two main accretion episodes which formed the halo-bulge-thick disk and the thin disk, respectively. We found that our best cosmological infall law is very similar to the two-infall one, which has already proven to be able to reproduce the majority of the chemical properties of the Milky Way in the solar neighbourhood. Our cosmological infall laws have been tested in a detailed chemical evolution model for the Milky Way, following the evolution of several chemical elements by taking into account stellar lifetimes, SN progenitors and stellar nucleosynthesis.

We have also shown that adopting a cosmologically motivated infall law, resembling the one of C97, for the solar neighbourhood but not predicting an inside-out formation of the Galactic disk, we were not able to reproduce the [O/H] gradient in the inner parts of the disk. So we tested several models in order to find the best values of four parameters to best reproduce the $SFR/SFR_{\odot}$, Σ_{gas} and the [O/H], [N/H] and [Fe/H] gradients along the

Galactic disk, for our best model and for the model by C97. These four parameters are the threshold gas density for the star formation, the star formation efficiency ν, the inside-out prescription $\tau(r)$ (i.e. the variation of the timescale for the formation of the Galactic disk) and the surface halo mass density.

In the last part of the thesis we tested a cosmologically derived infall law for the formation of an elliptical galaxy. We compared our results with those produced by the model by Pipino & Matteucci (2004), with and without galactic wind, focusing on constraints pertaining to the chemical evolution.

Our main conclusions can be summarized as follows:

- The cosmological laws, and in particular our preferred best model, seem to fit quite well all the data. This law predicts two main accretion episodes which can be identified with the formation of the halo-thick disk and thin disk, respectively, very similar to the two-infall law. Moreover, there seems to be a gap of 1-2 Gyr in the SFR between the two episodes, larger than predicted by Chiappini et al. (1997) (< 1 Gyr). The gap is due mainly to the adoption of a threshold gas density for the star formation rate. Such a gap seems to have been observed in abundance patterns, in particular at [Fe/O] vs. [O/H] (Gratton et al. 1996) and at [Fe/Mg] vs. [Fe/H] (Fuhrmann 1998), although new data are necessary to draw firm conclusions. The model including this cosmological infall law, being similar to the two-infall model, can well reproduce most of the observational constraints. However this model has some problems to fit the G-dwarf metallicity distribution, since it predicts two different peaks: we speculate that the first peak represents the stars of the halo and thick disk while the second peak represents the stars of the thin disk. The same metallicity distribution computed for the central region should also include the bulge stars. The predicted timescales for the formation of the halo-thick disk and the thin disk, respectively, are in excellent agreement with those suggested by Chiappini et al. In particular, the halo-thick disk must have formed on a timescale not longer than 1-2 Gyr whereas the thin disk in the solar vicinity took at least 6 Gyr to assemble 60% of its mass. As a consequence of the gap between the halo-thick disk and the thin disk,

we predict that the thin disk is at least 2 Gyr younger than the halo.

- The other cosmological infall laws are characterized by several minor accretion events after the two main ones and predict larger gaps in the SFR which are not observed in the [Fe/O] vs. [O/H] and [Fe/Mg] vs. [Mg/H] which indicate a gap not larger than 1-2 Gyr (see Fuhrnamm 1998 and Gratton et al. 2000).

- Our results can be compared with the work of Robertson et al. (2005), in which the authors studied the chemical enrichment of the stellar halo of the Milky Way, using the prescriptions of the hierarchical scenario. They supposed that most of the mass in the MW halo was acquired via mergers with massive dIrr-type DM halos, occurring at a look-back time of $\sim$ 10 Gyr. They used three examples of mass accretion history, assuming that the cumulative mass accretion in individual DM halos can be well described by an analytical function obtained by Wechsler et al (2002).

  Moreover, they assumed that the cold gas infall rate tracks the DM accretion rate and that the fraction of cold gas is equal to 2%.

  In order to build the stellar halo of the Milky Way they used a dIrr-type dark matter halo with a virial mass $M_0 = 6$ x $10^{10} M_{\odot}$, accreted 9 Gyr ago, following their assumed accretion law. In this case the time available for the star formation and the consequent chemical enrichment is only $\sim$ 2.6 Gyr and therefore the chemical enrichment due to SNIa was limited. We did not use the accretion of a dIrr galaxy to build the stellar halo of the MW. We obtained the mass accretion history of the DM halo directly from the cosmological simulation, done with the public tree-code GADGET2 (Springel 2005). For this reason we accrete only DM and cold gas and not already formed dwarf galaxies, with their own stars and gas. Moreover we study the chemical enrichment of halo and disk and not only of the stellar halo.

- The fact that all our four suitable DM halos show an accretion law that resembles that used in the two-infall model could be linked to the way in which such halos assemble. Indeed, they have their last major

merger at high redshift, larger than $z = 2.5$, by selection and they reach a mass larger than 50% of their final one at lower redshift. As a consequence of our requirement not to have late major mergers, such late assembly happens via accretion of material from the field, namely filaments, or via minor mergers. These two epochs of important accretion qualitatively correspond to the two peaks used in the two-infall model and give it a cosmological motivation. Obviously the details of the late accretion episode will depend on the dynamical history of the single DM halo, and will generate differences in the chemical patterns of individual late-type galaxies without destroying their overall properties. On the other hand, halos should acquire their angular momentum thanks to the cosmological torques acting at high redshifts on the material (both baryons and dark matter) which will coalesce to form them. Such torques will also influence their mass accretion histories. Thus, selecting DM halos with high spin values could also result in selecting halos with similar dynamical histories. Astrophysical processes acting on baryons, e.g. feedback, should not be able to dramatically alter this scenario. Finally we note that, while in the two-infall model the timing of the two episodes is a free parameter, in the cosmological infall scenario the timing is directly given by the gravitational evolution of the halos. In this sense, the agreement between such models is not a-priori guaranteed and could be interpreted as an interesting link between the morphological properties of the late-type galaxies (used to fix our requirement) and their chemical properties, via the hierarchical model.

- We found that it is impossible to fit all the disk constraints at the same time without assuming an inside-out formation for the Galactic disk together with a threshold in the gas density for the star formation rate. In particular, the inside-out formation is important to reproduce the right slope of the abundance gradients in the inner disk, whereas the threshold gas density is important to reproduce the slope of the gradients in the outer disk. Models with a constant timescale for the disk formation (no inside-out) cannot reproduce the slope in the inner disk. On the other hand, models with no inside-out mechanism can

well reproduce the distributions of the star formation rate and the gas density along the disk. A good way of testing the inside-out disk formation is to see whether there is a size and luminosity evolution of disks at high redshift. Roche et al. (1998), by studying galaxies in the reshift range 2.5-3.0, concluded that the larger increase of the surface brightness relative to the luminosity at high redshift is an indication of an inside-out disk formation. They tested their results by means of the C97 model. Another important issue concerns the existence of a threshold gas density for star formation. Recently, Boissier et al. (2006), by means of Galex data, suggested that the threshold might not exist or be much lower that thought before. Note, however, that the low level of star formation observed with GALEX at the outer edges of disks does not produce OB associations, hence no massive stars which are the main responsible for enriching the ISM. Therefore, the abundance gradients really measure the threshold for massive star formation. It is important to underline that models such as those of Prantzos (without threshold) and Tosi (constant infall)were able to fit the abundance gradients. According to us, however, the reason is that these two groups used only a disk model, without a contribution from the halo/thick disk phase.

- In the framework of models with no inside-out mechanism such as the model proposed by C08 we tested the effect of the efficiency of star formation varying with the galactocentric radius, being higher in the innermost than in the outermost regions of the Galactic disk. This assumption, even without the threshold in the surface gas density, can produce gradients with the right slope both in the inner and outer regions of the Galactic disk but it fails in reproducing the gas density distribution along the disk.

- A cosmological model without threshold, with a star formation efficiency changing with radius and with a very simple inside-out prescription, can well reproduce the SFR along the disk as well as the behavior of the surface gas density. Moreover, it can well reproduce the outer abundances gradients. However, in the inner part of the disk

it produces too flat gradients, even if the slope is more pronunced then that of Model C08.

Therefore, we conclude that to reproduce at the same time the abundance, star formation rate and surface gas density gradients along the Galactic disk it is necessary to assume an **inside-out formation** for the disk. The threshold in the gas density is not necessary and the same effect could be obtained by assuming a variable efficiency of star formation. The inclusion of radial flows without an inside-out formation of the disk would have the same effect as the threshold gas density without inside-out effect (Portinari & Chiosi, 2000).

- It is clear from our numerical simulations that while the process of formation of the Galactic disk has a major impact on the formation of abundance gradients, the specific adopted SF law has a major effect on the gas distribution along the disk. This effect could be used to infer the SF law from the gas distributions along disks of spirals.

- We conclude that our cosmological simulation has not a sufficient resolution to be able to capture the real inside-out formation of a galaxy-sized DM halo. High resolution cosmological simulations and/or resimulation of a single DM halo should be performed in order to understand if a suitable baryon accretion law can be inferred from collisionless simulations, or if the full gas physics and sub-grid treatment of astrophysical processes as star formation and energy feedback from SNe is unavoidably needed to get a realistic description of the formation of a galaxy.

In computing the model with a cosmologically derived infall law for the formation of an elliptical galaxy we found that:

- Models without galactic wind, in which the star formation never stops, predict a too large current SNIa rate. In particular, the cosmological model produces a current SNIa rate which is about ten times higher than the observed values given by Mannucci et al. (2008) for ellipticals. In order to reproduce the observed SNIa rate with the cosmological

model, one should adopt, in the calculation of the SN Ia rate, a value of the constant A (see eq. 2) ten times lower, an unrealistically low value which would predict a too low type Ia SN rate in the solar vicinity.

- Models without wind predict also a large current SNII rate. In particular, the cosmological model gives a current SNII rate which is higher than the SNIa rate, whereas from observations given by Mannucci et al. (2008) it is known that the SNIa rate is at least three time higher than the SNII rate in ellipticals. On the other hand, models based on the monolithic scenario predict almost no current star formation rate and therefore a negligible number of current type II SNe, at variance with some GALEX data, indicating recent star formation, although in a very small fraction of ellipticals.

- The mean value for the [Mg/Fe] ratio in the dominant stellar population, as predicted by our cosmological model, which is an important indicator for the robustness of a model, is too low, as expected. We predict [Mg/Fe]~ -0.3 dex. For an elliptical galaxy of the same mass Thomas et al. (2005) give a value of $\sim +0.2$ dex, corresponding to a gap of about 0.5 dex. This is, according to us, the most important, although negative, result of our cosmological model.

- In conclusion, it is important to underline some shortcomings of our approach and in particular the fact that ellipticals are tipically found in clusters of galaxies, whereas in our simulation we model an isolated elliptical galaxy. In a galaxy cluster there are some important physical processes (i.e. ram-pressure stripping, tidal stripping, harassment among others) that we do not consider in our DM-only simulation and that can influence the properties and the amount of the gas. Another important process that we do not consider is that ellipticals are likely to accrete not only gas during the mergers but also already formed stars. In this case, details on baryons properties become important and they cannot be ignored.

  What we can say here is that using a very simple cosmologically derived infall law for an elliptical galaxy it is not possible to reproduce the most

important chemical constraints given by observations. In our opinion, the problem resides in the too long and poorly efficient star formation rate predicted for typical and large ellipticals in the hierarchical galaxy formation scenario.

Bibliography

[1] Aarseth S. J., 1963, MNRAS, 126, 223

[2] Abadi M. G., Navarro J. F., Steinmetz M. & Eke V. R., 2003, ApJ, 591, 499

[3] Abadi M. G., Navarro J. F., Steinmetz M. & Eke V. R., 2003, ApJ, 597, 21

[4] Afflerbach A., Churchwell E. & Werner M. W., 1997, ApJ, 478, 190

[5] Andrievsky S. M., Kovtyukh V. V., Luck R. E., LÃ©pine J. R. D., Bersier D., Maciel W. J., Barbuy B., Klochkova V. G. et al., 2002a, A&A, 381, 32

[6] Andrievsky S. M., Bersier D., Kovtyukh V. V., Luck R. E., Maciel W. J., LÃ©pine J. R. D. & Beletsky Y. V., 2002b, A&A, 384, 140

[7] Andrievsky S. M., Kovtyukh V. V., Luck R. E., LÃ©pine J. R. D., Maciel W. J. & Beletsky Yu. V., 2002c, A&A, 392, 491

[8] Andrievsky S. M., Luck R. E., Martin P. & Lépine J. R. D. , 2004, A&A, 413, 159

[9] Arimoto N. & Yoshii Y., 1987, A&A, 173, 23

[10] Asplund M., Grevesse N. & Sauval A. J., 2005, ASPC, 336, 25

[11] Beers T. C. & Sommer-Larsen J., 1995, ApJS, 96, 175

[12] Bekki K. & Shioya Y., 1999, ApJ, 513, 108

[13] Bensby T., Feltzing S. & Lundström, 2003, A&A, 410, 527

[14] Bertschinger E., 1995, astro.ph, 6070

[15] Bildfell C., Hoekstra H., Babul A. & Mahdavi A., 2008, MNRAS, 389, 1637

[16] Blitz L., Fich M. & Kulkarni S., 1983, *Science* 220: 1233

[17] Boissier S. & Prantzos N., 1999, MNRAS, 307, 857

[18] Boissier S. & Prantzos N., 2000, MNRAS, 312, 398

[19] Boissier S., Boselli A., Prantzos N. & Gavazzi G., 2001, MNRAS, 321, 733

[20] Boissier S., Gil de Paz A., Boselli A., Madore B. F., Buat V., Cortese L., Burgarella D., Munoz Mateos J. C. et al., 2006, astro-ph/0609071

[21] Bower R. G., Lucey J. R. & Ellis R. S., 1992, MNRAS, 254, 601

[22] Bronfman L., 1986, PhD thesis Univ. Columbia, 251 pp.

[23] Bryan G. L. & Norman M. L., 1997, ASPC, 123, 363

[24] Bullock J. S., Kolat T. S., Sigad Y., Somerville R. S., Kravtsov A. V., Klypin A. A., Primack J. R. & Dekel A., 2001, MNRAS, 321, 559

[25] Burkert A., Truran J. W. & Hensler G., 1992, ApJ, 391, 651

[26] Burstein D., Bender R., Faber S. M., Nolthenius R., 1997, AJ, 114, 1365

[27] Carbon D. F., Barbuy B., Kraft R. P., Friel E. D. & Suntzeff N. B., 1987, PASP, 99, 335

[28] Carigi L., 1994, ApJ, 424, 181

[29] Carigi L., 1996, RMxAA, 32, 179

[30] Carney B. W., Wright J. S., Sneden C., Laird J. B., Aguilar L. A. & Latham D. W., 1997, AJ, 114, 363

[31] Carollo C. M., Danziger I. J. & Buson L., 1993, MNRAS, 265, 553

[32] Carraro G., Ng Y. K. & Portinari L., 1998, MNRAS, 296, 1045

[33] Carretta E., Gratton R., Cohen J. G., Beers T. C. & Christlieb N., 2002, AJ, 124, 481

[34] Cayrel R., Depagne E., Spite M., Hill V., Spite F., François P., Plez B., Beers T. et al., 2004, A&A, 416, 1117

[35] Cescutti G., François P., Matteucci F., Cayrel R. & Spite M., 2006, A&A, 448, 557

[36] Cescutti G., Matteucci, F. François P. & Chiappini, C. 2007, A&A, 462, 943

[37] Chabrier G., 2003, PASP, 115, 763

[38] Chen L., Hou J. L., Wang J. J., 2003, AJ, 125, 1397

[39] Chiappini C., Matteucci F. & Gratton R., 1997, ApJ, 477, 765

[40] Chiappini C., Matteucci F. & Romano D., 2001, ApJ, 554, 1044

[41] Chiappini C., Romano D. & Matteucci F., 2003, MNRAS, 339, 63

[42] Chiosi C., 1980, A&A, 83, 206

[43] Chiosi C. & Carraro G., 2002, MNRAS, 335, 335

[44] Clegg R. E. S., Lambert D. L. & Tomkin J., 1981, ApJ, 250, 262

[45] Colavitti E., Matteucci F. & Murante G., 2008, A&A, 483, 401

[46] Cowie L. L., Songaila A. & Hu E. M., 1996, AJ, 112, 839

[47] Daddi E., Cimatti A., Pozzetti L., Hoekstra H., Roettgering H. J. A., Renzini A., Zamorani G., Mannucci F., 2000, A&A, 361, 535

[48] Davies R. L., Sadler E. M. & Peletier R. F., 1993, MNRAS, 262, 650

[49] Davis M., Efstathiou G., Frenk G. S. & White S. D. M., 1985, ApJ, 292, 371

[50] Digel S., Bally J. & Thaddeus P., 1990, ApJ, 357, 29

[51] D'Onghia E. & Burkert A., 2004, ApJ, 612, 13

[52] D'Onghia E., Burkert A., Murante G. & Khochfar S., 2006, MNRAS, 372, 1525

[53] Dopita M. A. & Ryder S. D., 1994, ApJ, 430, 163

[54] Dressler A., Lynden-Bell D., Burstein D., Davies R. L., Faber S. M., Terlevich R. J., Wegner G., 1987, ApJ, 313, 42

[55] Dressler A., Oemler A. Jr., Couch W. J., Smail I., Ellis R. S., Barger A., Butcher H., Poggianti B. M., Sharples R. M., 1997, ApJ, 490, 577

[56] Efstathiou G., Davies M., White S. D. M. & Frenk G. S., 1985, ApJS, 57, 241

[57] Faber S. M., Worthey G. & Gonzalez J. J., 1992, in Barbuy B., Renzini A., eds, IAU Symp. 149, The Stellar Populations of Galaxies. Kluwer, Dordrecht, p. 255

[58] Ferrini F., Molla M., Pardi M. C. & Diaz A. I., 1994, ApJ, 427, 745

[59] François P., Matteucci F., Cayrel R., Spite M., Spite F. & Chiappini C., 2004, A&A, 421, 613

[60] Fulbright J. P., 2000, AJ, 120, 1841

[61] Fuhrnamm K., 1998, A&A 338, 161

[62] Garwood R. W. & Dickey J. M., 1989, ApJ, 338, 841

[63] Gilmore G., Wyse R. F. G. & Jones J. B., 1995, AJ, 109, 1095

[64] Gilroy K. K., Sneden C., Pilachowski C. A. & Cowan J. J., 1988, ApJ, 327, 298

[65] Giovagnoli A. & Tosi M., 1995, MNRAS, 273, 499

[66] Gonzalez J. J., 1993, PhD thesis Univ. California

[67] Gordon M. A. & Burton W. B., 1976, ApJ, 208, 346

[68] Governato F., Mayer L., Wadsley J., Gardner J. P., Willman B., Hayashi E., Quinn T., Stadel J. & Lake G., 2004, ApJ, 607, 688

[69] Governato F., Willman B., Mayer L., Brooks A., Stinson G., Valenzuela O., Wadsley J., Quinn T., 2007, MNRAS, 374, 1479

[70] Gratton R. & Sneden C., 1988, A&A, 204, 193

[71] Gratton R. & Sneden C., 1994, A&A, 287, 927

[72] Gratton R., Carretta E., Matteucci F. & Sneden C., 1996, ASPC, 92, 371

[73] Gratton R., Carretta E., Matteucci F. & Sneden C., 2000, A&A, 358, 671

[74] Greggio L. & Renzini A., 1983, A&A, 118, 217

[75] Greggio L., 2005, A&A, 441, 1055

[76] Gummersbach C. A., Kaufer A., Schäfer D. R., Szeifert T. & Wolf B., 1998, A&A, 338, 881

[77] Guzmán R., Gallego J., Koo D. C., Phillips A. C., Lowenthal J. D., Faber S. M., Illingworth G. D. & Vogt N. P., 1997, ApJ, 489, 559

[78] Hachisu I, Kato M. & Nomoto K., 1996, ApJ, 470, 97

[79] Han Z. & Podsiadlowski P., 2004, MNRAS, 350, 1301

[80] Helmi A., White S. D. M. & Springel V., 2003, MNRAS, 339, 834

[81] Hicks A. K. & Mushotzky R., 2005, ApJ, 635, L9

[82] Hou J. L., Prantzos N. & Boissier S., 2000, A&A, 362, 921

[83] Iben I. Jr. & Tutukov A., 1984, ApJ, 284, 719

[84] Israelian G., Ecuvillo A., Rebolo R., García-López R., Bonifacio P. & Molaro P., 2004, A&A, 421, 649

[85] Iwamoto K., Brachwitz F., Nomoto K., Kishimoto N., Umeda H., Hix W. R. & Thielemann F. K., 1999, ApJS, 125, 439

[86] Jørgensen B. R., 2000, A&A, 363, 947

[87] Kauffmann G. & White S. D. M., 1993, MNRAS, 261, 921

[88] Kauffmann G. & Charlot S., 1998, MNRAS, 294, 705

[89] Kauffmann G., Colberg J. M., Diaferio A. & White S. D. M., 1999, MNRAS, 303, 188

[90] Kauffmann G., 2001, ASPC, 245, 381

[91] Kaviraj S., Khochfar S., Schawinski K., Yi S. K., Gawiser E., Silk J., Virani S. N., Cardamone C. N. et al., 2008a, MNRAS, 388, 67

[92] Kaviraj S., 2008b, Modern Physics Letters A, 23, 153

[93] Kawata D. & Gibson B. K., 2003a, IAUS, 208, 413

[94] Kawata D. & Gibson B. K., 2003b, MNRAS, 340, 908

[95] Kennicutt R.C. Jr., 1998a, ApJ, 498, 541

[96] Kennicutt R.C. Jr., 1998b, AAR&A, 36, 189

[97] Klypin A. & Primack J. R., 2001, ApJ, 554, 903

[98] Kobayashi C., Tsujimoto T., Nomoto K., Hachisu I. & Kato M., 1998, ApJ, 503, L155

[99] Kormendy J. & Djorgovski S., 1989, ARA&A, 27, 235

[100] Kotoneva E., Flynn, C., Chiappini, C. & Matteucci, F., 2002, MNRAS 336, 879

[101] Kroupa P., Tout C. A. & Gilmore G., 1993, MNRAS, 262, 545

[102] Kroupa P., 2001, MNRAS, 322, 231

[103] Kuntschner H., 2000, MNRAS, 315, 184

[104] Kuntschner H., Lucey J. R., Smith R. J., Hudson M. J., Davies R. L., 2001, MNRAS, 323, 615

[105] Lacey C. G. & Fall S. M., 1985, ApJ, 290, 154

[106] Laird J. B., 1985, ApJS, 57, 389

[107] Laird J. B., 1985, ApJS, 289, 556

[108] Lanfranchi, G. & Matteucci, F. 2004, MNRAS, 351, 1338

[109] Larson R. B., 1972, Nature, 236, 21

[110] Larson R. B., 1974, MNRAS, 166, 585

[111] Larson R. B., 1976, MNRAS, 176, 31

[112] Luck R. E., Gieren W. P., Andrievsky S. M., Kovtyukh V. V., Fouqué P., Pont F. & Kienzle F., 2003, A&A, 401, 939

[113] Maeder A., 1992, A&A, 264, 105

[114] Malinie G., Hartmann D. H., Clayton D. D. & Mathews G. J., 1993, ApJ, 413, 633

[115] Mannucci F., Maoz D., Sharon K., Botticella M. T., Della Valle M., Gal-Yam A., Panagia N., 2008, MNRAS, 383, 1121

[116] Martinelli A., Matteucci F. & Colafrancesco S., 1998, MNRAS, 298, 42

[117] Matteucci F. & Chiosi C., 1983, A&A, 123, 121

[118] Matteucci F. & Greggio L., 1986, A&A, 154, 279

[119] Matteucci F. & Tornambè A., 1987, A&A, 185, 51

[120] Matteucci F. & François P., 1989, MNRAS, 239, 885

[121] Matteucci F. & François P., 1992, A&A, 262, 1

[122] Matteucci F., Raiteri C. M., Busson M., Gallino R. & Gratton R., 1993, A&A, 272, 421

[123] Matteucci F., 1994, A&A, 288, 57

[124] Matteucci F., Ponzone R. & Gibson B. K., 1998, A&A, 335, 855

[125] Matteucci F. & Recchi S., 2001, ApJ, 558, 351

[126] Matteucci F., 2001, *TheChemicalEvolutionoftheGalaxy*, ASSL, Kluwer Academic Publisher

[127] Matteucci F. & Pipino A., 2002, ApJ, 596, 69

[128] Matteucci F., 2008, [arXiv:0804.1492]

[129] McWilliam A., Preston G. W., Sneden C. & Searle L., 1995, AJ, 109, 2757

[130] Merlin E. & Chiosi C., 2006, A&A, 457, 437

[131] Meynet G. & Maeder A., 2002, A&A, 390, 561

[132] Meynet G. & Maeder A., 2003, A&A, 404, 975

[133] Meynet G. & Maeder A., 2005, A&A, 429, 581

[134] Naab T. & Ostriker J. P., 2006, MNRAS, 366, 899

[135] Nagashima M., Lacey C. G., Okamoto T., Baugh C. M., Frenk C. S. & Cole S., 2005, MNRAS, 363, 31

[136] Nagashima M. & Okamoto T., 2006, ApJ, 643, 863

[137] Navarro J. F., Frenk C. S. & White S. D. M., 1995, MNRAS, 275, 56

[138] Navarro J. F., Frenk C. S. & White S. D. M., 1996, ApJ, 462, 563

[139] Navarro J. F., Frenk C. S. & White S. D. M., 1997, ApJ, 490, 493

[140] Navarro J. F. & Steinmetz M., 2000, ApJ, 538, 477

[141] Nelan J. E., Smith R. J., Hudson M. J., Wegner G. A., Lucey J. R., Moore S. A. W., Quinney S. J. & Suntzeff N. B., 2005, ApJ, 632, 137

[142] Nissen P. E. & Schuster W. J., 1997, A&A, 326, 751

[143] Nissen P. E., Primas F. & Asplund D. L. M. L., 2002, A&A, 390, 235

[144] O'Dea C. P., Baum S. A., Privon G., Noel-Storr J., Quillen A. C., Zufelt N., Park J., Edge A. et al., 2008, ApJ, 681, 1035

[145] Pagel B. E. J. & Patchett B. E., 1975, MNRAS, 172, 13

[146] Pagel B. E. J., 1989 in "Evolutionary phenomena in galaxies", Cambridge University Press, 201

[147] Pardi M. C. & Ferrini F., 1994, ApJ, 421, 491

[148] Pardi M. C., Ferrini F. & Matteucci F., 1995, ApJ, 444, 207

[149] Peebles P. J. E., 2002, in Metcalfe N., Shanks T., eds, ASP Conf. Ser. Vol. 283, A New Era in Cosmology. Astron. Soc. Pac., San Francisco, p. 351

[150] Peletier R. F., Davies R. L., Illingworth G. D., Davies L. E., Cawson M., 1990, AJ, 100, 1091

[151] Pipino A., Matteucci F., Borgani S., Biviano A., 2002, ASPC, 253, 355

[152] Pipino A. & Matteucci F., 2004, MNRAS, 347, 968

[153] Pipino A., Kaviraj S., Bildfell C., Hoekstra H., Babul A. & Silk J., 2008, [arXiv:0807.2760]

[154] Portinari, L. & Chiosi, C., 2000, A&A, 355, 929

[155] Power C., Navarro J. F., Jenkins A., Frenk C. S., White S. D. M., Springel V., Stadel J. & Quinn T., 2003, MNRAS, 338, 14

[156] Prantzos N. & Aubert O., 1995, A&A, 302, 69

[157] Prantzos N., 2003, Ap&SS, 284, 675

[158] Press W. H. & Schechter P., 1974, ApJ, 187, 425

[159] Prochaska J. X., Naumov S. O., Carney B. W., McWilliam A. & Wolfe A. M., 2000, AJ, 120, 2513

[160] Raiteri C. M., Villata M. & Navarro J. F., 1996, A&A, 315, 105

[161] Raiteri C. M., Villata M. & Navarro J. F., 1996, MmSaIt, 67, 817

[162] Raiteri C. M., Villata M., Gallino R., Busso M. & Cravanzola A., 1999, ApJ, 518, 91

[163] Rana N. C. & Wilkinson D. A., 1986, MNRAS, 218, 721

[164] Rana N. C., 1991, ARA&A, 29, 129

[165] Recchi S., Matteucci F., D'Ercole A. & Tosi M., 2002, A&A, 384, 799

[166] Reid M. J., 1993, ARA&A, 31, 345

[167] Robertson B., Yoshida N., Springel V. & Hernquist L., 2004, ApJ, 606, 32

[168] Robertson B., Bullock J. S., Font A. S., Johnston K. V. & Hernquist L., 2005, ApJ, 632, 872

[169] Robinson B. J., Manchester R. N., Whiteoak J. B., Otrupcek R. E. & McCutcheon W. H., 1988, A&A, 193, 60

[170] Rocha-Pinto H. J. & Maciel W. J., 1996, MNRAS, 279, 447

[171] Roche N., Ratnatunga K., Griffiths R. E., Im M. & Naim A., 1998, MNRAS, 293, 157

[172] Ryan S., Norris J. E. & Bessell M. S., 1991, AJ, 102, 303

[173] Salim S., Charlot S., Rich R. M., Kauffmann G., Heckman T. M., Barlow T. A., Bianchi L., Byun Y.-I. et al., 2005, ApJ, 619, 39

[174] Salpeter E. E., 1955, ApJ, 121, 161

[175] Samland M. & Hensler G., 1996 in "New light on galaxy evolution", Kluwer Academic Publishers, 23

[176] Samland M., Hensler G. & Theis Ch., 1997, ApJ, 476, 544

[177] Samland M., 2004, PASA, 21, 175

[178] Scalo J. M., 1986, FCPh, 11, 1

[179] Scalo J. M., 1998, "The Stellar Initial Mass Function", A.S.P. Conf. Ser., Vol. 142 p. 201

[180] Scannapieco C., White S. D. M., Springel V. & Tissera P. B., 2008, [arXiv:0812.0976]

[181] Schmidt M., 1959, ApJ, 129, 243

[182] Simpson J. P., Colgan S. W. J., Rubin R. H., Erikson E. F. & Haas M. R., 1995, ApJ, 444, 721

[183] Sneden C. & Cowan J. J., 2003, Science, vol 299, Issue 5603, pp. 70

[184] Sommer-Larsen J. & Yoshii Y., 1989, MNRAS, 238, 133

[185] Sommer-Larsen J. & Yoshii Y., 1990, MNRAS, 243, 468

[186] Sommer-Larsen J., Gelato, S. & Vedel, H., 1999, ApJ 519, 501

[187] Spergel D. N., Bean R., Doré O., Nolta M. R., Bennet C. L., Dunkley J., Hinshaw J., Jarosik N. et al., 2007, ApJS, 170, 377

[188] Spite M., Cayrel R., Plez B., Hill V., Spite F., Depagne E., François P., Bonifacio P. et al., 2005, A&A, 430, 655

[189] Springel V., White S. D. M., Tormen G. & Kauffmann G., 2001, MNRAS, 328, 726

[190] Springel V., 2005, MNRAS, 364, 1105

[191] Steidel C. C., Giavalisco M., Pettini M., Dickinson M., Adelberger K. L., 1996a, ApJ, 462, L17

[192] Steidel C. C., Giavalisco M., Dickinson M., Adelberger K. L., 1996b, AJ, 112, 352

[193] Stephens A., 1999, AJ, 117, 1771

[194] Talbot R. J. Jr. & Arnett W. D., 1971, ApJ, 170, 409

[195] Talbot R. J. Jr. & Arnett W. D., 1973, ApJ, 186, 51

[196] Talbot R. J. Jr. & Arnett W. D., 1973, ApJ, 186, 69

[197] Talbot R. J. Jr. & Arnett W. D., 1975, ApJ, 197, 551

[198] Tamura N., Kobayashi C., Arimoto N., Kodama T., Ohta K., 2000, AJ, 119, 2134

[199] Tantalo R., Chiosi C., Bressan A., Marigo P., Portinari L., 1998b, A&A, 335, 823

[200] Theis C., Burkert A. & Hensler G., 1992, A&A, 265, 465

[201] Thomas D., Maraston C. & Korn A., 2004, MNRAS, 351, 19

[202] Thomas D., Maraston C., Bender R., Mendes de Oliveira C., 2005, ApJ, 621, 673

[203] Timmes F. X., Woosley S. E. & Weaver T. A., 1995, ApJS, 98, 617

[204] Tinsley B. M., 1980, Fund. Cosmic Phys. Vol. 5, 287

[205] Tomkin J., Woolf V. M., Lambert D. L. & Lemke M., 1995, AJ, 109, 2204

[206] Tosi M., 1988, A&A, 197, 47

[207] Trager S. C., Worthey G., Faber S. M., Burstein D., Gonzalez J. J., 1998, ApJS, 116, 1

[208] Trager S. C., Faber S. M., Worthey G., Gonzalez J. J., 2000b, AJ, 120, 165

[209] Tsujimoto T., Yoshii Y., Nomoto K. & Shigeyama T., 1995, A&A, 302, 704

[210] Twarog B. A., Ashman K. M. & Anthony-Twarog B. J., 1997, ApJ, 114, 2556

[211] van den Hoek L. B. & Groenewegen M. A. T., 1997, A&AS, 123, 305

[212] Wechsler R. H., Bullock J. S., Primack J. R., Kravtsov A. V. & Dekel A., 2002, ApJ, 568, 52

[213] Weidner C. & Kroupa P., 2005, ApJ, 625, 754

[214] Weiss A., Peletier R. F. & Matteucci F., 1995, A&A, 296, 73

[215] Whelan J. & Iben I. Jr., 1973, ApJ, 186, 1007

[216] White S. D. M. & Rees M. J., 1978, MNRAS, 183, 341

[217] Woosley S. E. & Weaver T. A., 1995, AIPC, 327, 365

[218] Worthey G., Faber S. M. & Gonzalez J. J., 1992, ApJ, 398, 69

[219] Wouterloot J. G. A., Brand J., Burton W. B. & Kwee K. K., 1990, A&A, 230, 21

[220] Wyse R. F. G. & Gilmore, G. 1995, AJ, 110, 2771

[221] Wyse R. F. G. & Silk J., 1989, ApJ, 339, 700

[222] Yi S. K., Peng E., Ford H., Kaviraj S., Yoon S.-J., 2004, MNRAS, 349, 1493